Terahertz Spectroscopy in Microfluidic Systems

Matthew Swithenbank, MEng

Submitted in accordance with the requirements for the degree of Doctor of Philosophy

The University of Leeds

School of Electronic and Electrical Engineering

August 2017

The candidate confirms that the work submitted is his own and that appropriate credit has been given where reference has been made to the work of others.

This copy has been supplied on the understanding that it is copyright material and that no quotation from the thesis may be published without proper acknowledgement.

©2017 The University of Leeds and Matthew Swithenbank.

The right of Matthew Swithenbank to be identified as Author of this work has been asserted by him in accordance with the Copyright, Designs and Patents Act 1988.

Acknowledgements

First, I would like to thank my supervisors Dr Christopher Wood, and Professor John Cunningham for their guidance throughout my research. Their patience and input has been the cornerstone of this project, and I have appreciated their encouragement over the years. Thank you also to the Engineering and Physical Sciences Research Council for their role in funding this work.

Special thanks go to Dr Andrew Burnett who laid the foundations of my understanding of the terahertz field, and has been a great friend to me and everyone in our research group. I am also indebted to Dr Chris Russell for making such significant progress in the development of planar Goubau lines, for then passing on his extensive knowledge to me, and for teaching me many research fundamentals.

My friends at the university have made life a joy throughout my time in Leeds. Nick Greenall has helped with my coding in so many ways, always pushing me for a more elegant and ambitious solution to any problem; his advice and guidance has formed the basis for many of the successes in this work. Nic Hunter and Dave Bacon have not only provided excellent conversation, but have also helped with many aspects of this research from fabrication to measurement. I am grateful for the help of my more senior colleagues; Mark Rosamond, Alex Valavanis, and Josh Freeman who have proven to be fountains of knowledge and caffeine.

I would also like to take the opportunity to thank the open-source developers who have produced many of the tools used in the production of this thesis. The graphics in this work were designed in Inkscape, and the document itself was written in LaTeX using the Texmaker editor, the helpful guidance of these respective communities has been invaluable. I am also thankful for the WebPlotDigitizer, which is an excellent tool for extracting plotted data from image files. All these tools are freely-available to any user, and for that I am very grateful.

On a personal note, my deepest thanks also go to my wonderful family. My parents taught me to be interested, always encouraged me, and have given me unwavering love and support. Finally, I would like to thank my superb wife Jo. She has kept me laughing throughout the last four years, supported me at every turn, and encouraged me to knuckle-down on many occasions. Her own successes over this time have filled me with pride, and excitement for the future.

Abstract

Spectroscopic measurements in the terahertz-frequency-range can offer insight into the picosecond dynamics, molecular conformation, and biological function of chemical systems. Despite the recent emergence of terahertz-frequency time-domain spectroscopy as a tool for the measurement of dry, solid samples, the investigation of liquid analytes is complicated by the strong attenuation of terahertz-frequency signals in aqueous environments. The integration of microfluidic systems with on-chip waveguides offers a potential solution as picosecond pulses confined to a waveguide can interact with nano- or microlitre liquid sample volumes over a distance of several millimetres, with significantly reduced attenuation compared to free-space techniques. Specifically, the single-wire planar Goubau line waveguide has attracted attention in recent years owing to the relatively large extent of the supported evanescent field, enabling sensitive interaction between a propagating electric field and nearby samples. In this work, the first on-chip microfluidic spectrometer, capable of measuring the complex permittivity of liquids in the terahertz-frequency range is introduced.

The fabrication of planar Goubau line devices with integrated photoconductive switches for the generation and detection of terahertz-frequency electric fields is discussed in detail. Given the importance of maximising the signal-to-noise ratio in spectroscopic measurements, an investigation of the signals excited from these switches is conducted, and factors such as the pump-power, generating beam polarisation, and switch geometry are found to have a significant impact on signal generation efficiency and noise. In addition to problematic signal noise, waveguide geometries can introduce artefacts that complicate further analysis. To simplify later modelling of these structures, the sources of unwanted reflections and propagation modes are identified, and prevented by design.

The integration of microfluidic systems with on-chip waveguides presents several interesting challenges. Intimate contact between the waveguide and analyte allows for sensitive measurement of the sample properties, yet the electronic circuitry required to generate and detect a probing terahertz field must be isolated from the risk of a short-circuit presented by the potentially conductive liquid. A device structure is proposed that simultaneously overcomes these design limitations, and comprises a geometry that can be accurately modelled. Given the lack of analytical

models with which the planar Goubau line can be described, numerical modelling techniques are used to create an accurate simulation of the device structure. A method is then introduced that allows interpretation of experimental data, such that the complex permittivity of unknown liquid samples can be calculated.

This new technique is used to measure the complex permittivity of a selection of well-studied polar alcohols, and the results are found to compare well to those available in literature. A free-space terahertz spectroscopy system is then used to measure liquid samples that have not been published in order to verify the results of the on-chip spectrometer when used to measure a wider range of liquid samples.

Publications

The work presented in this thesis has been included in the following journal papers and conference proceedings.

Peer-reviewed journals

M. Swithenbank, A. D. Burnett, C. Russell, L. H. Li, A. G. Davies, E. H. Linfield, J. E. Cunningham, and C. D. Wood, "On-chip terahertz-frequency measurements of liquids," *Analytical Chemistry*, vol. 89, no. 15, pp. 7981–7987, 2017.

C. Russell, **M. Swithenbank**, C. D. Wood, A. D. Burnett, L. H. Li, E. H. Linfield, A. G. Davies, and J. E. Cunningham, "Integrated on-chip THz sensors for fluidic systems fabricated using flexible polyimide films," *IEEE Transactions on Terahertz Science and Technology*, vol. 6, no. 4, pp. 619–624, 2016.

D. R. Bacon, A. D. Burnett, **M. Swithenbank**, C. Russell, L. H. Li, C. D. Wood, J. E. Cunningham, A. G. Davies, P. Dean, and J. R. Freeman "Free-space terahertz radiation from a LT-GaAs-on-quartz large-area photoconductive emitter," *Optics Express*, vol. 24, no. 23, pp. 26986–26997, 2016.

B. Hong, **M. Swithenbank**, N. Somjit, and I. Robertson, "Asymptotically single-mode small-core terahertz Bragg fibre with low loss and low dispersion," *Journal of Physics D: Applied Physics*, vol. 50, no. 4, 045104, 2017.

Conference proceedings

N. Abd Razak, **M. Swithenbank**, A. D. Burnett, N. R. Greenall, E. H. Linfield, A. G. Davies, J. E. Cunningham, and C. D. Wood, "THz-TDS of liquids in a temperature-controlled transmission flowcell," *The 42nd International Conference on Infrared, Millimeter, and Terahertz Waves*, 2017.

M. Swithenbank, C. Russell, A. D. Burnett, L. H. Li, E. H. Linfield, A. G. Davies, J. E. Cunningham, and C. D. Wood, "Accurate parameter extraction from liquids measured using on-chip terahertz spectroscopy," *The 41st International Conference on Infrared, Millimeter, and Terahertz Waves*, 2016.

M. Swithenbank, C. Russell, A. D. Burnett, L. H. Li, E. H. Linfield, A. G. Davies, J. E. Cunningham, and C. D. Wood, "On-chip terahertz spectroscopy of liquid mixtures," *The 40th International Conference on Infrared, Millimeter, and Terahertz Waves*, 2015.

M. Swithenbank, C. Russell, A. D. Burnett, L. H. Li, E. H. Linfield, A. G. Davies, J. E. Cunningham, and C. D. Wood, "Development of planar Goubau line – microfluidic integrated devices for THz spectroscopy of liquid analytes," *IET Colloquium on Millimetre-wave and Terahertz Engineering & Technology*, 2015.

Contents

List of Figures

List of Principal Symbols

A	Electric field amplitude.
c	Speed of light in a vacuum.
E	Electric field.
k	Angular wavenumber.
l	Propagation length.
$\tilde{n}$	Complex refractive index.
n'	Real component of the complex refractive index, $\tilde{n}$.
n''	Imaginary component of the complex refractive index, $\tilde{n}$.
j	Imaginary number ($\mathrm{j}^2 = -1$).
$\tan(\delta)$	Loss tangent.
α	Absorption coefficient.
β	Per-unit-length phase coefficient.
$\tilde{\varepsilon}$	Complex permittivity.
ε'	Real component of the complex permittivity, $\tilde{\varepsilon}$.
ε''	Imaginary component of the complex permittivity, $\tilde{\varepsilon}$.
γ	Propagation constant.
θ	Frequency-dependent phase-angle.
ω	Angular frequency.
φ	Frequency-dependent phase-shift.
ζ	Per-unit-length attenuation coefficient.
$\square_{\mathrm{eff}}$	Subscript denotes an effective measure of the given parameter.
$\square_{\mathrm{r}}$	A reference for the given parameter.
$\square_{\mathrm{s}}$	A sample measurement of the given parameter.
$\tilde{\square}$	Denotes the complex form of the given variable.

Chapter 1

An Introduction to Terahertz and Microfluidic Systems

Sometimes referred to as sub-millimetre radiation, the terahertz region of the electromagnetic spectrum is typically taken to cover the range of wavelengths between 1 mm and 0.03 mm (0.3 THz to 10 THz [1]). Historically, this region has represented frequencies that are particularly difficult to generate with artificial sources owing to its location at the interface between electronic and optical technologies. As sources have become more wide-spread, terahertz time-domain spectroscopy, with its clear applications in biochemistry [2], pharmaceuticals [3], and security [4], has played a significant role in expanding interest in the field. Specifically, many materials have been found to exhibit unique spectral characteristics in the terahertz band, as long-range intermolecular vibrational modes are accessed that yield information about conformation in addition to atomic content, such that structurally similar (or even polymorphic) samples can be distinguished [5, 6]. Despite the many strengths of terahertz-frequency spectroscopy, limitations such as attenuation in aqueous environments restrict the interrogation of biological samples in physically relevant contexts [2]. The integration of on-chip terahertz waveguides and microfluidic systems is a compelling potential solution to this problem as picosecond pulses confined to a transmission line can interact with nano- or microlitre sample volumes over relatively long (millimetre) distances, thereby overcoming the signal attenuation that dominates conventional free-space measurements [7].

To provide some historical context to the field of terahertz-frequency microflu-

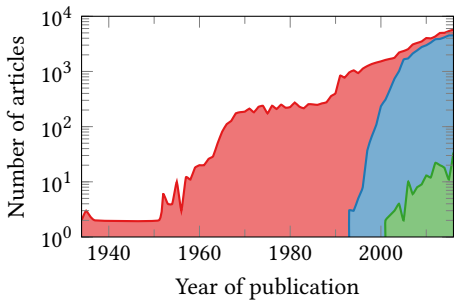

Figure 1.1: The number of journal articles published per year that discussed the fields of terahertz (red) or microfluidics (blue), and those that studied both (green). All data collated from the Web of Science [8].

idics, a search of the Web of Science database [8] was conducted in which all published articles that discuss terahertz or microfluidics were compiled. Given the various naming conventions that have been used in the literature, the search terms "terahertz," "sub-millimetre," "t-ray," and "far-infrared," along with regional spelling variants were investigated. As Figure 1.1 shows, the interest in terahertz technologies experienced a first major growth in the 1970s as the development of several new sources enabled the generation of terahertz radiation. Coinciding with the development of the terahertz time-domain spectroscopy technique [9], the terahertz field experienced a second boom period in the 1990s that has continued to this day (further supported by the invention of the terahertz quantum cascade laser in the early 2000s [10]), with several thousand articles published each year. In contrast, microfluidic systems have only been discussed since the early 1990s yet the interest surrounding them has resulted in a significant growth, such that there were almost as many articles published in both fields in recent years. Despite the development of both terahertz and microfluidic fields, very few articles are published that discuss both subjects. This may be due in part to the complications involved in integrating microfluidic and terahertz-frequency systems such that useful spectroscopic information can be extracted from liquid samples. Thus, the study of terahertz spectroscopy in microfluidic devices, such as the creation of an on-chip terahertz-frequency spectrometer, may pave the way for an increased interest in the integration of these two fields.

1.1 The generation and detection of terahertz radiation

Over the decades of research in the field, many emitters and detectors of terahertz-frequency radiation have been investigated [11], with researchers typically either working to increase the operating frequency of traditional electronic devices, or the wavelength of optical systems. Terahertz-frequency spectroscopic applications are usually based upon technologies that can generate and detect across a relatively broad spectral range, to maximise the sample information that can be garnered. Therefore, most technologies used in spectroscopy produce either spectrally-narrow but tuneable radiation, or simultaneously emit across a broad range of wavelengths.

1.1.1 The photoconductive antenna

Of the many competing sources, the photoconductive antenna has emerged as the emitter most commonly used in terahertz time-domain spectroscopy. As illustrated in Figure 1.2, a photoconductive switch comprises a metal dipole patterned on a semiconductor material, in which carriers with very short (sub-picosecond) lifetimes are generated by optical excitation.

Charge carriers are generated when the energy of an incoming photon exceeds that of the material bandgap, such that electrons in the valence band of the semiconductor can be excited into the conduction band [12]. The free carriers are then accelerated by the dipole bias, resulting in a sharp rise in current between the electrodes, which has spectral components that extend into the terahertz frequency range [13]. The generation of carriers is very rapid, and is primarily based on the

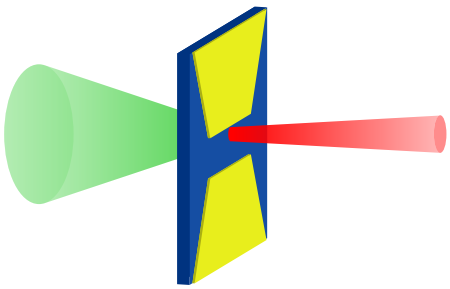

Figure 1.2: A dipole antenna patterned on a photoconductive substrate material. An illuminating laser (red) excites charge carriers in the semiconductor, resulting in the emission of terahertz radiation (green).

rise-time of the femtosecond laser that is used a source of optical excitation. However, the recombination of electrons back into the valence band is dependent on the carrier lifetime in the material.

Historically, photoconductive antennas have been fabricated on materials such as ion-damaged Si-on-sapphire, ion-damaged InP, and GaAs [14]. The implantation of ions in a material creates recombination centres that reduce the carrier lifetime as the ion concentration is increased, for example bombardment with O^+ ions was found to reduce the carrier lifetime of Si-on-sapphire from ~100 ps to 0.6 ps [15]. However, in addition to reducing the carrier lifetime, ion-damage also reduces the carrier mobility (30 $cm^2\ V^{-1}\ s^{-1}$ in ion-damaged Si-on-sapphire [14]), which in turn decreases the terahertz field generation efficiency. The carrier mobility in a material is proportional to the carrier velocity, v, under an electric field, which is related to the current density by [16],

$$J = env, \tag{1.1}$$

where e is the charge on an electron, and n is the free-carrier density. Given that the resulting terahertz electric field is

$$E_{\mathrm{THz}} \propto \frac{\delta J}{\delta t}, \tag{1.2}$$

it is clear that a low mobility is undesirable. Therefore, there is a balance between carrier lifetime and mobility that is required when engineering ion-damaged materials for photoconductive emission.

1.1.2 Low-temperature-grown gallium arsenide

Low-temperature-grown gallium arsenide (LT GaAs) is a material that has both a low carrier lifetime, and relatively high mobility (0.6 ps and 150 $cm^2\ V^{-1}\ s^{-1}$ respectively [14]). GaAs is typically grown by molecular beam epitaxy at temperatures in the range of 500 °C to 720 °C [17], however growth at temperatures less than 300 °C in an As-rich environment creates an arsenic excess (~1 %) [18], which forms precipitates when briefly annealed *ex situ* at a high temperature [14]. The precipitates create a miniband between the valence and conduction bands that acts as a recombination

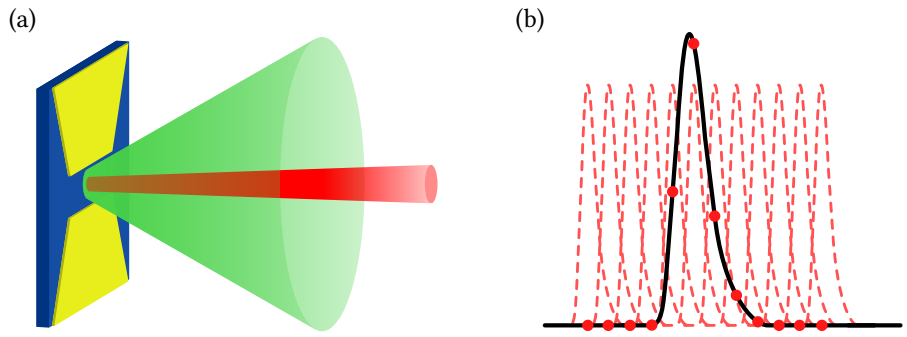

Figure 1.3: (a) A terahertz electric field (green) and probe laser beam (red) are focused between the electrodes of a photoconductive switch. (b) The transient current between the electrodes is sampled by delaying the arrival time of the probe beam (red, dashed) with respect to the terahertz pulse (black), such that the transient is sampled at multiple points.

centre to maintain sub-picosecond carrier lifetimes, and increases the resistivity of the material—essential for reducing the electronic noise of biased photoconductive switches [19].

Given the relatively high permittivity and absorption coefficient of GaAs, it is often desirable to transfer thin films of the material to an alternative host substrate. Epitaxially-grown LT GaAs films can be transferred to arbitrary substrates by a sacrificial lift-off technique [20]. Cunningham et al. [21], grew LT GaAs on a GaAs wafer that had been capped with a sacrificial layer of AlAs, which was etched in hydrofluoric acid to liberate the LT GaAs [22]. The released LT GaAs could then be transferred to a new host substrate and left to bond over a period of 24 hours through a combination of electrostatic and van der Waals forces [22].

1.1.3 Photoconductive detection

To generate terahertz radiation from a photoconductive antenna, a bias applied to the electrodes was electrically shorted by the transient increase in conductivity of the substrate material when optically excited. The same mechanism can be used to detect a pulse of terahertz radiation. As shown in Figure 1.3a, a transient terahertz electric field is focused onto the gap between the antenna electrodes, which produces a temporary dipole that is shorted by the simultaneous arrival of an ultrafast pulse of light, such as that generated by a femtosecond laser (see §1.1.5). The acceleration of the photocarriers under the bias of the terahertz field can therefore be measured as a current between the electrodes [23].

As the optical transient is considerably shorter than the duration of the terahertz pulse, a single measurement describes the current produced over a short window of the terahertz electric field. Therefore, as illustrated in Figure 1.3b, the arrival time of the probing laser pulse is delayed with respect to the transient terahertz field, so that the pulse is sampled over multiple points in the time-domain [23].

1.1.4 Electro–optic detection

Electro–optic detection exploits changes in the optical properties of materials that occur when an electric field is applied, specifically the introduction of birefringence owing to the Pockels effect [24]. The terahertz field applies a local bias to an electro–optic crystal (e.g. GaP, ZnTe, or GaSe) which distorts both the electron motion and crystal structure of the material to modify the axial refractive indices [25]. If n_x and n_y represent the refractive index of a crystal in the x- and y- planes respectively, then $n_x = n_y$ in an optically isotropic crystal. The structural changes as a result of the external field create anisotropy in the crystal such that the modified indices $\dot{n}_x \neq \dot{n}_y$, and the crystal exhibits a field-dependent birefringence.

The polarisation angle of a linearly polarised beam that passes through a birefringent crystal will be rotated by an angle determined by the difference between $\dot{n}_x$ and $\dot{n}_y$. An electro–optic detection scheme measures the rotation of the beam, which is effectively a measure of the electric field incident on the crystal, by first circularly polarising the rotated beam with a quarter-wave plate, then separating the vertically and horizontally polarised components with a Wollaston prism. The magnitudes of the two components are measured using a pair of balanced photodiodes, and the difference between them is proportional to the terahertz electric field. As was also the case with photoconductive detection, the terahertz transient is measured by delaying the arrival of the probing beam with respect to the terahertz pulse.

1.1.5 Ultrafast light sources

Both photoconductive and electro–optic generation and detection schemes require a highly-stable light source that emits short, high-power, periodic pulses. Also the

generation of charge carriers in the photoconductive material requires that the photon energy of the laser must exceed that of the semiconductor bandgap, which is 1.42 eV in GaAs [26], equivalent to a wavelength of 873 nm. When pumped with a continuous-wave laser centred around 500 nm, a Ti:sapphire crystal will fluoresce between 600 nm and 1100 nm, which equates to photon energies between 2 eV and 1.1 eV [27]. However, the broad spectral range generated in the laser cavity is supported by many cavity modes, with randomly fluctuating phase relationships. Pulsed behaviour is established by designing the laser cavity such that the desired mode is selectively focused, often achieved by Kerr-effect lensing in which the Ti:sapphire crystal is also used as a focusing lens [28]. The Kerr effect describes the change in refractive index of a material owing to a localised, intense electric field, such as that introduced by coherent pulses of laser light. Mode-locking can therefore be achieved in a laser cavity by aligning the optics around the Ti:sapphire crystal such that only the intense pulses passing through it are correctly focused and supported by the cavity mode.

1.2 Terahertz time-domain spectroscopy

An electromagnetic wave propagating through a material is both attenuated and delayed as a function of the absorption coefficient and refractive index of the propagation medium. Given that the terahertz pulses emitted from a photoconductive antenna cover a relatively broad spectral range (from hundreds of gigahertz up to tens of terahertz), a pulse that has propagated through an unknown sample will contain frequency-dependent information about the material properties. In terahertz time-domain spectroscopy, the difference in the losses of an unknown sample and a known reference material are measured, and a propagation model is then applied to extract the sample properties.

If the difference in phase between the waves propagating through the reference and sample media (r and s respectively) is $\varphi = \theta_\mathrm{r} - \theta_\mathrm{s}$, then the difference between

the refractive index of the reference and sample ($\Delta n = n_s - n_r$) is

$$\Delta n = \frac{c}{\omega d}\varphi, \tag{1.3}$$

where c is the speed of light, ω is the angular frequency of the wave, and d is the propagation distance in the medium. The absorption coefficient of a material, α, is determined from the Beer–Lambert law [29],

$$\frac{A_0}{A_1} = e^{\alpha d}, \tag{1.4}$$

where A_0 is the emitted electric field, and A_1 is the field detected at the receiver. If the generated field is constant between the reference and sample measurements, Equation 1.4 can be rearranged to give

$$\Delta\alpha = \frac{1}{d}\ln\left(\frac{A_r}{A_s}\right), \tag{1.5}$$

where $\Delta\alpha = \alpha_s - \alpha_r$. Dry air is a commonly used reference material in terahertz spectroscopy owing to its low loss ($n = 1$, and $\alpha = 0$), which simplifies calculation.

In practice, the propagation models applied to extract sample parameters are usually more complicated than those described here since they must account for artefacts that arise from the measurement system [30–32]. One of these more advanced models is implemented in Chapter 5.

The strengths of terahertz time-domain spectroscopy lie in the unique spectral properties that many materials exhibit in this frequency range. Owing to the long-range intermolecular motions that are accessed, structurally similar molecules may possess very different properties [33]. For example, the isomers L-isoleucine and L-leucine and their absorption spectra are pictured in Figure 1.4. Structurally, the CH_3 group is translated, but the atomic content of the two molecules is the same. Such a difference would not be detected with infrared spectroscopic techniques, as the individual bonds present are the same, but as the measured absorption coefficient shows, there are clear differences observed in the terahertz frequency range.

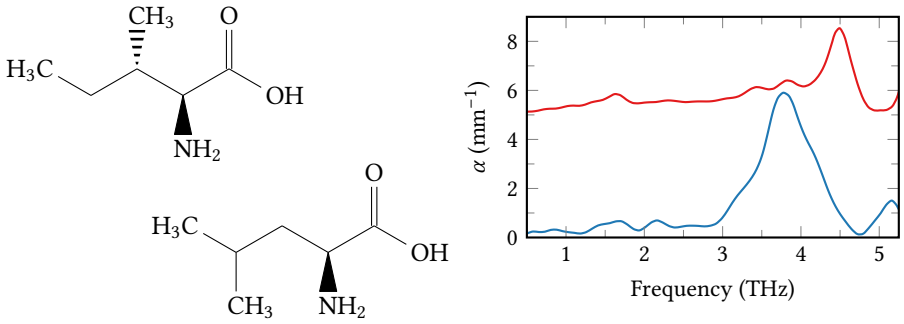

Figure 1.4: The absorption coefficient of the isomers L-isoleucine (top, red) and L-leucine (bottom, blue). The spectrum of L-isoleucine has been offset by 5 mm^{-1} for clarity. The structural differences between the two chemicals result in significant differences in the respective absorption coefficients, even though the atomic content is unchanged. The measurements were made with a free-space terahertz time-domain system using photoconductive emission and electro–optic detection schemes.

1.2.1 Free-space terahertz time-domain spectroscopy

The measurements shown in Figure 1.4 were made with a free-space broadband terahertz time-domain spectroscopy system that is capable of measuring sample properties between 300 GHz and 6 THz [34]. Systems such as this are widespread, and are commonly used for the measurement of solid, crystalline samples. In the most simple configuration, a femtosecond laser source is focused onto a photoconductive emitter, which emits terahertz radiation into free-space. The radiation is collected and collimated by a parabolic mirror, after which it is focused on a second switch, or electro–optic crystal by an additional mirror. The properties of a sample can be measured by positioning it in the collimated beam path [23], as shown in Figure 1.5.

Terahertz radiation is strongly attenuated by the many absorption lines of atmospheric water vapour, which may dominate measurements [9]. Therefore, most experiments are conducted within a sealed chamber that can be purged with dry air or N_2, thus reducing the attenuation of the pulse when propagating through free-space. If liquid samples are to be measured, the significant loss of terahertz-frequencies in water, and polar liquids in general, requires that the interaction volume between the sample and radiation is restricted in order to avoid attenuation of the signal to levels that cannot be distinguished from background noise. If samples are contained within a liquid flow-cell [32, 35], the narrow separation of the windows required results in many reflections, owing to the changes in permittivity that occur at the boundaries

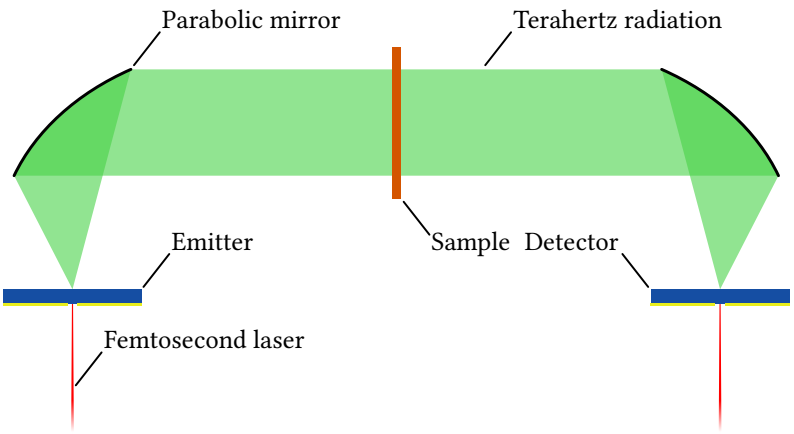

Figure 1.5: A simple free-space time-domain spectroscopy system in which a femtosecond laser focused on a photoconductive antenna results in the emission of terahertz radiation, which is collimated, transmitted through a sample, and then focused on a detector.

between the sample and window material. Etalons such as these complicate analysis, necessitating the use of a comprehensive system model that describes the various reflection sources, as is discussed further in Chapter 5. The problems caused by the introduction of windows can be overcome by flowing liquid films between suspended wires through surface tension [36]. However, the biconcave cross-section of the resulting film requires precise calibration to accurately determine the length of interaction between the sample and terahertz electric field [37].

1.2.2 Spectroscopy in waveguided systems

Assuming a spherical emission pattern, the power of an unguided wave, such as that emitted from a photoconductive antenna, will decrease according to the square of the distance from the source. While parabolic mirrors can be used to collimate, direct, and focus free-space beams of terahertz radiation, electromagnetic waves can also be confined to low-loss waveguide structures that allow more intricate mixing, splitting [38], and manipulation of propagating waves [39].

The rectangular waveguide is one of the most common waveguide structures, and is typically operated in the TE_{10} mode where the hollow metallic waveguide has width $\lambda/2$, and height $\lambda/4$, and λ is the wavelength of the low-frequency cut-off (the frequency below which the associated wavelength is too long to be supported). Rectangular waveguide is often excited with Schottky multiplier circuits that operate

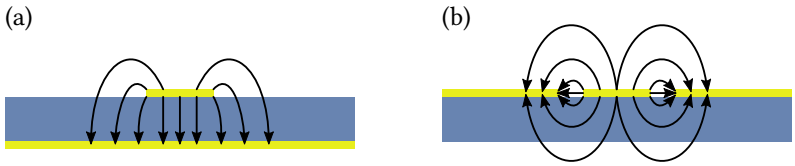

Figure 1.6: (a) A schematic of the electric field lines around a microstrip transmission line. The majority of the electric field is contained within the substrate, owing to the ground plane on the reverse face. (b) The electric field lines around coplanar line. The greatest electric field strength is found between the centre conductor and the adjacent ground plane.

over a relatively narrow frequency range, such as the WR-1.0 band that supports frequencies between 750 GHz and 1100 GHz, and are used to extend the output frequency range of a vector network analyser [40]. The cut-off frequency of rectangular waveguide is only a low-frequency limit, and multi-mode operation between 0.7 THz and 4 THz has been demonstrated by coupling free-space radiation emitted from a photoconductive antenna [41], through which it is also possible to sensitively extract the properties of a sample within the waveguide cavity [41]. Given that the peak field strength of the TE_{10} mode occurs along the centre of the waveguide, other spectroscopic techniques include the alignment of a sample vertically along the centre of the cavity [42], and the integration of microfluidic capillary tubes that contain a liquid sample [43].

The microstrip and coplanar transmission line are metallic waveguides that are patterned on a supporting substrate. In the microstrip geometry, the signal conductor and the ground plane are separated by the substrate material, whereas the signal conductor and ground plane are patterned on a single side of the coplanar waveguide substrate. As shown in Figure 1.6a, the electric field distribution around a microstrip geometry is primarily concentrated within the substrate material. Despite this, absorption features have been observed in overlaid samples of lactose monohydrate, well-known for the strong absorption mode that occurs at 534 GHz [44], but less dominant modes in other materials may not be so easily identified. The sensitivity of the interaction between the electric field supported by a microstrip transmission line and an overlaid material can be increased by the inclusion of band-stop quarter-wavelength stub filters [45]. The resonant frequency of a stub filter is dependent on the effective permittivity defined by the substrate and superstrate materials, which is increased by an overlaid sample material. The centre-frequency of the resonance

therefore shifts as a function of the sample permittivity, which yields information about the analyte at pre-defined frequency points. However, the number of resonant stub filters that can be incorporated onto a single transmission line is somewhat restricted by the bandwidth of the bandstop filter response.

Coplanar transmission lines that operate up to 1 THz [46,47] have been designed, but as shown in Figure 1.6b, the electric field is also primarily confined to the region between the conductor and ground plane. To efficiently support terahertz-frequency propagation, the separation between the centre-conductor and ground plane must be of the order of a few tens of microns [47]. While it may be possible to perform spectroscopic measurements of solid, non-conductive samples with microstrip and coplanar geometries designed for operation at terahertz-frequencies, the integration of a fluid system that is in sufficiently intimate contact to achieve sensitive interaction between the electric field and analyte, but does not electrically short the waveguide circuitry, would indeed be challenging.

The planar Goubau line offers a potential solution to this problem. A single wire suspended in free-space, known as the Sommerfeld line [48], can guide an electromagnetic field with lower attenuation than equivalent rectangular waveguide. However, as observed by Goubau [49], the radial extension of the field into free-space around the wire makes interference with surrounding objects a likelihood, particularly at longer wavelengths. Goubau therefore proposed a transmission line in which a wire is coated with a dielectric material that acted to better confine the field to the metal surface. As illustrated in Figure 1.7a, a freestanding Goubau line can be fed by a metallic horn that enables transition of the mode from other sources, and aids efficient coupling into the wire. The propagating field extends beyond the dielectric material, and is therefore sensitive to the permittivity of surrounding materials, albeit less sensitive than the Sommerfeld line. While the interaction with external influences may be undesirable for low-loss transmission, it is essential in spectroscopy [50].

At the turn of the millennium, a renewed interest in the geometry [51,52] inspired the development of the planar Goubau line, in which the cross-section of the free-standing wire was patterned on a dielectric slab [53]. As the field around the planar

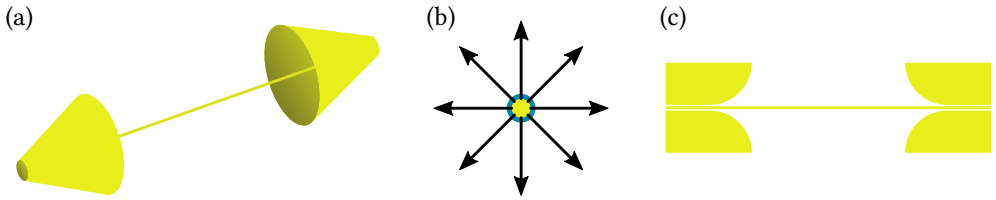

Figure 1.7: (a) A freestanding Goubau line that comprises a feed and receiver horn connected by a single dielectric-coated wire. (b) The electric field lines extend radially from the conductor. (c) The planar Goubau line was inspired by the cross-section of a traditional Goubau line and was originally fed from a coplanar transition region.

Goubau line extends both into and out of the substrate, it interacts strongly with overlaid samples, such as crytalline solids [54], and liquids confined to channels [55]. With this discovery, the development of on-chip spectroscopy with planar Goubau lines may seem to be a foregone conclusion. However, while analytical models exist for rectangular, microstrip, and coplanar waveguides [56, 57], the Goubau line is as yet without solution, and analysis is restricted to the use of finite-element methods to numerically solve Maxwell's equations [50, 58]. For this reason, the scope of sample parameter extraction has been limited to measurements of relative delay and attenuation changes caused by samples brought near to the transmission line [59], or changes to the scattering parameters of a waveguide induced by an overlaid material [60]. In this work, a method that combines the results of finite-element simulations and spectroscopic measurements is introduced, which enables extraction of the frequency-dependent permittivity of a sample positioned over a planar Goubau line.

1.3 Liquid spectroscopy at terahertz frequencies

Microfluidic systems are those in which channels with dimensions between tens and hundreds of micrometers are used to manipulate small (10^{-9} to 10^{-18} litre) liquid volumes [61]. At these length-scales, interfacial forces, surface tension, and capillary effects dominate over gravitational forces, which results in predictable, easily controlled laminar flows that simplify the modelling of diffusion and mixing mechanisms [62]. Given the strong absorption of terahertz radiation in polar liquids, the use of microfluidic systems to reduce interaction volumes has increased in both

free-space [32, 35, 63], and on-chip [55, 60] applications in recent years.

The potential biochemical applications of microfluidic technologies are far-reaching. For example, efforts have been made to replicate physiological functions in 'organ-on-a-chip' devices that aim to emulate *in vivo* environments in more easily controlled *in vitro* experimental conditions [64]. Preliminary developments include lung [65], intestine [66], and kidney [67] simulants. It has also been shown that Raman spectroscopy can be performed within a device in real-time to monitor the catalysis of isopropanol into acetone [68]. Given the interesting molecular dynamics that occur on picosecond timescales (corresponding to the terahertz frequency range) [2, 69], it is possible that the direct integration of a terahertz spectrometer and microfluidic system could be used to reveal more information about reaction dynamics [70], hydration [71], and molecular conformation [72]. However, to do so would require the development of robust on-chip analogues to the well-established free-space spectrometers that have been used to probe various biological systems.

Early on-chip microfluidic devices were fabricated on glass substrates [73], but more recently a wide range of polymers have been used owing to the greater range of chemical and mechanical properties available [74, 75]. The elastomer polydimethylsiloxane (PDMS) is possibly the most commonly selected biocompatible material with which microfluidic components can be moulded and bonded [76] to construct intricate three-dimensional geometries [77]. PDMS is typically supplied as a viscous liquid elastomer and a separate curing agent, and can therefore be poured over a rigid mould master and cured, before then being peeled away to create an accurate replica of the mould surface [78]. To create sealed microfluidic channels, a moulded PDMS device is typically bonded to either a rigid substrate [75], or capped with another layer of the elastomer to produce a flexible chip [79].

As explored in Figure 1.1, the growth of the microfluidics field has been rapid, but some argue that the most significant progress has been made within engineering and the physical sciences, and that ground-breaking microfluidic applications that attract the wider interest of the biomedical community are yet to be invented [80]. It is here proposed that the development of an on-chip microfluidic spectrometer capable of extracting the complex frequency-dependent dielectric properties of unknown liquid

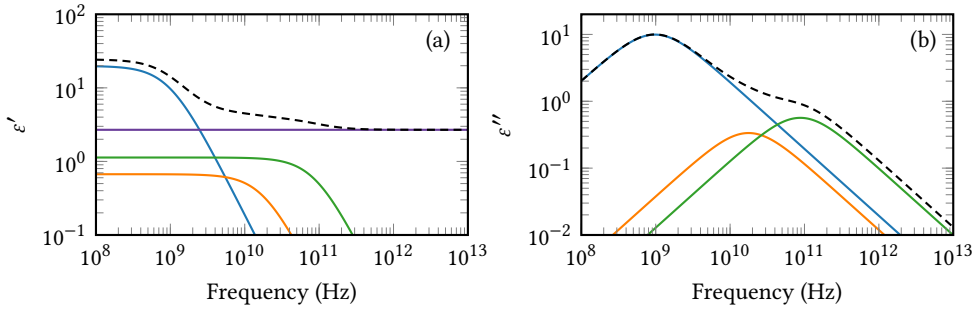

Figure 1.8: The (a) real and (b) imaginary components of the triple-Debye relaxation model of ethanol as described by Barthel et al. [82]. Each of the components (solid, coloured) are summed to determine the frequency-dependent sample permittivity (dashed, black).

samples may pave the way for future biological technologies.

1.3.1 The Debye relaxation model

The complex frequency-dependent dielectric response of polar liquids is typically described with the Debye relaxation model, which was originally developed to describe atomic lattice thermodynamics [81], but can also be applied to the reorientation of polar liquids [82]. A polarisation is established when an electric field is applied to a polar liquid, owing to the alignment of molecular dipoles, which has an associated time constant and permittivity. In many samples there may be multiple relaxation processes that occur simultaneously, in which case the complex permittivity of the material is the summation of each of these terms [83]. The general dielectric function, $\tilde{\varepsilon}_{\mathrm{D}}$, for n relaxation processes describes the frequency-dependent permittivity of a material as it varies from the static DC value to the high-frequency limit, ε_∞. At higher frequencies, around 1 THz, vibrational modes with a resonant frequency ω_i and damping rate κ are also accessed, such that the complete dielectric function is [83],

$$\tilde{\varepsilon}_{\mathrm{D}} = \varepsilon_\infty + \sum_{i=1}^{n} \frac{\varepsilon_i - \varepsilon_{i+1}}{1 + \mathrm{j}\omega\tau_i} + \sum_{i=1}^{m} \frac{A_i}{\omega_i^2 - \omega^2 - \mathrm{j}\omega\kappa_i}, \tag{1.6}$$

where ω is the angular frequency, ε_i and τ_i describe the n relaxation processes, and A_i is the amplitude of the m resonant modes. Figure 1.8 shows the Debye relaxation model of ethanol as described by Barthel et al., which comprises three relaxation process, and no resonant modes [82].

Fitting a Debye model to the complex permittivity of a measured sample can re-

veal information about structural changes that occur as a result of chemical reaction. For example, water and ethanol are best represented by double ($n = 2$) and triple ($n = 3$) relaxation models respectively, with no vibration terms ($m = 0$). However, when mixed, a resonant mode is introduced ($m = 1$) owing to the intermolecular interaction between the two liquids, and changes in the dielectric strength of the relaxation terms correlate with the exothermic mixing enthalpy of the two components [83]. The flexibility of the Debye model is also the key weakness in its implementation, and care must be taken to suitably constrain the fitting process. Fitting processes, and some of the issues involved, are discussed in more detail in §4.3.5

1.4 Concluding remarks

The fields of terahertz spectroscopy and microfluidics have independently attracted much interest from their respective research communities, yet efforts to integrate the two technologies are in their infancy. The information about hydration, and biomolecular dynamics that can be accessed on picosecond timescales, and the precise control of analytes that is possible in microfluidic circuits shows considerable promise. However, the tools with which to perform accurate terahertz-frequency measurements of liquid samples contained within microfluidic systems have not yet been established. Over the following chapters, the design of a microfluidic on-chip terahertz spectrometer will be discussed, and a method for the extraction of the complex permittivity (and therefore absorption coefficient and refractive index) of an unknown liquid sample will be presented.

Chapter 2

The Simulation of Goubau Line Properties

As discussed in Chapter 1, traditional analytical efforts to define the characteristic impedance or permittivity of the planar Goubau mode have been unsuccessful. Several treatments have described the electromagnetic field distribution [49, 84, 85], yet these expressions cannot be adapted to allow calculation of the waveguide geometry impedance (as is possible with microstrip and coplanar systems), owing to the lack of a defined ground plane at which the electric field is terminated.

Given the restrictions to an analytical approach, numerical solutions are often employed to allow some analysis of planar Goubau propagation modes [86]. Typically, this involves calculation of the electromagnetic field around the waveguide structure by dividing a model into many cells, within which the local field can be more easily computed. For such a method to produce accurate results, the cells each must be sized such that the electric field gradient within is minimised. Therefore, micrometer-scale cells are required to calculate the distribution of a terahertz-frequency field; the use of such a method is computationally expensive, and structures comprising several hundred thousand elements require tens of gigabytes of memory.

Several software packages have been used in the analysis of planar Goubau line, including Comsol [86], Microwave CST [58], and Ansys HFSS [87]. The methods

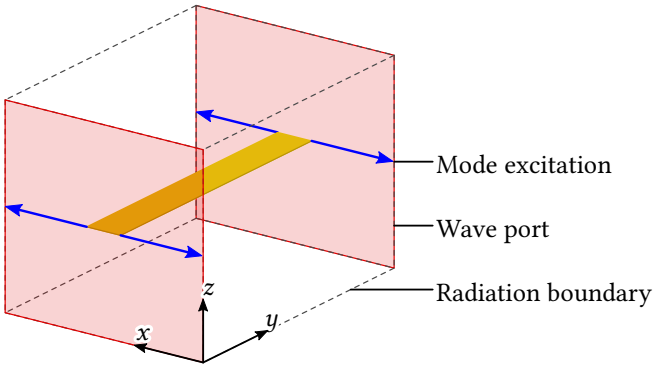

Figure 2.1: A simple model of a single-wire conductor used for simulation purposes. An electromagnetic field is excited at the wave ports indicated, and the model is defined within a radiation boundary that simulates an infinite extension into free-space.

employed by each of these packages are fundamentally similar, and HFSS is used in this work.

2.1 An introduction to simulation with HFSS

In the High-Frequency Structural Simulator (HFSS, Ansys Inc.), a three-dimensional representation of the waveguide structure is defined with polygonal components, positioned within a simulation boundary. Figure 2.1 shows an exemplar planar single-wire conductor, suspended in a region of free-space, within the confines of a radiation boundary. The radiation boundary is assumed to be perfectly matched to any adjacent geometry, such that incident waves are not reflected, which would introduce model-artefacts into the simulation. Wave propagation in the model is investigated through the definition of ports at which an electromagnetic field can be stimulated along the lines of excitation indicated in the Figure. In coplanar and microstrip geometries, wave ports (and excitations) are usually terminated at the ground plane. However, the planar Goubau line does not have a clearly-defined termination, hence the field extends an infinite distance from the conductor, which is represented in the model by termination at the radiating boundary. Owing to the relatively large extent of the evanescent field about the planar Goubau line, the boundary dimensions must be appropriately sized such that the majority of the field is contained within the modelled domain. As will be shown, the field distribution is dependent on both the wavelength in question, and the permittivity of the surround-

ing materials. Therefore, it is not appropriate to present rule-of-thumb definitions for suitable model dimensions, and they must be determined per application.

In order to model a wide range of structures, HFSS is packaged with a library of materials that can be assigned to the device components. Typically, these values are measured at a single microwave frequency (around 1 GHz). While sufficient for investigating the effects of various design parameters, the development of the accurate on-chip spectrometer discussed in Chapter 4 required that more precise frequency-dependent material properties were entered manually. The process of improving model accuracy in order to accurately represent a practical device is discussed in more detail in §4.3.2.

2.1.1 Refining the model mesh

In the finite element method, the waveguide structure is converted into a three-dimensional mesh of elements within which the electric field gradients are minimised, such that the field at any point in the geometry can be accurately estimated by interpolation between the adjacent calculated points. To achieve this, the structure is first converted into a coarse mesh using a Delaunay tessellation method, in which neighbouring object vertices are joined with tetrahedral elements. The electric field in each element is then calculated at the highest frequency to be modelled (e.g. 1 THz), and the mesh-elements with the greatest field gradient (typically those surrounding the smaller features of the conductor) are sub-divided to increase the spatial-resolution, and therefore the accuracy of further field-interpolation.

As the field gradient is minimised in each mesh element, the introduction of high-permittivity materials requires the use of smaller (and therefore more) mesh elements. For example, Figure 2.2a shows a cross-section of the initial mesh defined around a 30-µm-wide planar Goubau line on a high-permittivity ($\varepsilon = 4$) substrate material, with an overlaid 4-µm-thick layer of dielectric material ($\varepsilon = 3$). The geometry was confined to a 1 mm^3 boundary. During each iteration of the mesh refinement process, the waveguide S-parameters were calculated, and compared to those of the previous mesh. The mesh is deemed to have converged to a sufficiently accurate solution when the difference between two subsequent iterations is less than 2 %. Figure 2.2b

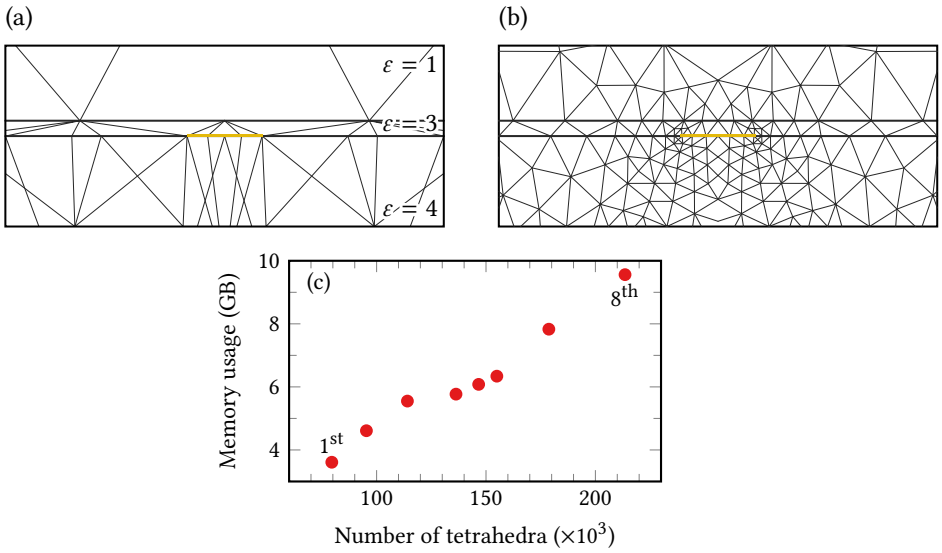

Figure 2.2: (a) A sample of the cross-section of the initial mesh created for a solution frequency of 1 THz around a 30-µm-wide planar Goubau line (yellow), on a supporting substrate, with an overlaid 4-µm-thick layer of dielectric material. (b) After eight iterations, the convergence criterion was met, and the final mesh produced. (c) The number of tetrahedra and memory required to simulate the full three-dimensional model per iteration, as labelled.

shows the converged mesh that was achieved after eight refining iterations, resulting in the creation of 200,000 mesh elements that required 10 GB of memory to model, as shown in Figure 2.2c. The smallest mesh elements are found closest to the conductor (where the greatest field gradient is observed), and also in the high-permittivity substrate and overlaid dielectric materials. To ensure a stable solution, the solver can be configured to require that multiple consecutive iterations meet the convergence criterion. Once established, a stable mesh is suitable for use at any frequency below that used in its creation. Therefore, the broadband response of a particular geometry can be calculated using a single mesh.

2.1.2 Modelling waveguide characteristics

The properties of a waveguide, such as its effective permittivity or loss, are dependent on the interaction between the supported modes of propagation and the surrounding materials. Figure 2.3 shows a cross-section of the electric and magnetic field distribution around a 30-µm-wide planar Goubau line supported by a 100-µm-thick substrate ($\varepsilon = 4$), as calculated with HFSS at 100 GHz and 500 GHz. As shown in Figure 2.3a, the evanescent field around the transmission line is approximately ra-

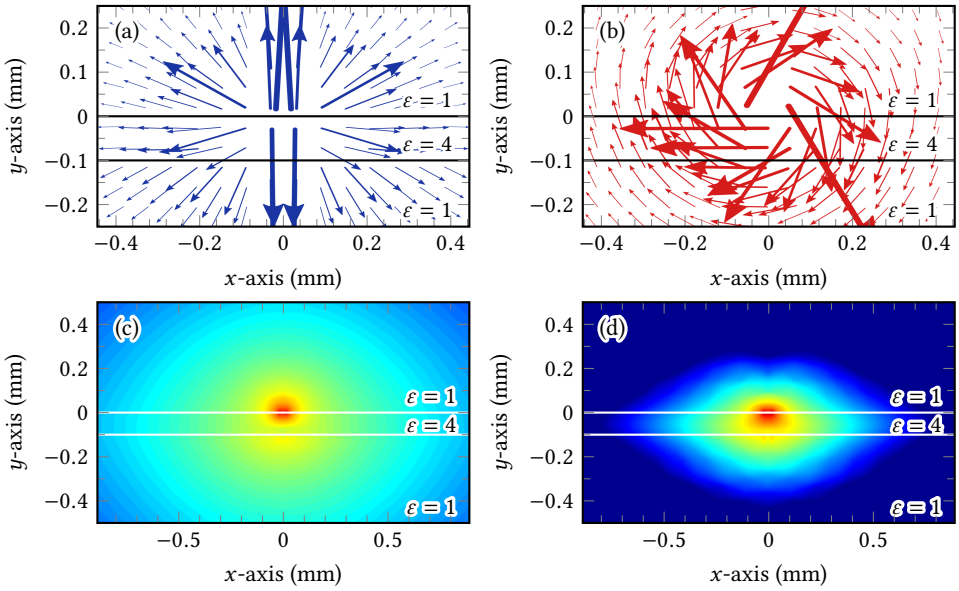

Figure 2.3: Vector plots of the (a) electric and (b) magnetic field magnitudes around a planar Goubau line patterned on a 100-µm-thick substrate ($\varepsilon = 4$), as calculated by HFSS at 100 GHz. Arrow size indicates the strength of the field at the vector origin. (c) The electric field distribution around the transmission line at 100 GHz and (d) 500 GHz. For clarity, a 1.8 mm × 1 mm cropped region of a larger simulation domain is shown. The absolute values of electric field are arbitrary, but the same logarithmic colour scale has been applied in both (c) and (d).

dial, as it extends away from the transmission line in all directions, whereas the magnetic field circulates the conductor, as indicated in Figure 2.3b. As shown in Figure 2.3c, the evanescent field around the transmission line is approximately circular at the low-end of the supported frequency range. Previously, this circular distribution has been exploited, and the effective permittivity of the mode has been estimated with simple trigonometry [54]. In theory, the expressions described in Reference 54 would allow calculation of the effective permittivity, without the use of computationally expensive simulations. However, as shown in Figure 2.3d, the field distribution is also frequency-dependent, and the circular nature is not maintained across all frequencies, which introduces a systematic error into the trigonometric approximations.

At each simulated frequency point, HFSS can calculate a wide range of waveguide parameters, including the effective permittivity and propagation coefficient. For example, Figure 2.4a shows the frequency-dependent effective permittivity of the Goubau mode for the structure shown in Figure 2.3. Given that the extent of

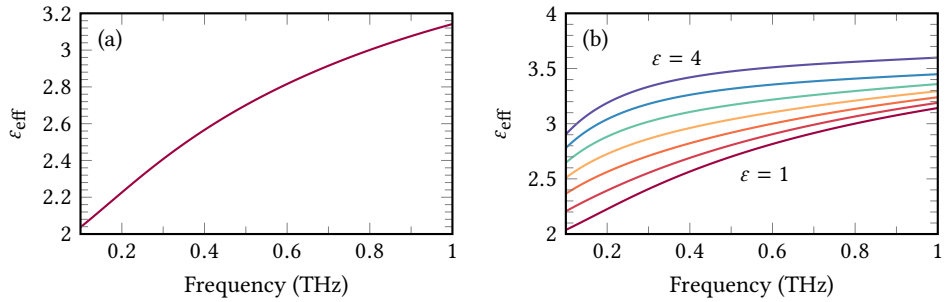

Figure 2.4: (a) The frequency-dependent effective permittivity, ε_{eff}, of the Goubau mode for the device structure shown in Figure 2.3. The decrease in wavelength at higher frequencies results in an increase in effective permittivity as the interaction between the field and air is reduced relative to the interaction between the field and substrate. (b) The simulated ε_{eff} of the same structure as the permittivity of the overlaid material is increased from $\varepsilon = 1$ (red) to $\varepsilon = 4$ (blue) in increments of 0.5.

evanescent field decreases as a function of frequency, the interaction between the field and surrounding air is reduced relative to the interaction between the field and substrate. Thus, the effective permittivity, ε_{eff}, of the propagation mode increases with frequency.

In spectroscopic applications, such as those considered in this work, an unknown material is brought into the vicinity of the transmission line, such that it is probed by the evanescent field. As discussed in Chapter 4, the resulting change in the propagation mode can be measured to determine the analyte permittivity. For example, Figure 2.4b shows the simulated ε_{eff} of the geometry in Figure 2.4a as the permittivity of the overlaid material was increased from $\varepsilon = 1$ to $\varepsilon = 4$. In this illustration, the permittivity of the simulated material was frequency-independent; in practice, the dielectric properties of most liquid samples vary across the terahertz frequency-range, therefore necessitating the development of a frequency-dependent permittivity extraction technique.

2.2 Concluding remarks

Throughout this work, HFSS models are used to compliment and interpret experimental data. In Chapter 3, the results of HFSS simulations are used to develop a better understanding of the propagation modes supported by a planar Goubau line patterned on a dielectric slab, including the introduction of reflections at waveguide

meanders, and the generation of unwanted substrate modes at high-frequencies. In Chapter 4, a numerical method is introduced in which the complex permittivity of an analyte measured within an on-chip terahertz-frequency spectrometer is determined with the use of an accurate HFSS model of the experimental device geometry.

Chapter 3

The Design of Planar Goubau Lines for Spectroscopy

Previous studies of on-chip terahertz-frequency waveguides, and planar Goubau lines in particular, have focused on increases in bandwidth [88], as well as investigating the sensitivity of propagating fields to proximal samples, thereby allowing the waveguides to be used for spectroscopic measurements [44, 54, 60, 89]. Given the relative infancy of the technologies employed in on-chip terahertz spectroscopy, there is still much to be learned about the factors that dictate the performance of any given design. In this work, particular attention was paid to the design and characterisation of planar Goubau lines for application in terahertz time-domain spectroscopy, and therefore the fabrication of low-noise, high frequency resolution devices that were sensitive to changes in the dielectric properties of proximal samples was investigated.

3.1 Fabrication of a planar Goubau line on quartz

A typical on-chip device comprises two pairs of photoconductive switches formed from LT GaAs, which are separated by a length of transmission line formed from vapour-deposited metal, all on a host substrate which both provides support and defines the electrical properties of the device. The first devices produced in this work were patterned on quartz substrates, a material that is commonly used for the fabrication of planar Goubau lines owing to its low loss ($\alpha < 2\,\mathrm{cm}^{-1}$ [90]) and

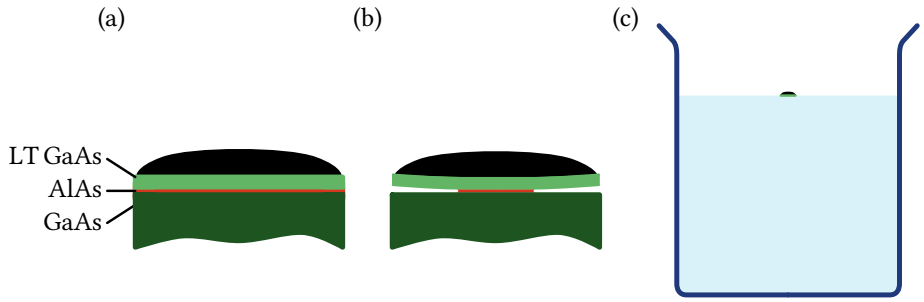

Figure 3.1: (a) Black wax was deposited onto the top surface of an LT GaAs wafer. (b) The sacrificial AlAs layer was removed by etching with HF acid; tension applied by the black wax aids the diffusion of gaseous products, and replenishment of HF etchant. (c) The surface tension of water was used to transport the released LT GaAs material.

relatively low permittivity ($\varepsilon \sim 4.5$ [91]) in the terahertz frequency range [54, 92]. In general, the fabrication process used was based on that pioneered in the Leeds group by Wood et al. [21, 93], and further developed upon by Russell et al. [54, 88, 94].

3.1.1 The LT GaAs transfer process

The epitaxial transfer process described here is a modification to the process described in Reference 21. Here, the process duration has been reduced, and several modifications have been highlighted that aim to reduce stresses in the thin LT GaAs film.

A 350-nm-thick layer of LT GaAs was grown at ~200 °C using molecular beam epitaxy, on a 100-nm-thick layer of AlAs, itself grown on a 500-µm-thick GaAs wafer. A section (typically 2 mm × 2 mm) was cleaved from the wafer by scribing along the crystallographic planes, as determined from the wafer major flat. The piece of LT GaAs wafer was then cleaned in acetone, isopropanol (IPA), and deionised (DI)-H_2O by agitation in an ultrasonic bath (Sonorex Super 10 P, Bandelin) for five minutes per solution and then dried in N_2, after which any remaining organic residue was removed by exposure to a 50 W O_2-plasma for five minutes (EMS 1050, Electron Microscopy Sciences). The LT GaAs was then annealed *ex situ* at 575 °C to precipitate the arsenic, as described in §1.1.2. After annealing, black wax (Wax W, Apiezon) was melted onto the surface of the LT GaAs at 110 °C to form an etch mask, to aid lift-off of the LT GaAs by applying tension [20], and permit easier handling of the 350-nm-thick material after release, as shown in Figure 3.1a. The tension applied by

the black wax aids the diffusion of H_2 gas produced in the etching process, which reduces micro-cracking of the LT GaAs, whilst also allowing the replenishment of fresh HF reactant during etching.

The wax-coated wafer was placed in a H_2SO_4:H_2O_2:H_2O solution (1:8:40 by volume) for two minutes to etch the exposed sidewalls (removing any oxide layer that may have formed on the AlAs), after which it was transferred to a HF:H_2O solution (1:4 by volume), stored in a refrigerator at 6 °C, and left for 24 hours, during which time the AlAs layer was selectively etched, as illustrated in Figure 3.1b, and the LT GaAs released. The liberated LT GaAs was transferred to a beaker of DI-H_2O, where, as shown in Figure 3.1c, the surface tension of the water was used to suspend the semiconductor.

Simultaneously, an appropriately-sized section of fused quartz (typically around 20 mm × 20 mm) was cut from a single-side polished wafer using a wafer saw (Microace 66, Loadpoint) fitted with a resin blade, driven at 22 krpm. The quartz substrate was then cleaned with acetone, IPA and DI-H_2O, dried, and plasma ashed in the same manner as the LT GaAs. A vacuum tool was used to manipulate the fragile wax-coated LT GaAs, and position it on the cleaned, polished quartz surface; any residual water trapped at the LT GaAs–quartz interface following transfer was wicked away using a cleanroom tissue, promoting adhesion between the two surfaces. The quartz was then moved to a hot plate heated to 80 °C, to soften the wax, while also allowing the LT GaAs to form an intimate contact with the quartz as any remaining water was evaporated. The hot plate was then turned off after one hour, and the quartz wafer allowed to cool naturally, to minimize thermal stresses in the wax, which might otherwise induce micro-cracking in the LT GaAs. The LT GaAs-on-quartz was then placed in a vacuum oven (VD 53, Binder), which was pumped down to 30 mbar, and then baked at 80 °C for 15 hours, during which an LT GaAs–quartz bond was formed. Upon removal from the vacuum oven, the black wax was removed from the LT GaAs by dissolving it in trichloroethylene, after which the LT GaAs-on-quartz was cleaned in acetone, IPA, and DI-H_2O (without ultrasonic agitation, to avoid damage to the LT GaAs). As shown in Figure 3.2a, air or water can become trapped between the LT GaAs and quartz during the bonding process,

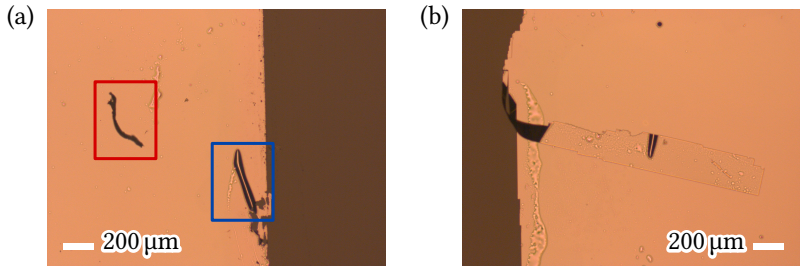

Figure 3.2: Micrograph of transferred LT GaAs-on-quartz. (a) Water or air trapped at the interface has caused wrinkling of the semiconductor (blue), and has also resulted in the LT GaAs being completely removed (red). (b) A weakly bonded section of LT GaAs has been lifted, folded, and redeposited during the wax removal process.

which can create wrinkles in the semiconductor, or cause regions to break off completely. Sections of LT GaAs that have bonded weakly to the quartz may also be delaminated during the wax-removal process, and can be deposited elsewhere on the device as shown in Figure 3.2b. Given that the LT GaAs in these areas would be of an unknown quality and thickness, they were avoided when selecting regions to be used for forming photoconductive switches.

3.1.2 Fabrication of photoconductive switches

To improve the transmission characteristics of an on-chip device (see §3.3.2), it is preferable to remove any LT GaAs that is not used in the generation or detection of picosecond pulses, owing to its high permittivity. This is achieved by lithographically defining switches of the appropriate size, shape, and separation, and then chemically etching the waste material as follows:

First, a 1.4-µm-thick layer of S1813 positive photoresist (Microposit) was deposited over the LT GaAs-on-quartz by spin-coating at 4000 rpm, followed by a four minute bake at 110 °C. The resist was exposed to ultraviolet (UV) light (20 mW cm^{-2}) for two seconds through a light-field mask, on which two squares, separated by the length of the transmission line were patterned. After exposure, the resist was baked again for 30 s, to improve the straightness of the sidewalls, and developed in MF-319 (Microposit) for one minute. The unwanted, exposed LT GaAs was then removed by etching in a dilute H_2SO_4:H_2O_2:H_2O solution (1:8:950 by volume) for 10 minutes so that only the two LT GaAs mesas remained, as shown in Figure 3.3a, ready for deposition of the switch-defining metals.

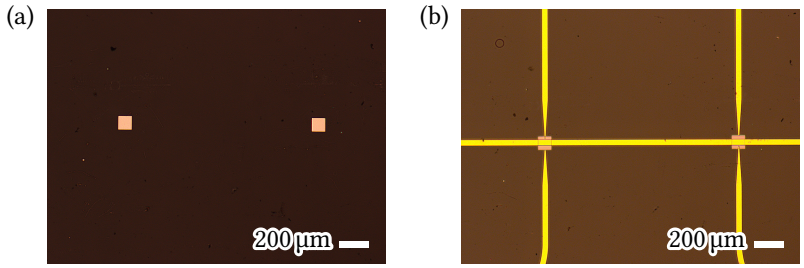

Figure 3.3: (a) Micrograph of two 70 µm × 70 µm LT GaAs mesas, separated by 1 mm, after etching of the unwanted material. (b) The same LT GaAs squares after deposition of a Ti/Au PGL transmission line with integrated photoconductive switches.

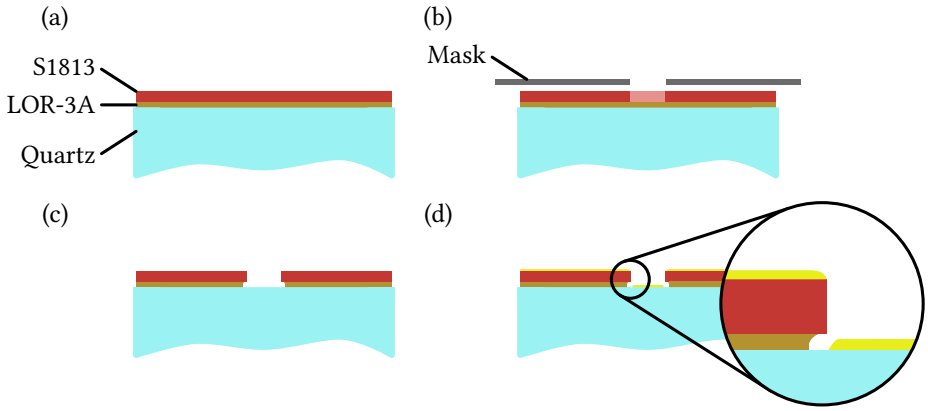

Figure 3.4: The bilayer resist metallisation process. (a) LOR-3A and S1813 were spun onto a quartz substrate, and (b) the S1813 was exposed to UV-light through an optical mask. (c) MF-319 was used to develop the S1813, and a second immersion in MF-319 etched the LOR-3A sidewalls, creating an undercut. (d) During metallisation, the undercut aided separation of the unwanted Ti/Au deposited on the resist and the metal that was deposited on the quartz substrate.

The metal regions of the photoconductive switches and transmission line were fabricated using a lift-off technique in which photoresist was patterned with an undercut, to achieve clean separation of the metal deposited on the resist and that on the substrate. An undercut can be created by partially curing the top-surface of S1813 with chlorobenzene, so that it is more resistant to the MF-319 developer. However, the poor adhesion between quartz and S1813 makes this standard lithographic technique unsuitable, and therefore a bilayer technique, illustrated in Figure 3.4, was adopted.

In the bilayer process, the device was first cleaned in organic solvents and an O_2-plasma (as discussed previously) after which a layer of hexamethyldisilazane (HMDS) adhesion promoter was spun on at 5000 rpm for 30 s, and baked at 200 °C for one minute. HMDS is both toxic and flammable; the device was therefore carefully

cleaned of any excess HMDS using IPA, followed by a further one-minute-long, 200 °C bake. LOR-3A (MicroChem) lift-off resist was then spun onto the device at 2000 rpm for 30 s to create a 400-nm-thick layer that was baked at 200 °C for five minutes. Finally, the device was spin-coated with a layer of S1813.

The S1813 was exposed to UV light through a lithographic mask to define the photoconductive switches, bias arms, and PGL transmission line, after which it was baked at 110 °C to improve the sidewall definition. The photoresist was first developed by immersion in MF-319 for one minute to expose the underlying LOR layer in the device pattern, after which the remaining S1813 was hard-baked at 200 °C to prevent further development. An undercut was defined in the LOR by returning the device to MF-319 for an additional minute, during which the exposed LOR was etched. The development process was halted by washing in DI-H_2O, and the device was prepared for metallisation by ashing in a 50 W O_2-plasma for 40 s.

Metal was deposited using either an electron beam evaporator (Leybold), or a thermal evaporator (Auto306, Edwards). The high conductivity of Au means that it is well-suited for high frequency waveguides, and its inert nature prevents the formation of oxide layers during processing and measurement. However, Au does not bond well to quartz substrates, so a 10-nm-thick Ti adhesion layer was deposited before a 150-nm-thick layer of Au [95]. After metallisation, the unwanted Ti/Au was removed by dissolving the LOR in cyclopentanone, leaving a PGL pattern as shown in Figure 3.3b.

3.1.3 External connections

The PGL devices fabricated in this work comprise multiple photoconductive switches that can be independently biased or measured as required. To interface with external instruments, black wax was used to bond devices to a copper clad printed circuit board (PCB) that had been patterned with an appropriate number of break-out bond pads. Electrical interconnects between the PCB and chip were made using Au-wire, and external instruments were connected to the PCB using a custom ribbon-cable socket, or SubMiniature version A (SMA) coaxial connectors, depending on the number of connections that were required, as illustrated in Figure 3.5.

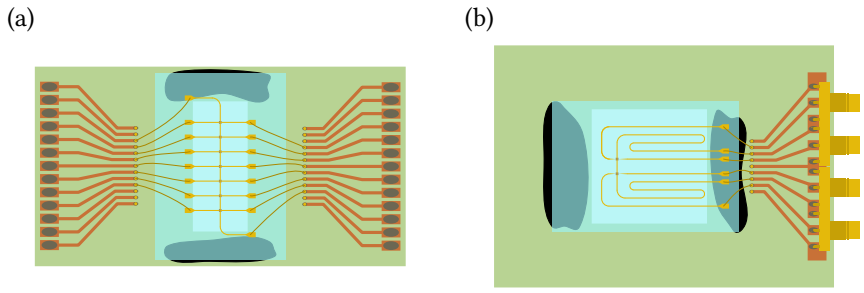

Figure 3.5: (a) Schematic of a device with many switches bonded to a PCB using black wax. A custom ribbon-cable socket is used to interface with external instrumentation. (b) An on-chip planar Goubau line device mounted to a PCB that is fitted with coaxial SMA lugs for external connections.

3.1.4 Experimental configuration of the on-chip terahertz time-domain spectroscopy system

The on-chip terahertz time-domain spectroscopy system used in the majority of this work is illustrated in Figure 3.6. Near-infrared (NIR) pulses were produced by pumping a femotosecond Ti:sapphire laser (Tsunami, Spectra-Physics) with a 7.42 W, 532 nm source (Millennia Xs, Spectra-Physics). The resulting femtosecond pulses had an average power of 800 mW, with a central wavelength of 800 nm, an 80 MHz repetition rate, and a full-width at half-maximum bandwidth of ~13 nm, which equate to a pulse energy of 10 nJ with a duration of ~100 fs. Using a 1:1 beam splitter, pulses were divided into a pump beam for the generation of terahertz-frequency electric fields by illuminating a biased photoconductive switch; and a probe beam for their detection at a second switch after propagation along the device.

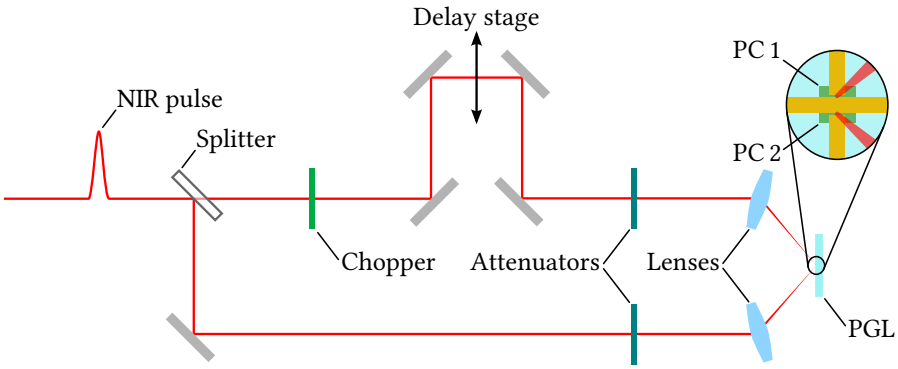

Figure 3.6: Schematic of the on-chip terahertz time-domain spectroscopy system used in this work. The NIR laser pulse is split into a pump, and a probe beam. The pump beam is attenuated and focused onto the generating switch, while the detection beam is optically chopped, passed through a delay stage, attenuated, and then focused onto the detection switch.

The pump beam was attenuated to the desired power using a variable neutral density filter, and focused onto PC 1. The probe beam was optically chopped at a rate of ~1.8 kHz, and mechanically delayed by a linear stage before it was attenuated and focused on PC 2.

The pump and probe beams were aligned to their respective photoconductive switches by applying a 10 V bias from a source-measure unit capable of simultaneously measuring picoamp currents (Keithley 2400). The position of the incoming beam on the switch was adjusted using a two-axis mirror mount and a lens in order to maximise the measured photocurrent. After alignment, a bias was applied to PC 1, and PC 2 was connected to a lock-in amplifier (Signal Recovery 7265) that was synchronised to the frequency of the optical chopper.

3.2 On-chip photoconductive switch characterisation

To perform spectroscopic measurements, a device should be designed and measured in such a way that the signal-to-noise ratio across the broadest available bandwidth is maximised. Maximising pulse amplitude is also advantageous for the measurement of strongly absorbing samples—such as the liquids considered in most microfluidic experiments. In the following sections, the characteristics of LT GaAs-based photoconductive switches designed for the generation of picosecond pulses are investigated, and observations are made about the influence of several design and measurement parameters. In photoconductive terahertz generation, the main device characteristics over which we have control, and that will affect the pulse amplitude and bandwidth are: the photoconductive switching and substrate materials, the switch geometry and bias, and the illuminating laser power. As discussed, quartz is a suitable substrate material, and LT GaAs is widely considered to be one of the best photoconductive switching materials, and will therefore be kept constant. The following sections will therefore investigate the effect of the remaining criteria on the amplitude, bandwidth, and signal-to-noise ratio of the on-chip terahertz pulse.

3.2.1 Influence of bias and laser power

In order to understand how switch bias and laser power dictate pulse generation, we must first consider the mechanisms involved in the production of terahertz radiation. In photoconductive generation, radiation is produced by first applying an electrical bias across a region of semiconductor material. The semiconductor is chosen to have an appropriate bandgap to allow the excitation of photo-generated charge carriers when illuminated using a pulsed laser beam. A pump laser is then focused onto the biased semiconductor, exciting charge carriers in the material, which are then accelerated by the local field. In LT GaAs, the excited carriers have sub-picosecond lifetimes, owing to the presence of precipitated As trapping sites, formed during MBE growth in an As overpressure [14]. The generation of carriers by a laser pulse illuminating a photoconductive material is given by

$$\frac{dn_\mathrm{f}}{dt} = -\frac{n_\mathrm{f}}{\tau_\mathrm{c}} + G \tag{3.1}$$

where n_f is the free carrier density, τ_c is the carrier trapping time, and G is the rate of carrier generation as a result of the laser pulse [12]. The generation rate is a time-dependent Gaussian function of the pump pulse duration, δt, which was kept constant in this work,

$$G(t) = n_0 e^{\left(\frac{-t^2}{\delta t^2}\right)}, \tag{3.2}$$

where n_0 is the carrier density at $t = 0$. As the generation process involves the spatial separation of electron and hole charge carriers, a localised space-charge polarisation, P_sc, is induced which acts to screen the applied electric field, E_b, such that the local field, E_l is [16]

$$E_\mathrm{l} = E_\mathrm{b} - \frac{P_\mathrm{sc}}{\eta \varepsilon'} \tag{3.3}$$

where η is a geometric factor of the photoconductive material ($\eta = 3$ for an isotropic dielectric material [16]). The polarisation factor is dependent on the number of charge carriers generated by the pump pulse, and therefore increases with laser power, which in turn increases the magnitude of the screening effect [96, 97]. The carriers generated by the excitation pulse are accelerated by the local electric field,

such that

$$\frac{dv_{\mathrm{e,h}}}{dt} = -\frac{v_{\mathrm{e,h}}}{\tau_{\mathrm{s}}} + \frac{Q_{\mathrm{e,h}}}{m^*_{\mathrm{e,h}}} E_{\mathrm{l}} \tag{3.4}$$

where v is the average carrier velocity, τ_{s} is the average time for the carriers to relax from the excitation, Q is the carrier charge, m^* is the effective carrier mass, and the subscripts e and h refer to electrons and holes respectively. If the relative difference in electron and hole velocity is defined as $v = v_{\mathrm{e}} - v_{\mathrm{h}}$, then the terahertz electric field, E_{THz} can be expressed as [12]

$$E_{\mathrm{THz}} \propto Q_{\mathrm{p}} v \frac{dn_{\mathrm{f}}}{dt} + Q_{\mathrm{p}} n_{\mathrm{f}} \frac{dv}{dt}, \tag{3.5}$$

where Q_{p} is the charge on a proton. The first term of Equation 3.5 describes the contribution to E_{THz} made by the generation of charge carriers, and the second term describes the contribution made by the acceleration of those carriers. When the polarisation-induced screening effect is small, as it is for low bias and pump powers, E_{THz} would be expected to scale linearly with bias and pump power.

The magnitude of the screening effect is strongly-dependent on the photoconductive switch geometry used. This was demonstrated by Tani et al. [96], who measured the terahertz generation characteristics of a stripline, dipole, and bow-tie antenna, shown in Figure 3.7. The terahertz power emitted from each antenna, which is proportional to E^2_{THz}, was measured using a bolometer for a fixed pump laser power, and was found to increase quadratically with applied bias (therefore E_{THz} increased linearly). However, when a fixed bias was applied to the switches and the pump laser power was varied, a linear relationship between pump power and E_{THz} was only observed for low excitation powers. As shown in Figure 3.7d, at low pump powers, the generation efficiency of a smaller gap is greater than larger geometries, owing to the increased applied bias. However, for the same device E_{THz} is more readily saturated as the pump power increases, such that a device with a larger gap can ultimately produce more power.

Following the methodology described in §3.1, a 70 µm × 70 µm square photoconductive switch was fabricated from LT GaAs transferred onto a 500-µm-thick quartz substrate, over which a 30-µm-wide Ti/Au centre conductor and pair of bias arms

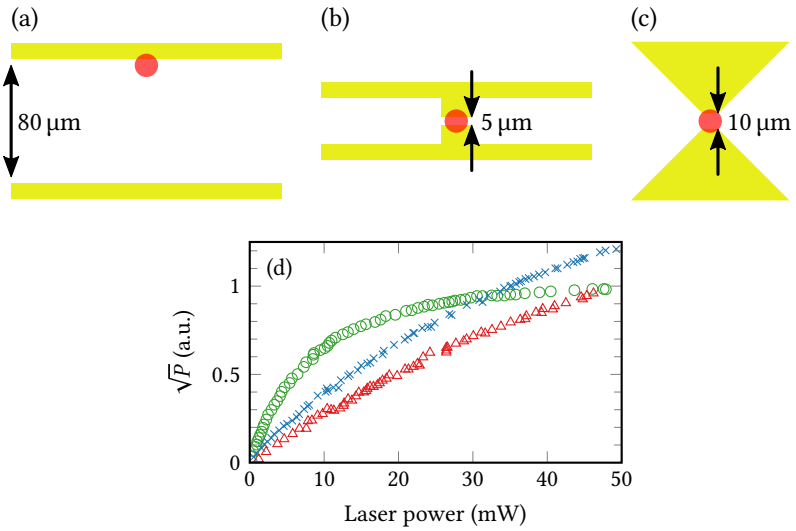

Figure 3.7: (a) A stripline antenna with an 80-µm-separation between the biased contacts. (b) A dipole antenna with a 20 µm × 5 µm photoconductive gap. (c) A bow-tie antenna with a 10 µm × 10 µm excitation region. (d) Square root of the power measured for a stripline (△), dipole (○), and bow-tie antenna (×). Reproduced from [96].

were formed. Fundamentally, the bias that can be applied to a switch is limited by the breakdown voltage of the surrounding materials. For example, the breakdown voltage of LT GaAs is of the order $2.5 \times 10^7\,\mathrm{V\,m^{-1}}$ when annealed between 500 °C and 650 °C [98], which equates to a bias of 125 V over the 5-µm-wide switching gaps tested here. Interestingly, although the breakdown field of air is of the order $3 \times 10^6\,\mathrm{V\,m^{-1}}$ on the macro-scale (an order of magnitude lower than LT GaAs), the breakdown field increases to approximately $4 \times 10^7\,\mathrm{V\,m^{-1}}$ when gap sizes are reduced to between 5 µm and 10 µm (which equates to a bias of 200 V to 400 V) owing to transitions in the breakdown mechanism [99, 100]. The laser power incident on PC 1 and PC 2 was fixed at 10 mW, while the bias applied to PC 1 was varied from −25 V to 25 V (considerably less than the theoretical maximum), as shown in Figure 3.8a. Across this relatively low bias range, the signal amplitude measured at PC 2 (which is proportional to E_{THz}) showed a linear relationship with the field applied at PC 1.

Although the maximum terahertz signal amplitude in Figure 3.8a could be improved further by increasing the applied bias (whilst still remaining below the breakdown threshold), such gains come at the expense of increasing electrical noise and thermally heating the device. Figure 3.8c shows Fourier transforms of the time-

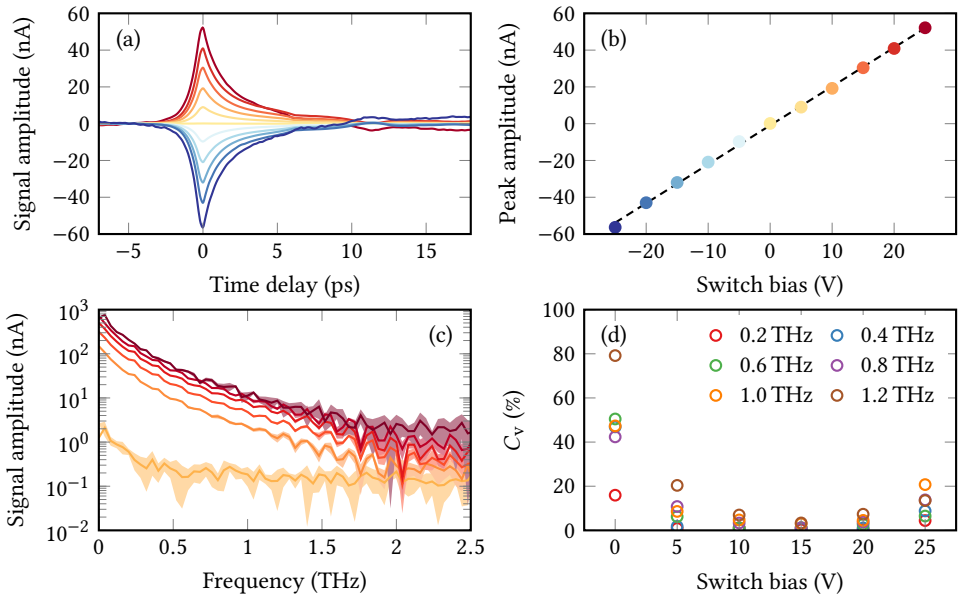

Figure 3.8: (a) The picosecond pulses measured at detection switch PC 2, as the bias applied to switch PC 1 was varied from −25 V (blue) to 25 V (red) in 5 V increments. (b) The amplitude of each peak in (a), and a linear fit (dashed) has been included to guide the eye. (c) Fourier transforms of picosecond pulses measured at PC 2 when the bias of PC 1 was varied from 0 V (orange) to 25 V (red) in 5 V increments. Lines shown are the mean of five measurements, and the shaded regions indicate the standard deviation. (d) The coefficient of variation, C_v at selected frequency points from (c) plotted as a function of switch bias.

domain data in Figure 3.8a. Although the relative signal amplitude across the 0 THz to 1.5 THz range can be seen to increase with applied bias, the noise floor has increased also. The noise floor is the background signal recorded when no spectral components are contributed by the picosecond pulse, so here it is equivalent to the spectrum measured beyond 2 THz. The frequency-domain traces in Figure 3.8c are the mean of five individually-recorded scans, for which the standard deviations are represented by the shaded regions. The ratio of the standard deviation to the mean, termed the coefficient of variation, C_v, can be used to assess the signal-to-noise ratio for such measurements, and is plotted in Figure 3.8d. As expected, at a bias of 0 V C_v is very large, as all measurements at this bias are of background noise. However, C_v also increases above 20 V, confirming that although a higher switch bias produces a greater pulse amplitude, the signal-to-noise ratio decreases. Thus, the minima between 10 V and 20 V represents the bias range in which an optimal signal-to-noise ratio was measured, and any further increases in applied bias up to the breakdown voltage would be detrimental for measurements. To maximise signal

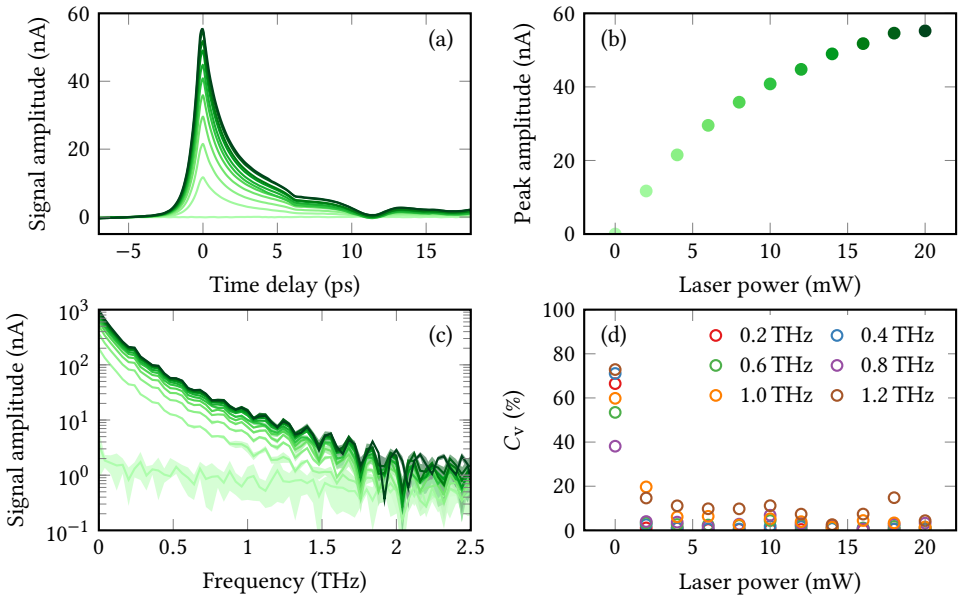

Figure 3.9: (a) Picosecond pulses detected at PC 2 as the laser power incident on PC 1 was varied from 0 mW (light-green) to 20 mW (dark-green). (b) The amplitude of the peaks from (a) plotted as a function of laser power. (c) Fourier transform of pulses measured at PC 2 when the laser power incident on PC 1 was varied from 0 mW (light-green) to 20 mW (dark-green). The shaded regions indicate the standard deviation of five measurements. (d) The coefficient of variation, C_v, as a function of laser power at selection frequencies.

amplitude, whilst maintaining a relatively low signal-to-noise ratio, a bias of 20 V was applied throughout the majority of this work.

As discussed, the terahertz pulse amplitude may also be increased by increasing the incident laser power which results in the generation of additional charge carriers. The effects of laser power were investigated at a fixed bias of 20 V applied to PC 1. The laser power incident on PC 2 was fixed at 10 mW and the power on PC 1 was varied incrementally from 0 mW to 20 mW. The time-domain traces in Figure 3.9a show an increase in pulse amplitude as the laser power was increased. However, as shown in Figure 3.9b, there is a nonlinear-relationship between the excitation laser power and the resulting pulse amplitude, which saturates at high pump powers. This is attributed to the screening effect of electron–hole separation [96], which reduces the localised electric field [12], as described by Equation 3.3.

The frequency-dependent responses shown in Figure 3.9c demonstrate an increase in amplitude up to 1.5 THz as the laser power is increased. Naturally, the plot of C_v in Figure 3.9d shows a large degree of variance when the laser was fully attenuated to 0 mW, but there is little change in C_v above 2 mW. Although increasing

the pump power above the approximately linear domain between 0 mW and 10 mW did not appear to decrease the signal-to-noise ratio, the increased laser power will increase the temperature local to the switch. The breakdown voltage of LT GaAs has been shown to decrease as temperature is increased, owing to an increase in the rate of thermionic emission [101]. Therefore, while the use of pump powers within the nonlinear regime shown in Figure 3.9b was not found to decrease the signal-to-noise ratio, it would decrease the breakdown voltage of the switch, increasing the likelihood of permanent damage.

3.2.2 Bias arm geometry

A switch array was produced by defining six 70 µm × 70 µm squares of LT GaAs, each separated by 1 mm, on a quartz substrate, over which five pairs of opposing straight-edged bias arms with widths between 5 µm and 70 µm were patterned, in addition to a pair of opposing 30-µm-wide arms that were tapered to a semicircular tip with a 5 µm diameter. Micrographs of each switch are shown in Figure 3.10a.

A 20 V bias was applied to one switch of each pair, and the picosecond pulses excited by a 10 mW pump laser were measured at the opposing switch. Owing to unavoidable variations in the fabrication process, and in the alignment of the pump and probe beams, the absolute signal amplitudes generated by photoconductive switches produced from the same LT GaAs wafer are expected to differ, and therefore the following switch comparisons were made by normalising the data with respect to the maximum of each picosecond pulse. As shown in Figure 3.10b, the tapered bias arm produced the picosecond pulse with the narrowest full-width at half-maximum (FWHM), and did not produce the negative-phase reflection present around 11 ps observed for all of the the straight-edged bias arms; the sources of these reflections are discussed in §3.3.1.

Fourier transforms of the pulses are shown in Figure 3.10c. The greatest frequency-dependent dynamic range was produced by the tapered switch geometry across the measurable range of 0 THz to ~1.5 THz, and the straight-edged switches showed little variation in frequency-response. Similarly, little variation was observed in the time-domain FWHM of the straight-edged switch geometries. Two factors con-

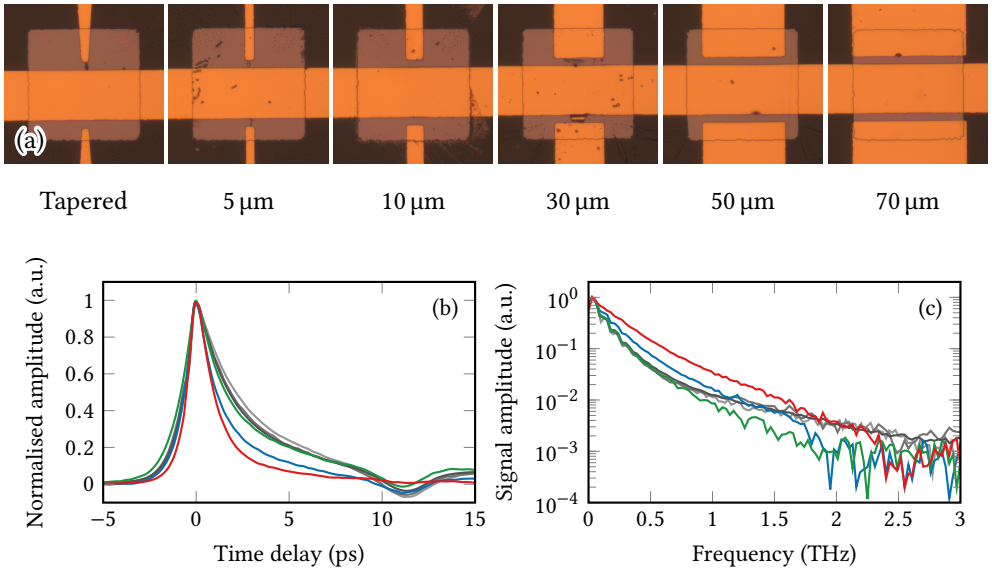

Figure 3.10: (a) Micrographs of a range of photoconductive switches comprising a 30 µm to 5 µm tapered bias arm, and five straight-edged bias arms that vary in width from 5 µm to 70 µm. In each case, there is a 5 µm separation between the tip of the bias arm and the 30-µm-wide centre-conductor. The 1-mm-long PGL that separated each switch is not shown. (b) Picosecond pulses generated and detected by photoconductive switch pairs with various bias arm geometries, normalised with respect to the signal peaks. The tapered (red) bias arm was found to generate the pulses with the shortest FWHM, and did not produce the reflections characteristic of the straight-edged switches. Also shown are picosecond pulses measured from the 5 µm (blue), 10 µm (green), and 30 µm to 70 µm (grey-scale, decreasing in intensity) switches. (c) Fourier transforms of the data in (b). The tapered switch geometry produced the greatest signal amplitude across the measured frequency-range.

tribute to the change in FWHM as a function of switch geometry; the distribution of the electric field along the centre-conductor, and the distribution of the laser power across the semiconductor.

The bias arms produce an electric field pattern that is distributed along the length of the PGL centre-conductor, and is related to the geometry of the biased arm tip. The DC electric field distribution in a switching region was modelled by subdividing the area into a potential grid of fixed voltage elements, each with a potential that is the average of its orthogonally neighbouring cells. That is, if a cell x is adjacent to cells a, b, c, and d, then the potential, V, at x is

$$V_x = \frac{V_a + V_b + V_c + V_d}{4}. \tag{3.6}$$

To determine the field distribution, a relaxation algorithm was initialised by applying an invariant bias to the probe arm, and its inverse to the centre conductor. The

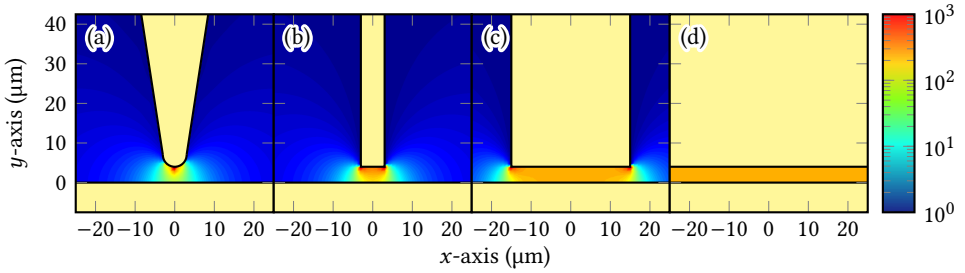

Figure 3.11: The electric field distribution established between biased probe arms of differing geometries, and the planar Goubau line centre-conductor. (a) A tapered probe arm with a 5 µm diameter, in addition to (b) 5-µm-wide, (c) 30-µm-wide, and (d) 70-µm-wide straight-edged geometries. The absolute field values are arbitrary, and colour was applied using the same logarithmic scale for all plots.

potentials of the elements between these components were then determined by iteratively calculating the average of all neighbouring cells until the absolute difference between the elements of two subsequent iterations was less than 0.5 %. Using this method, the magnitude of the electric field distribution was calculated for the tapered bias arm, and the 5 µm, 30 µm, and 70-µm-wide straight-edged geometries, as shown in Figure 3.11. For the straight-edged switch geometries, the modelled field was greatest at the corners of the metallisation, and was uniform in the parallel switch regions, away from the edges. For the tapered geometry, the electric field was greatest at the tip, closest to the centre-conductor, and decreased rapidly in intensity with distance from that point. In the wider switch geometries, excited charge carriers are simultaneously accelerated from positions along a greater length of the centre-conductor, resulting in a broader pulse in the time-domain, and an increase in the pulse FWHM. However, particularly for the larger switch geometries, it is unlikely that the entire switch is fully illuminated, or that the illumination intensity is uniform, as is the electric field.

In order to assess the laser power distribution across the beam focus, a scalpel blade was attached to a translation stage that allowed the blade edge to be moved into the beam path. Figure 3.12a shows the power measured by a laser power meter as the scalpel blade was translated into the path of a beam focused through a lens with a 10 mm focal length, the derivative of which is proportional to the power distribution across the diameter of the focus, as shown in Figure 3.12b. In agreement with the laser manufacturer, the profile in Figure 3.12b follows a Gaussian distribution, meaning

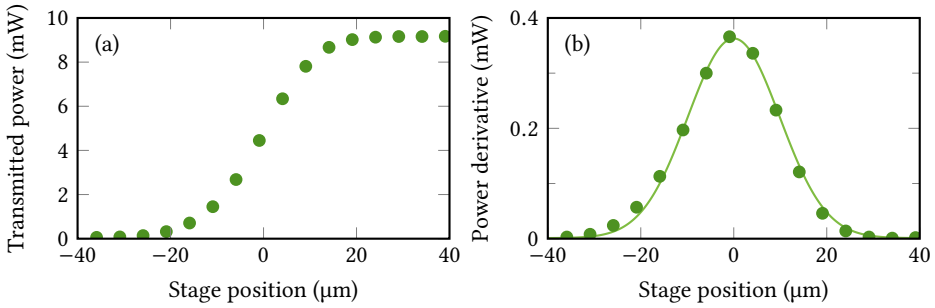

Figure 3.12: (a) The transmitted beam power measured as a scalpel blade was translated across the beam path. (b) The derivative of the data in (a) (scatter), and a Gaussian fit of the same data (solid line). The FWHM of the fit was measured to be 24 μm, meaning that half of the total power was focused within an area of that diameter.

that half of the total beam power is contained within the 24 μm FWHM, and the intensity quickly tends towards zero outside of this region. Therefore, while the electric field is evenly distributed across the width of the photoconductive switch, the amplitude of the laser excitation at a point (x, y) follows the two-dimensional Gaussian distribution [102],

$$A = \frac{1}{\sqrt{2\pi\sigma^2}} e^{\left(-\frac{(x-x_c)^2+(y-y_c)^2}{2\sigma^2}\right)}, \tag{3.7}$$

where x_c and y_c define the centre of the focus, and σ is the standard deviation of the Gaussian distribution, which is related to the full-width at half-maximum by

$$\text{FWHM} = 2\sqrt{2\ln 2}\sigma. \tag{3.8}$$

The normalised laser power distribution was calculated for a pump beam with a 24 μm FWHM focused at the centre of the switch gap, and multiplied by the electric field distributions in Figure 3.11. The resulting distributions, shown in Figure 3.13, are proportional to the terahertz electric field, E_{THz}, generated in the LT GaAs as a function of position. Here, it is clear that while the wider probe arms (>30 μm) produced an electric field capable of accelerating charges along a greater length of the centre-conductor, the laser-limited generation of charge carriers results in a similar E_{THz} pattern.

Of the switch geometries tested, the tapered bias arm produced the frequency-

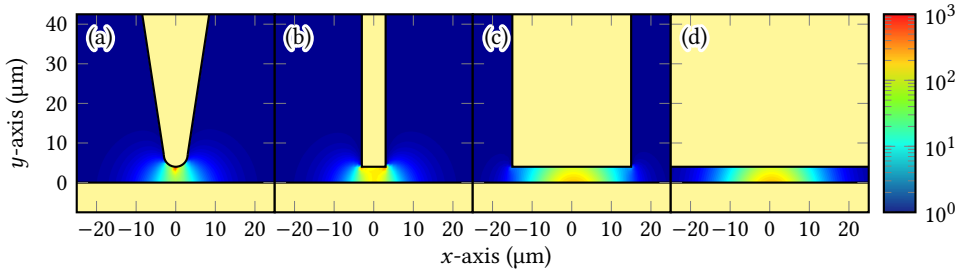

Figure 3.13: Simulations of spatially-dependent, generated terahertz field intensity, calculated by convolution of the applied electric field distribution and exciting laser spot size for different switch geometries including (a) a 5 µm taper, in addition to (b) 5-µm-wide, (c) 30-µm-wide, and (d) 70-µm-wide straight-edged geometries. The absolute values of E_{THz} are arbitrary, and colour was applied using the same logarithmic scale for all plots.

response with the greatest amplitude, and least significant oscillations, which are highly desirable properties for spectroscopic applications. As will be discussed in §3.3.1, oscillations in the time-domain are a result of impedance changes along the length of a waveguide, such as those created by the 90° corners of the straight-edged switches.

3.2.3 Through-substrate illumination

The experimental results presented thus far have involved the illumination of photoconductive switches from the metallised side of the device. In this configuration, the focus of the laser is partially masked by the metallisation, restricting illumination of the LT GaAs, as illustrated in Figure 3.14a. The reverse-side of the device measured in §3.2.1 was polished on a lapping station, to allow a pump beam to be focused through the quartz onto the rear surface of the LT GaAs switches, increasing the area of semiconductor in which charge carriers are generated, as shown in Figure 3.14b.

Some loss in the power of the pump beam would be expected from the introduction of the quartz substrate into the beam path, caused by absorption of the laser by the quartz, and by Fresnel reflectance losses, R, which describe the fraction of an incident beam that is reflected from an interface at which light passes between media with refractive indices n_p and n_q respectively,

$$R = \left| \frac{n_p - n_q}{n_p + n_q} \right|^2 . \tag{3.9}$$

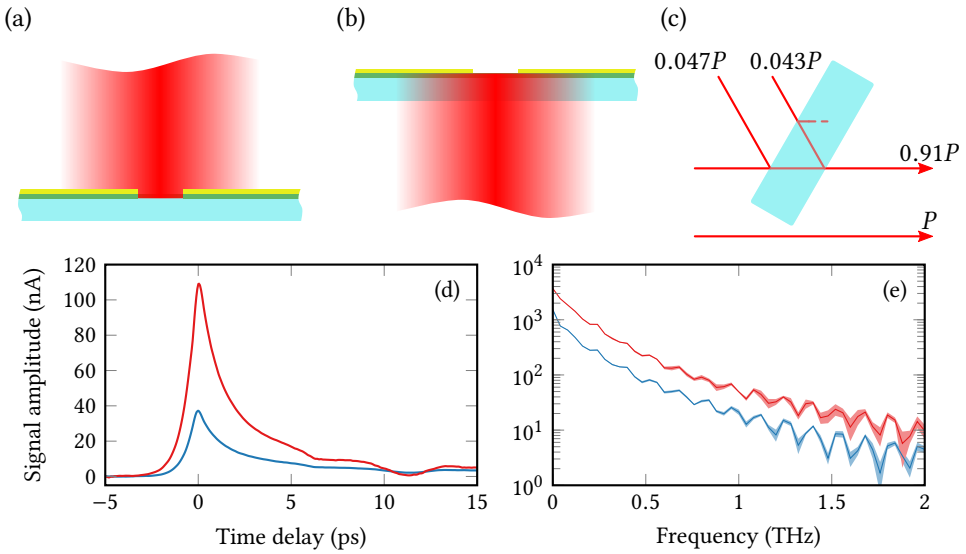

Figure 3.14: (a) Illumination of switches from the metallised surface results in masking of the beam. (b) Through-substrate excitation allows the entire beam to excite carriers in the LT GaAs. (c) The Fresnel reflectance losses at quartz–air interfaces. The quartz wafer is shown at an angle for clarity. (d) Picosecond pulses recorded when a photoconductive switch was illuminated through the metallisation (blue), and through the substrate material (red). Data shown are the mean of five measurements. (e) The Fourier transform of the data in (d), shaded areas indicate the standard deviation of five measurements.

A reflectance of 4.7 % was calculated for the interface between air ($n_p = 1$) and quartz ($n_q = 1.55$ at 800 nm [103]), and therefore a transmittance, $T = 1 - R = 91$ %, would be expected for a beam traversing two quartz–air interfaces, as illustrated in Figure 3.14c.

The actual losses were then assessed empirically by placing a 5-mm-thick quartz sample into the path of a 10 mW beam, and measuring the transmitted power. A transmission ratio of 89 % was calculated, corresponding to a measured transmitted power of 8.9 mW. The 2 % difference in loss between the theoretical and measured transmission values can therefore be attributed to absorption of the laser in the quartz substrate, suggesting an attenuation coefficient of 40 µW mm^{-1}. Hence, while the thinner 500-µm-thick quartz substrate would attenuate the 10 mW pump laser by only 20 µW through absorption, the reflection losses are independent of thickness, and comprise a loss of 0.9 mW.

The device measured in §3.2.1 was repositioned in the measurement system so that the laser could be focused onto the photoconductive switches through the quartz substrate. A 20 V bias was applied to the generating switch, which was excited

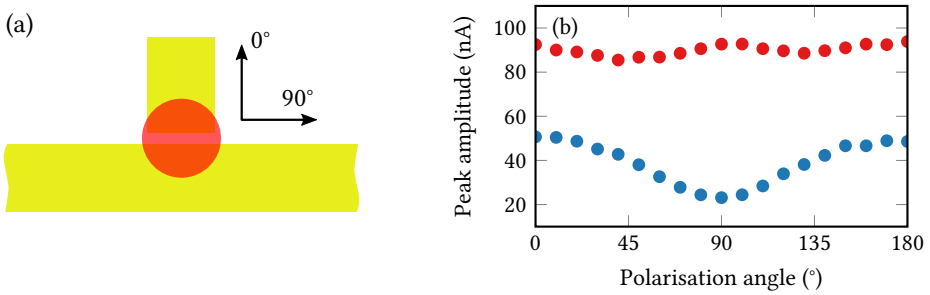

Figure 3.15: (a) A schematic of the 30-µm-wide photoconductive switch with a 5-µm-gap between the probe arm and centre conductor. In a typical experiment, the polarisation angle of the beam is perpendicular to the metal edges of the centre conductor (denoted by 0° here). (b) The peak amplitude of picosecond pulses plotted as a function of the polarisation angle of the pump beam when the switch is excited through the metallisation (blue), and through the substrate (red).

with a 10 mW pump beam. Pulses were detected with a 10 mW probe beam, and the measured pulses presented in Figure 3.14d and e show a significant increase in signal amplitude measured in both the time- and frequency-domain, without an increase in the standard deviation. Through-substrate illumination results in the excitation of additional charge carriers beneath the overlaid Ti/Au bias arms, a region that was masked when the device was illuminated through gaps in the metallisation. Therefore, the electric field that extended into the LT GaAs under the conductor contributed to the acceleration of these charge carriers, increasing the total terahertz electric field generated by the switch.

In addition to exciting charge carriers across a greater area, a beam focused through the higher-permittivity quartz substrate has a larger angle of convergence, which reduces the size of the beam focus and consequently increases the power density incident on the switching region. Hence, more charge carriers were excited between the metal contacts, where the electric field magnitude was greatest, further increasing the terahertz electric field generated.

3.2.4 Through-substrate illumination and polarisation

A device mounted in the on-chip measurement system is typically positioned such that the metal edges that define the switch are perpendicular to the polarisation of the laser source, as shown in Figure 3.15a. When a half-wave plate was used to rotate the polarisation angle of the pump laser from perpendicular (0°), to parallel

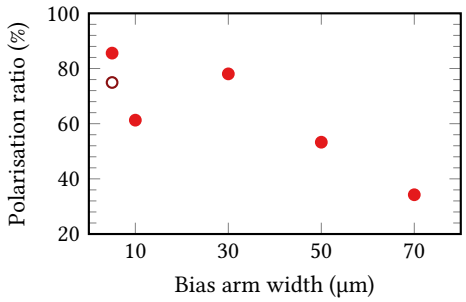

Figure 3.16: The ratio of the peak signal amplitudes measured when the pump beam polarisation angle was varied between 0° and 90° for the straight-edge bias arms (●), and the tapered switch (○). The wider bias arms were found to be more sensitive to the polarisation angle of the pump beam.

(90°) with respect to the metal edge of the centre-conductor, it was noted that the amplitude of the resulting picosecond pulses varied significantly. This phenomenon was investigated by rotating the polarisation angle of the pump laser from 0° to 180° in increments of 10° when the device was excited both through the metallisation, and through the substrate. As shown in Figure 3.15b, the polarisation-dependence of the terahertz peak amplitude was found to be more significant when the switch was excited through gaps in the metallisation than when illuminated through the substrate. This may be owing to the narrow separation of the probe arm and centre conductor metal edges causing behaviour similar to that of a wire-grid polariser in which a plasmon mode is coupled into the parallel metal edges, reflecting the incident optical beam, as has been observed in periodic metal–semiconductor–metal terahertz emitters [104]. When illuminated through the substrate, the peak amplitude showed a reduced polarisation-dependence, but also at half the period of the metallised results, which is attributed to the birefringence of the quartz substrate.

The experiment was repeated for switches with arm bias widths between 5-µm-wide, and 70-µm-wide. The ratio of the peak signal amplitudes measured for polarisation angles of 90° and 0° was calculated for each switch, such that a polarisation ratio of 100 % indicates no change in amplitude, and 0 % represents complete extinction at an angle of 90°. The results presented in Figure 3.16, show that the wider bias arms generally demonstrated a greater dependence on polarisation angle, suggesting that the increased interaction length of the parallel metal edges increases the plasmon coupling effect. The pulses generated from the tapered geometry showed a relatively

weak polarisation-dependence, yet for all measurements, a polarisation angle of 0° was maintained to maximise the generated pulse amplitude.

3.3 Designing planar Goubau line geometries for spectroscopy

In addition to the efficient generation of terahertz-frequency electric fields, an effective on-chip spectrometer is one designed such that there is a sensitive interaction between the propagating field and analyte. This includes consideration of the informative frequency resolution that can be attained, and the frequency-dependent distribution of the electric field and its various propagation modes.

3.3.1 Sources of reflections in the time-domain

The switch array geometries considered in §3.2 comprise multiple switches along the length of a transmission line that cause changes in the characteristic impedance owing to the high permittivity of the LT GaAs material, and the proximity of the bias arms to the centre-conductor. From microwave theory, it is known that a wave transitioning from a region of impedance Z_1 to an impedance Z_2 is reflected by a ratio determined by the reflection coefficient, Γ [105],

$$\Gamma = \frac{Z_2 - Z_1}{Z_2 + Z_1}. \tag{3.10}$$

In waveguide geometries for which the characteristic impedance can be calculated, Γ can be assessed directly. However, as discussed, analytical solutions have not been identified for the planar Goubau line. Yet, given the simplicity of Equation 3.10, the relative magnitudes of Z_1 and Z_2 can be approximated to determine whether Γ is positive or negative for a given interface, i.e. $\Gamma > 0$ if $Z_1 < Z_2$, and $\Gamma < 0$ if $Z_1 > Z_2$.

In spectroscopic applications, it is often necessary to produce measurements with a high frequency-resolution. This is particularly important in terahertz-frequency measurements of crystalline materials for which absorption features that are tens of gigahertz wide are expected [106]. The frequency-resolution of a given measure-

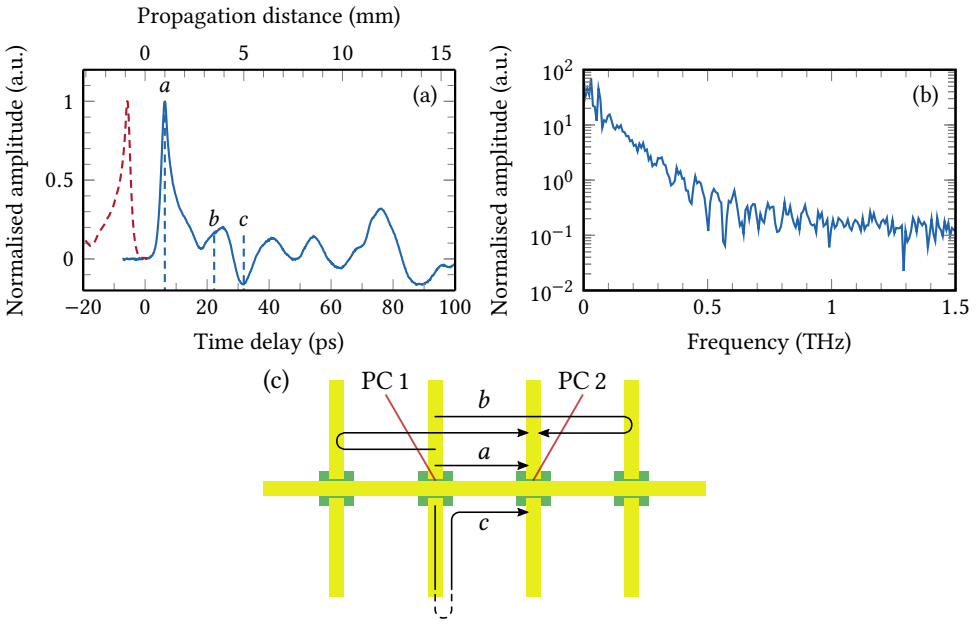

Figure 3.17: (a) The time-domain response measured when a picosecond pulse was excited at PC 1, and the resulting pulse train was detected at PC 2 (blue, solid). Multiple reflections are observed in the time after the arrival of the initial pulse. Also shown is a pulse that was excited at PC 2 and detected at PC 1 (red, dashed), which is used to calculate the group propagation velocity. (b) The Fourier transform of the data in (a), the many time-domain reflections are seen to create oscillations in the frequency-domain. (c) A schematic of the switch array device, indicating the source of the reflections labelled *a*, *b*, and *c* as a pulse propagates from PC 1 to PC 2.

ment is the inverse of the length of the recorded time window, i.e. a 100 ps time window equates to a resolution of 10 GHz in the frequency domain, and therefore an increase in the measurement time window duration results in an increase in the frequency-resolution. Conventionally, an increase in frequency-resolution refers to the increased density of data points in the frequency domain, such that a measurement at a frequency-resolution of 5 GHz comprises twice as many data points as a measurement with a 10 GHz resolution. As will be shown here, the measurement window of a device geometry that has not been designed specifically for high frequency-resolution measurements cannot be extended indefinitely without incorporating a number of problematic time-domain features into the measured response.

The time-domain response shown in Figure 3.17a was measured by exciting a picosecond pulse at switch PC 1, and then detecting the arrival of pulses at an adjacent switch, PC 2, separated by a distance of 1 mm. The transient electric field excited at a photoconductive switch extends both into and out of the substrate in all directions,

and therefore is coupled into all proximal media. The many impedance changes along these propagation paths cause the pulses to be reflected, which results in a number of parasitic oscillations in the time-domain, as shown in Figure 3.17a. The inclusion of these oscillations in the Fourier transform window, as demonstrated in Figure 3.17b, also results in many oscillations in the frequency-domain that complicate further analysis, and potentially mask spectral features produced by the measured samples. The first three distinct features in the recorded time-domain trace have been labelled *a*, *b*, and *c*, and the periodicity of the switch array geometry means that the subsequent unlabelled features in the time-domain arise from equivalent sources. The first detected pulse, *a*, is a result of the electric field that is coupled into the centre-conductor and propagates along the shortest path from PC 1 to PC 2, which is the 1-mm-long transmission line that separates the switches. To determine the source of other reflections, the group propagation velocity was determined so that a conversion between temporal and physical length could be performed.

Group propagation velocity can be measured by reversing the excitation direction, such that a pulse is generated at PC 2 and detected at PC 1, without physically altering the optical arrangement (i.e. the pump pulse becomes the probe pulse, and *vice versa*). As shown in Figure 3.17a, there was a 12.73 ps difference between the peak positions when exciting in either direction, over an effective propagation distance of 2 mm, which equates to a group propagation velocity of $1.57 \times 10^8\,\mathrm{m\,s^{-1}}$.

With this information, the time delay axis in Figure 3.17a can be mapped directly to propagation distance, and then used to determine the sources of the features *b* and *c*, as indicated in Figure 3.17c. The feature at *b* is broadened since it is a superposition of pulses that have been reflected by adjacent switches, along with the fraction of the initial pulse that was reflected between PC 2 and PC 1 after a total propagation distance of 3 mm. The feature at *c* corresponds to a propagation distance of 5 mm, and has a negative-phase indicating that it is a result of the electric field coupled into the 2-mm-long unused bias arms; a reflection is produced at the lower-impedance ground connection (a total distance of 4 mm) and is then detected after coupling along the 1-mm-long transmission line. A device that is suitable for high frequency-resolution measurements must therefore be designed to minimise the number of

reflection interfaces, in order to increase the duration of the reflection-free time-window for Fourier transformation.

3.3.2 Prevention of reflections for high frequency-resolution devices

As has been demonstrated, a device with many photoconductive switches defined along the length of a planar Goubau line produces undesirable time-domain reflections. This effect can be reduced by fabricating a single pair of photoconductive switches, and by increasing the length of the bias arms and centre-conductor to 10's of millimetres before external connections are made, so that reflections are delayed by 100's of picoseconds after the initial pulse [54, 94]. Simply extending the conductors in a straight line to achieve the desired length would result in an inefficient use of the quartz substrate material, and therefore meanders were introduced into the conductor paths.

Propagating waves are partially reflected by the change in characteristic impedance introduced by a change in waveguide direction, as a function of bend-radius, with a right-angled bend introducing the greatest propagation perturbation [107]. To minimise the energy reflected by any transmission line feature, the magnitude of the return loss parameters (S_{11} and S_{22}) should be as large as possible. Figure 3.18a shows the simulated scattering parameters for a 2-mm-long planar Goubau line that incorporates a 90° bend for which the radius was varied between 0.05 mm and 1 mm. Between 0.05 THz and 1 THz, the four radii demonstrated comparable insertion loss (S_{21}) characteristics, but the return losses (S_{11}) of the sharper 0.05 mm and 0.1 mm bend radii were approximately a decade lower across the majority of the simulated frequency range. Plan views of the two-dimensional field distribution of the four simulated bend radii are presented in Figures 3.18c to f. The field originated at the position $(0, 0)$ for the 0.05 mm bend, and the x-value of the origin increases with radius in order to maintain the total transmission line length. In Figures 3.18c and d, the reflectivity of the sharper bend radii resulted in a notable inequality in the field strength before and after the corner, and partial dissipation of the field into the substrate beyond the corner. As illustrated in Figure 3.18b, the guided mode wavefront is perpendicular to the direction of propagation [108]. In order to maintain

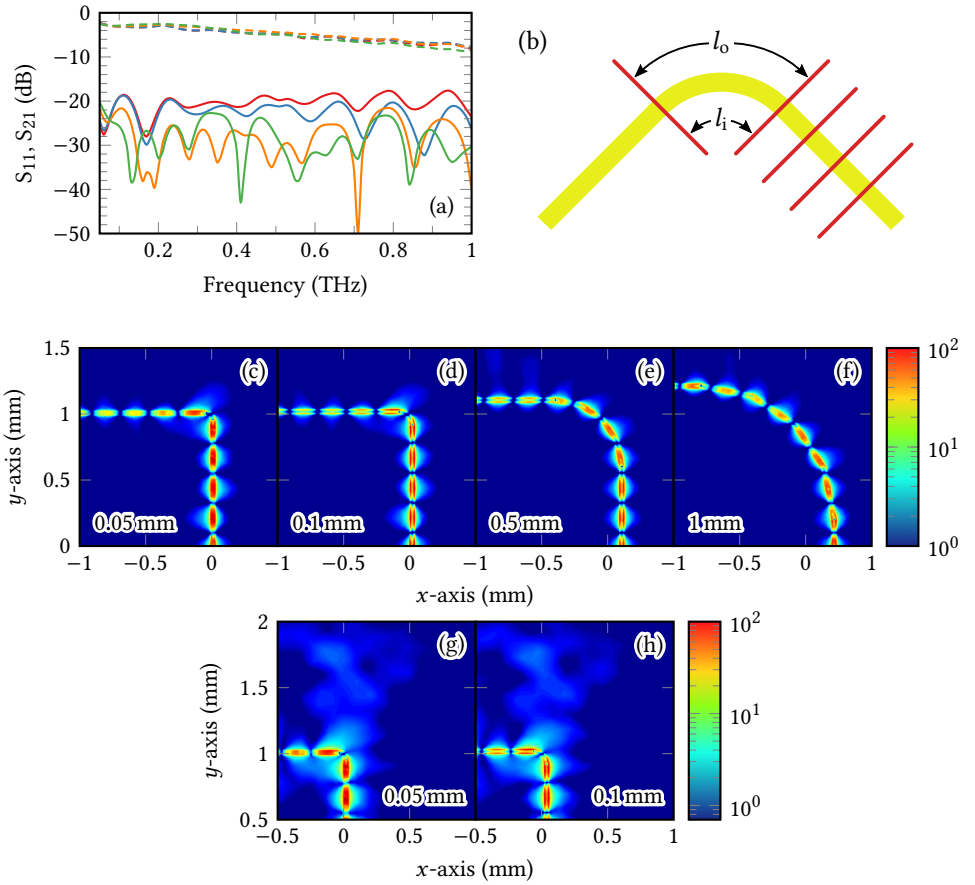

Figure 3.18: (a) The S_{21} insertion (dashed) and S_{11} return (solid) losses of four 2-mm-long, 30-µm-wide planar Goubau lines that include a 90° bend with 0.05 mm (red), 0.1 mm (blue), 0.5 mm (orange), and 1 mm (green) radii. (b) The perpendicular wavefront of the Goubau mode results in differing outer and inner path lengths, l_o and l_i respectively, across the bend section. (c)–(f) Plan views of the distribution of a 400 GHz electric field propagating along the simulated Goubau lines. Fields were excited from the x-axis. The absolute field values are arbitrary, and colour was applied using the same logarithmic scale for all plots. (g) and (h) Plan views of the unguided mode that extends from the sharper corners in (c) and (d). Colours have been rescaled to more clearly show the radiating field.

the wavefront integrity, the velocity of the signal must therefore differ along the longer outer and shorter inner path lengths, l_o and l_i, on the outside and inside of the bend respectively. As the bend radius is reduced, the difference between l_o and l_i is increased; therefore, the velocity of the outer wavefront fringe tends towards c, and the guided wave transitions to an unguided free-space–substrate mode, as can be observed in Figure 3.18g and h in which a portion the field radiates from the sharp corner transitions along the original direction of propagation [108].

To minimise reflections, whilst maintaining a compact device perimeter, the geometry illustrated in Figure 3.19c was developed by the Leeds research group [88],

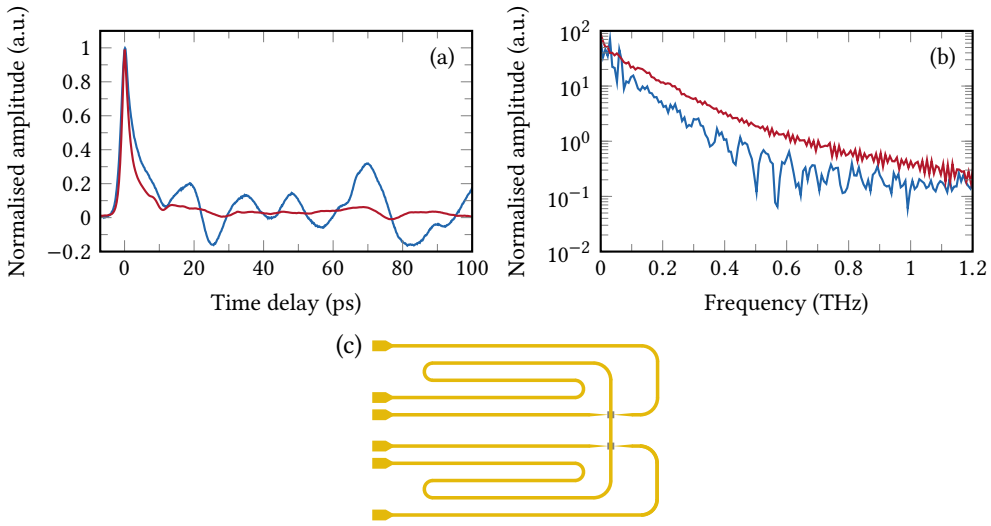

Figure 3.19: (a) Time-domain traces recorded from the geometry shown in Figure 3.17 (blue), and the low-reflection geometry in (c). (b) Fourier transforms of the data in (a). By removing many of the reflection sources from the switch array geometry, the low-reflection design produces fewer oscillations in the frequency-domain. (c) Schematic of a planar Goubau line geometry designed to minimise time-domain reflections by extending the length of all conductors to temporally delay reflections from external connections; corners with a 1 mm bend radius are used to limit the pattern perimeter without introducing additional reflections.

in which two photoconductive switches are separated by 1 mm, and the centre-conductor extends for 30 mm to the bonding pads used to make external connections. The 10 mm × 10 mm perimeter of the design was maintained by introducing corners with a 1 mm bend-radius into the centre conductor and tapered bias arms, that were also extended to approximately 10 mm. A device of this design was fabricated on a 100-µm-thick quartz substrate, and many of the reflections exhibited by the switch array demonstrated in §3.3.1 were significantly delayed, as illustrated in Figure 3.19a. By temporally delaying the arrival of reflections, the time-domain window over which the Fourier transform is computed contains fewer of these interfering etalons, which substantially reduces oscillations in the frequency-domain. For comparison here, the Fourier transforms shown in Figure 3.19b were calculated using the same 100 ps window, resulting in a frequency resolution of approximately 10 GHz. However, the first significant reflection in the low-reflection geometry did not occur until approximately 200 ps after the initial impulse, and therefore a longer window could be used to further increase the measurable frequency resolution.

3.3.3 Generation of additional propagation modes

The omnidirectional electromagnetic field generated at a photoconductive switch extends into and out of the substrate and can result in multiple modes of propagation. Through the introduction of overlaid conductors, the planar Goubau line device preferentially supports the propagation of a radial Goubau mode, however this is not always the case. The distribution of the electric field propagating along the Goubau line is dependent on the permittivity of the surrounding media [58, 86], and the use of thick or high permittivity substrates can result in the generation of additional propagation modes operating at high frequency [109].

In addition to the desired Goubau mode, the plane–parallel surfaces of the supporting substrate perform similarly to a dielectric slab waveguide when the effective wavelength, λ_{eff}, of the slab mode is less than twice the dielectric thickness, h, such that the slab mode cut-off thickness is $2h_{\text{c}} = \lambda_{\text{eff}}$. The effective wavelength in a stratified air–substrate–air structure is approximately [109],

$$\lambda_{\text{eff}} \approx \frac{2\lambda}{\sqrt{\varepsilon_{\text{sub}} + 1}}, \tag{3.11}$$

where ε_{sub} is the substrate permittivity, and λ is the free-space wavelength. Therefore, Equation 3.11 can be rearranged to find h_{c} as a function of frequency,

$$h_{\text{c}} \approx \frac{c}{f\sqrt{\varepsilon_{\text{sub}} + 1}}. \tag{3.12}$$

Figure 3.20a shows the cut-off thickness for a quartz substrate ($\varepsilon_{\text{sub}} \sim 3.78$) between 0.05 THz and 1 THz. Using this model, the cut-off frequency of the TE_0-like dielectric slab mode can be determined for a given substrate thickness. For example, if the Goubau mode is to be supported up to 1 THz, then a quartz substrate less than 140-µm-thick is required to avoid the generation of substrate modes. To further illustrate this effect, a 30-µm-wide, 150-nm-thick planar Goubau line patterned on a quartz substrate was modelled in HFSS. Figure 3.20b shows the real part of the effective permittivity of the Goubau mode, and the TE_0-like mode supported by the substrate without an overlaid conductor when the quartz thickness was varied from

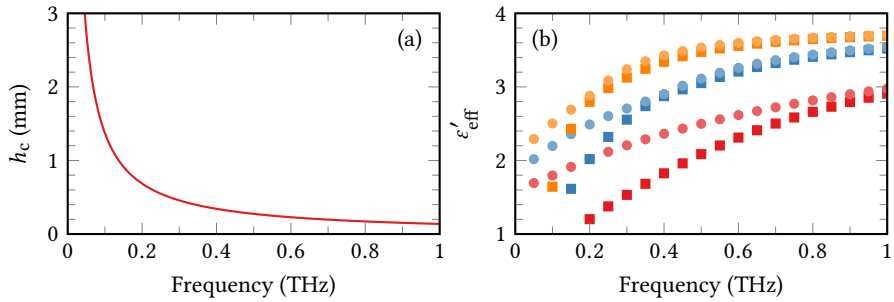

Figure 3.20: (a) The frequency-dependence of h_c as determined by Equation 3.12 for a quartz substrate ($\varepsilon_{sub} \sim 3.78$). (b) Real part of the effective permittivity of the Goubau (●) and TE_0-like (■) substrate modes simulated in HFSS for 500 µm (blue), 250 µm (red), and 100-µm-thick (green) substrates. The two modes have the same effective permittivity above the cut-off frequency of the given substrate thickness.

100 µm to 500 µm. The permittivity of the two modes coincide above the cut-off frequencies defined in Figure 3.20a, suggesting that the Goubau mode transitions to the preferentially supported substrate mode as the frequency is increased beyond this critical point.

Figure 3.21a shows a cross-section of a 100 GHz electric field supported by a planar Goubau line patterned on a 250-µm-thick quartz substrate, as simulated in HFSS. The field is concentrated around the PGL at position $(0, 0)$, and extends into and out of the substrate. However, as shown in Figure 3.21b, at 500 GHz, the slab propagation mode is preferred, and the electric field is almost completely confined to within the substrate. Given that spectroscopy relies on measurement of the interaction between electric field and sample, the evolution of these additional substrate modes is highly undesirable. Whilst the field distribution illustrated in Figure 3.21a would be sensitive to the presence of analytes positioned above and below the substrate, the field distribution shown in Figure 3.21b would demonstrate a very weak interaction with a sample positioned anywhere other than within the substrate.

Figure 3.21c and d show the corresponding field distributions when the quartz substrate was reduced to 100-µm-thick. Owing to the reduced dielectric load beneath the conductor, the relative symmetry of the substrate and superstrate regions is increased, and the electric field distribution is more circular at 100 GHz. As shown in Figure 3.21d, the Goubau mode is maintained across a greater frequency-range, owing to the increased slab-mode cut-off frequency that is a result of the thinner

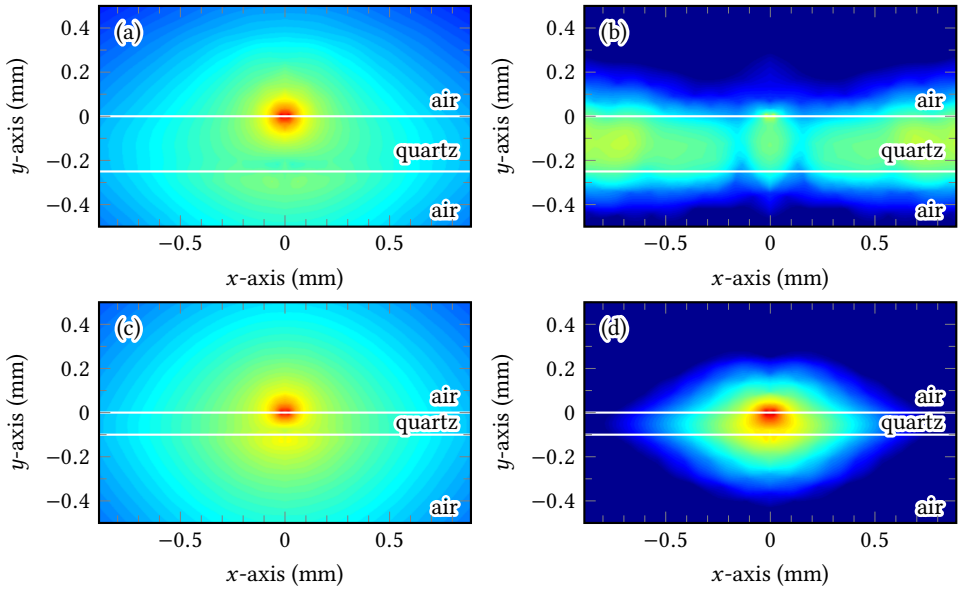

Figure 3.21: (a) A cross-section of the 100 GHz electric field around a planar Goubau line (positioned at $(0, 0)$) patterned on a 250-µm-thick quartz substrate. (b) A cross-section of the 500 GHz electric field around the same geometry as in (a). Rather than supporting a Goubau mode, the field is confined to a dielectric slab substrate mode. (c) A cross-section of the 100 GHz electric field around a planar Goubau line patterned on a 100-µm-thick quartz substrate. (d) A cross-section of the 500 GHz electric field around the same geometry as in (c). The thinner substrate maintains the circular Goubau mode across a greater frequency-range. In each figure, the absolute values of electric field are arbitrary, but the same colour scale has been applied.

substrate material.

The generation of these additional substrate modes therefore implies a fundamental limit to the spectroscopically-useful bandwidth of the planar Goubau line, that is dependent on the thickness of the substrate on which it is fabricated. Previously, Russell measured the frequency response of a 1-mm-long PGL patterned on a quartz substrate that was progressively mechanically lapped from 250 µm to 85-µm-thick [88]. Transmitted picosecond pulses were measured for each substrate thickness, and the Fourier transforms were calculated as shown in Figure 3.22. Through application of Equation 3.12, the cut-off frequency at which the evolution of the dielectric slab mode is predicted for each substrate thickness was calculated, as indicated by the dashed lines in Figure 3.22. For each substrate thickness, oscillations are observed in the spectrum above the highlighted cut-off frequency as the mode of propagation transitioned from the radial Goubau to the dielectric slab mode.

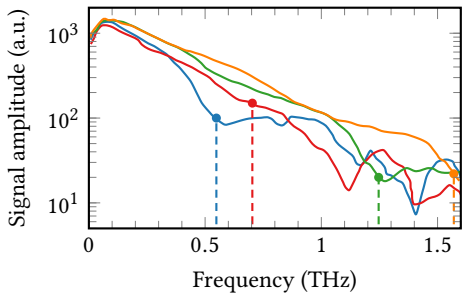

Figure 3.22: Fourier transforms of picosecond pulses after propagation along a 1-mm-long planar Goubau line patterned on 250 µm (blue), 195 µm (red), 110 µm (green), and 85-µm-thick (orange) quartz substrates. The dashed lines indicate the substrate mode cut-off frequencies as expected from Equation 3.12. Above these points, the oscillations in the spectra are caused by a transition from the Goubau to dielectric slab modes.

3.4 Concluding remarks

The picosecond pulse generation characteristics of integrated LT GaAs photoconductive switches fabricated on quartz substrates have been investigated. It has been shown that maximising signal amplitude may reduce the signal-to-noise ratio across the measured frequency range, and methods for quantifying this effect have been introduced. Geometry considerations for the generation of terahertz field have been explored, and the results of through-substrate illumination, varying laser polarisation, and decreasing substrate thickness have been presented.

While the advantages of optimising the signal-to-noise ratio across the measured frequency range are clear, the understanding of propagation modes is critical for spectroscopic applications. In Chapter 4, it will be shown that maintenance of the Goubau mode does not only allow for sensitive interaction between the propagating electric field and the sample, but also enables the propagation mode for unknown samples to be approximated. This knowledge will then allow extraction of the frequency-dependent propagation characteristics of liquid samples, information that is yet to be successfully determined from on-chip planar Goubau line measurements.

Chapter 4

The Development on an On-chip Spectrometer

Methods for the generation, detection, and efficient propagation of terahertz-frequency electric fields, supported by the planar Goubau line, have been discussed in previous chapters. In this work, an on-chip microfluidic spectrometer is proposed that comprises a planar Goubau waveguide integrated with a microfluidic chip. The design of this device is first investigated through the use of reflection-geometry transmission lines, which enable simultaneous measurement of picosecond pulses injected into and output from the waveguide structure, aiding understanding of several design aspects. The findings from these devices are then combined with the knowledge of mode-propagation characteristics explored in Chapter 3, and a design proposed that allows extraction of the complex permittivity of an unknown liquid sample; the veracity of the extracted parameters is verified by comparison with data previously published in the microwave and terahertz frequency ranges.

4.1 Design and fabrication of microfluidic channels

As discussed in §1.3, microfluidic systems are those in which the dimensions are sufficiently small that gravitational effects play a secondary role to surface tension and capillary forces. The transition from macro- to micro-scale flow systems is dictated primarily by the dimensions of the channel and the properties of the controlled liq-

uid. Owing to the restricted laminar dynamics in a microfluidic system, the process of modelling actions such as flow or mixing is simplified. The Reynolds number, *Re*, is a dimensionless quantity that relates the resistance of a fluidic system to the dynamics of the solutions flowed through it [110, 111],

$$Re = \frac{v_f D_h}{\upsilon_k}, \tag{4.1}$$

where v_f is the mean velocity, υ_k is the kinematic viscosity of the liquid in question, and D_h is the hydraulic diameter of the channel. The majority of the channels investigated in this work had a rectangular cross-section, and therefore an effective approximation of D_h was used [112],

$$D_h = \frac{4A}{p_w}, \tag{4.2}$$

where A is the cross-sectional area of the channel, and p_w is the wetted perimeter (the length of the channel perimeter that is in contact with the liquid). Therefore, *Re* can be used to determine a critical velocity above which the flow of a liquid in a given geometry will transition from a laminar to a turbulent regime. The specific *Re* that represents this transition region is not clearly defined, but values between 1800 and 2200 are typically reported [113–116]. The Reynolds number in microfluidic channels is normally sufficiently low that laminar flow is maintained at very high flow rates. For example, if DI-H_2O ($\upsilon_k \approx 1 \times 10^{-6}\,m^2\,s^{-1}$ [117]) was flowed through a 200 µm × 200 µm channel, *Re* would exceed 2000 when the flow rate was $10\,m\,s^{-1}$, which equates to a volumetric rate of $0.4\,mL\,s^{-1}$.

Given that a high Reynolds number indicates a turbulent environment, it was necessary to design the microfluidic circuit geometries such that it was possible to replace liquid samples without mixing, thereby avoiding contamination. This was achieved by restricting the channel dimensions such that an acceptably low Reynolds number could be attained with a controllable rate of liquid flow. The microfluidic systems investigated in this work were designed for integration with on-chip planar Goubau line devices so that a propagating electromagnetic field interacted with

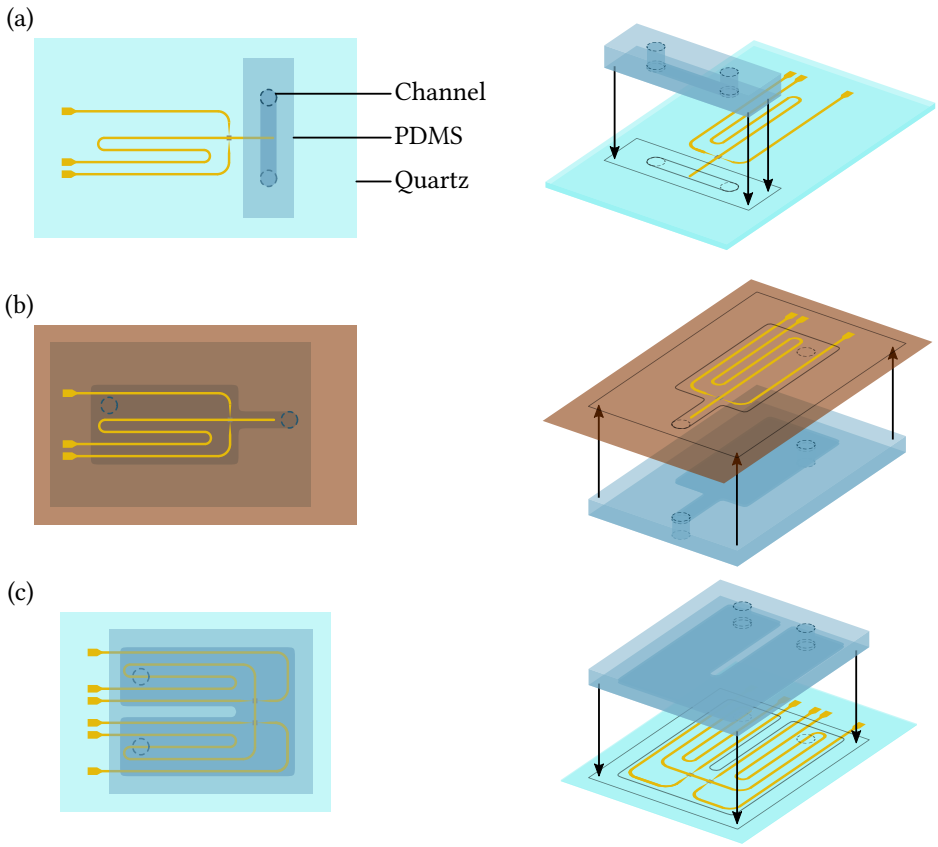

Figure 4.1: Schematic plan-views and three-dimensional illustrations of the key device geometries investigated. (a) A 2-mm-long reflection-geometry planar Goubau line patterned on a 500-µm-thick quartz substrate, with which a microfluidic channel has been integrated. The channel was 800-µm-wide, and bonded in such a way that there was a 600 µm interaction length between the transmission line and overlaid liquid. (b) The same transmission line geometry as in (a) patterned on a 50-µm-thick polyimide substrate, with a microfluidic channel bonded to the underside to remove all impedance-mismatched boundaries. (c) A 1-mm-long transmission-geometry Goubau line on a 100-µm-thick quartz, with a channel bonded to the top surface. The dashed circles in all figures represent the access ports where silicone tubing was inserted.

the overlaid liquid-under-test. Therefore, the channels had to be fabricated from a material that could be bonded to the device substrate so that a seal was created to prevent the release of any hazardous chemicals that may be measured, and to avoid the creation of an electrical short across the nearby biased photoconductive switches.

4.1.1 Device design iterations

The development of the terahertz-frequency on-chip spectrometer was progressed through three key iterations, as illustrated in Figure 4.1. The method of channel integration shown in Figure 4.1a was inspired by a combination of two published

designs in which an overlaid microfluidic channel [55] was positioned perpendicular to a reflective open circuit stub [91]. This design (measurement of which is discussed in §4.2.1) comprised a 2-mm-long reflection-geometry Goubau line patterned on a 500-µm-thick quartz substrate, to which a 400-µm-deep microfluidic channel defined in PDMS was bonded as illustrated. The alignment of the channel is restricted by the presence of the biased photoconductive switches that could be shorted by conductive analytes. It will be shown that the abrupt changes in the transmission line impedance created by the channel boundaries introduce undesirable reflections in the time-domain, which complicate analysis, but aid in describing the propagation characteristics of a sample-loaded Goubau line.

The device in Figure 4.1b is a variation upon the first design, and is discussed in §4.2.2. Here, the quartz substrate material was replaced with a 50-µm-thick polyimide film, which was sufficiently thin that the propagating electric field was sensitive to a sample placed on the underside of the substrate. This through-substrate geometry meant that the biased photoconductive switches were isolated from the liquid samples, so the 400-µm-deep channel could cover the entirety of the transmission line, without electrically shorting the switches.

Finally, the on-chip planar Goubau line spectrometer design in Figure 4.1c was investigated in which a low-reflection transmission line (as described in §3.3.2) was patterned on a 100-µm-thick quartz substrate, which was then coated with a thin, insulating dielectric. A 100-µm-deep channel was bonded to the top surface of the dielectric so that the switches were isolated from the liquid. It will be shown that the combination of the high frequency resolution that can be achieved with the low-reflection geometry, and the simplified three-dimensional structure created by the method of microfluidic integration enables the extraction of the complex permittivity of an unknown sample in the liquid channel.

4.1.2 Fabrication of microfluidic channels

As discussed in §1.3, PDMS is a silicon-based polymer that is commonly used in the research of bio-compatible microfluidic devices as it exhibits many properties that are desirable for rapid prototyping. Here, features were defined in PDMS by casting

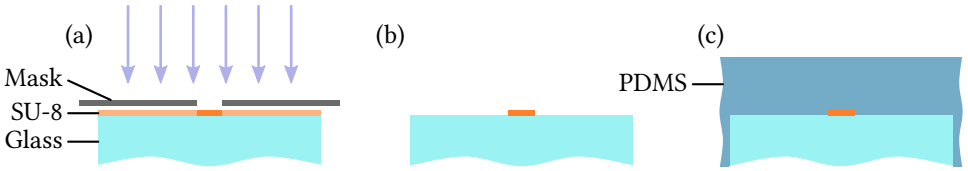

Figure 4.2: (a) A film of SU-8 was spun onto a glass microscope slide, and then exposed to ultraviolet light through a lithographic mask. (b) The unwanted resist was removed in ethyl lactate solvent, so that only the microfluidic channel mould remained. (c) PDMS was cast over the mould and then cured to define a permanent channel in the elastomer.

over reusable SU-8 mould-masters patterned on glass. SU-8 is a negative photoresist that can be used to create permanent high-aspect-ratio structures between 1 µm and 1200-µm-thick [118, 119]. Depending on the target channel depth, SU-8 mould masters were creating using one of two methods.

Thinner (<100-µm-thick) moulds were fabricated by first oxidising a glass microscope slide in a H_2SO_4:H_2O_2 piranha etch solution (7:3 by volume), which removed any organic residue, and increased the hydrophilicity of the glass surface. The cleaned slide was then washed in DI-H_2O, after which it was dried with N_2, and baked at 200 °C for ten minutes to desorb any remaining water. SU-8 (Microchem) is supplied in a range of formulations, the selection of which is based upon the desired thickness of the finished product. The process described here provides timings for the fabrication of a 20-µm-thick mould; the process parameters for SU-8 films of differing thickness can be found in the manufacturer's data sheet [120]. The glass slide was spin-coated with SU-8 2025 at 500 rpm for 10 seconds to evenly distribute the resist, and then at 4000 rpm for 30 seconds to produce a 20-µm-thick layer, as shown in Figure 4.2a. The SU-8 diluting solvent was evaporated by a soft-bake at 65 °C for five minutes, and then at 95 °C for ten minutes. When processing SU-8, thermal stresses can be introduced owing to the differing thermal expansion coefficients of the resist and the glass substrate, which can cause the formation of cracks in the brittle SU-8. Therefore, all baking processes were initiated on a room-temperature hot plate that was then set to the target temperature, resulting in a gradual increase that limited the induced stress. The resist was exposed to ultraviolet light (20 mW cm^{-2}) for eight seconds through a dark field mask, which initiated a cross-linking reaction in the irradiated regions. After exposure, the resist was baked at 65 °C for one minute,

and then at 95 °C for five minutes, during which the cross-linking process was completed as the exposed SU-8 became polymerised. The masked, unexposed SU-8 was then removed by development in ethyl lactate for approximately five minutes, after which the unwanted resist was completely dissolved, as illustrated in Figure 4.2b. The completed mould was then washed in IPA and DI-H_2O, and dried with N_2.

PDMS was prepared for casting over the mould by thoroughly mixing the elastomer curing agent and base (1:10 by volume), and then degassing in a vacuum oven at 20 mbar for approximately ten minutes, or until all of the air bubbles trapped in the polymer had been released. The mould was then placed in a Petri dish, and the PDMS poured over, as shown in Figure 4.2c. The elastomer was again degassed at 20 mbar to remove any air that had become trapped, after which the PDMS was cured at 80 °C in an oven for one hour, after which it was peeled off the mould master and cut to size with a razor blade. If necessary, a biopsy punch was used to make inlet and outlet holes in the PDMS channel for the insertion of capillary tubing.

The fabrication of deep microfluidic channels, and therefore tall (>100-µm-thick) SU-8 features introduces an increased risk of thermally-induced cracking, and the possibility of a reduced bond strength between the resist and the substrate material; thus some variations were made to the SU-8 process when thick layers were required. SU-8 strongly absorbs ultraviolet light at wavelengths below 350 nm, which can result in overexposure of the top surface of the resist, and an insufficient dosage deeper into the film, limiting the bond-strength between the SU-8 and substrate. Hence, to avoid delamination, thicker SU-8 layers were exposed through the substrate to ensure that the greatest dose was received by the resist closest to the interface.

A lithographic mask was defined on the glass microscope slide by first cleaning in acetone, IPA, and DI-H_2O for five minutes per solvent in an ultrasonic bath, after which the slide was baked at 200 °C to desorb any water from the surface. A 1.4-µm-thick layer of S1813 was deposited by spin-coating at 4000 rpm, followed by a four minute bake at 110 °C. As illustrated in Figure 4.3a, the S1813 was exposed through a light-field mask of the final microfluidic channel design, and the slide was then transferred to chlorobenzene for five minutes, which reacted with the S1813 to harden the top surface. Upon removal, the device was thoroughly dried with N_2,

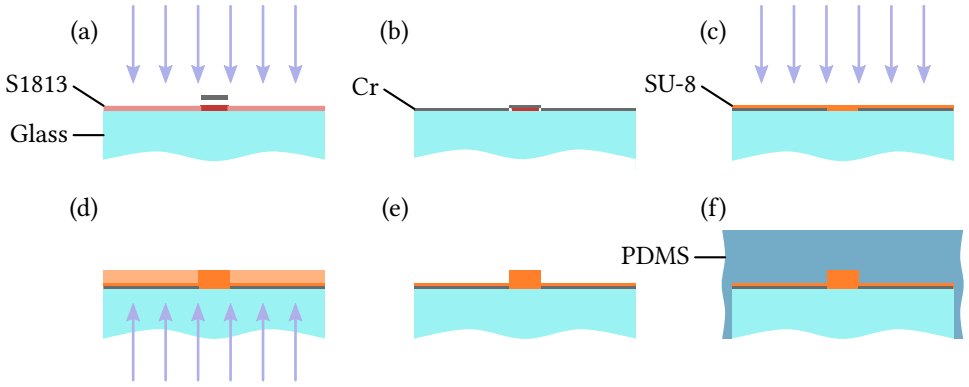

Figure 4.3: (a) An S1813 film was spun onto a glass microscope slide and exposed to ultraviolet light through a lithographic mask. (b) An undercut was created in the S1813 by soaking in chlorobenzene prior to development, which aided clean separation of the deposited Cr. (c) A base layer of SU-8 was spun over the mask, and flood exposed to create a fully cross-linked film. (d) A thicker layer of SU-8 was then applied, and exposed to ultraviolet light through the substrate (and therefore through the integrated mask). (e) The masked resist that had not been exposed was removed with ethyl lactate solvent, after which (f) PDMS was cast over the mould and cured.

and then the resist was developed in MF-319 for approximately two minutes, until the unwanted S1813 had been removed. As shown in Figure 4.3b, the chlorobenzene-treated surface was developed more slowly by the MF-319, resulting in an undercut that aided in the lift-off of the subsequently deposited metal. To prepare for metallisation, the slide was exposed to a 50 W O_2-plasma for 40 seconds, which removed any remaining resist residue. A 100-nm-thick layer of Cr was then evaporated onto the device using an electron beam evaporator, after which it was washed in acetone to remove the S1813, and lift-off the unwanted metal. In preparation for SU-8 deposition, the completed mask was thoroughly washed in IPA and then DI-H_2O, to remove any traces of organic solvent, after which it was cleaned in a piranha etch solution.

It was found that casting PDMS directly onto a metal-coated glass slide resulted in buckling of the elastomer surface after heating, similar to the deformation observed when evaporating metal directly onto PDMS [121]. Previous studies have measured the height of these surface undulations to be approximately 1.5 µm [121], which would be problematic when used in the fabrication of a water-tight microfluidic channel. Therefore, as shown in Figure 4.3c, a 20-µm-thick base-layer of SU-8 2025 was deposited over the mask and flood exposed, after which it was baked to fully

cross-link the resist. The channel mould was then fabricated by successive applications of SU-8 2050 that were each spin-coated at 1500 rpm for 30 seconds to produce a 100-µm-thick film. Between applications, the film was baked at 65 °C for five minutes to partially evaporate the diluting solvent. When the desired thickness was reached, the resist was baked according to the manufacturer's instructions [120].

The SU-8 was exposed through the integrated mask, as illustrated in Figure 4.3d, and then baked at 65 °C and 95 °C to polymerise the exposed resist, after which it was developed in ethyl lactate until the unwanted SU-8 was removed, as shown in Figure 4.3e. PDMS was then cast over the mould using the same methodology as described for the thinner channels, as demonstrated in Figure 4.3f.

4.1.3 Techniques for bonding channels to on-chip waveguides

The fabrication techniques used in the manufacture of microfluidic devices typically lend themselves to the production of several layers with two-dimensional or simple three-dimensional structures that can then be bonded together to create more intricate three-dimensional circuits. There is therefore a great research interest in the development of bonding methods that are suitable for a wide range of materials, geometries, and environments. Specifically, the strength of an appropriate bonding method must be sufficient to withstand the pressures and temperatures applied during use, and be chemically compatible with the analytes that the device is intended to contain.

Eddings et al. [79] published a comparative study of some common PDMS–PDMS bonding methods. These include a technique in which uncured PDMS is used as an adhesive layer between the two components to be bonded [122], and methods in which the layers are only partially cured before being brought into contact [123], or the components are each produced with an excess of either the curing or base agents such that the excesses react when brought into contact and bond the layers [124]. The study also discusses the O_2-plasma [125] and corona discharge [126] surface-modification techniques, where the PDMS surfaces are chemically activated so that they bond when brought into contact. Eddings et al. fabricated nine replicate devices using each technique and measured the air pressure that the bonds could withstand

Table 4.1: The minimum and maximum bond strength of five different PDMS–PDMS bonding techniques as measured by Eddings et al. [79]. The results are organised by the average pressure at which the bond integrity was compromised, and the range is included as an indication of the repeatability of each method.

Method	Minimum (bar)	Maximum (bar)	Range (bar)	Average (bar)
Uncured PDMS	5.52	6.98	1.46	6.79
Partial curing	3.88	6.97	3.09	6.58
Agent ratio	3.73	5.24	1.51	4.81
Oxygen plasma	1.87	5.26	3.39	3.21
Corona discharge	2.35	3.88	1.53	2.99

before they were compromised. The results of these tests are summarised in Table 4.1.

Given that the fabrication of the planar Goubau line devices to which microfluidic channels were bonded in this work is an expensive and time-consuming process, the methods used had to be highly repeatable to minimise wastage of otherwise functional devices. Therefore, the suitability of some of these techniques were explored to identify an appropriate bonding process that could be applied to the fabrication of microfluidic devices.

The stamp-and-stick method as tested by Eddings et al. [79] was found to produce the most reliable, high-strength bond. In this technique, first described by Satyanarayana et al. [122], a glass slide was spin-coated with a ~1.5-µm-thick layer of uncured PDMS, onto which one of the moulded components was stamped such that a thin layer of the uncured elastomer was transferred, as illustrated in Figures 4.4a to c. The coated component was then brought into contact with a glass slide and cured at 90 °C, after which a strong PDMS–glass bond capable of withstanding pressures between 4 bar and 7 bar was formed between the two layers [122].

The applicability of this method was tested by fabricating an on-chip planar Goubau line device on a quartz substrate, as described in Chapter 3, and a PDMS microfluidic channel as per §4.1.2. The components were bonded using the uncured PDMS stamp-and-stick method. Figure 4.4d shows a micrograph of a 200-µm-wide channel, that was taken through the quartz substrate, in which it is clear that some of the PDMS adhesive was wicked into the channel through capillary action, resulting

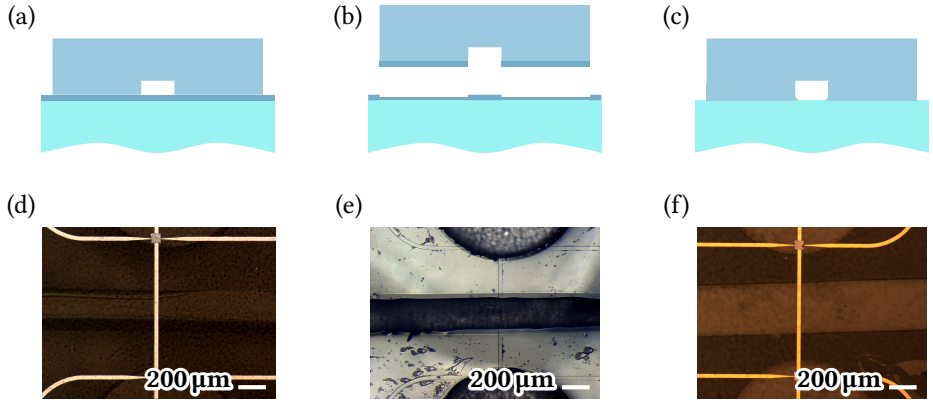

Figure 4.4: (a) A glass microscope slide was spin-coated with uncured PDMS, onto which a piece of moulded PDMS was stamped. (b) When peeled away from the glass slide, a thin layer of uncured PDMS adhered to the surfaces that were in contact. (c) The coated PDMS was then bonded to the target glass slide by curing at 90 °C. Some of the uncured PDMS may be wicked into the channel, resulting in a meniscus-effect at the PDMS–substrate interface. (d) Micrograph of a 200-µm-wide microfluidic channel (lighter region) that has been bonded to a 1-mm-long planar Goubau line. The dark bands at the edge of the channel are caused by wicking of the PDMS before it was cured. (e) Micrograph of a 300-µm-wide PDMS microfluidic channel that has been peeled off a device. The wicked bands of PDMS at the channel edges are more apparent than in (d). (f) A 400-µm-wide microfluidic channel that was bonded using only the PDMS curing agent, which did not create the meniscus-effect at the channel edges.

in a meniscus that ran along the cavity walls, and was cured in place. This effect is more clearly demonstrated in Figure 4.4e, which shows a 300-µm-wide PDMS channel that has been peeled from an on-chip device. The imprint of the conductors to which the elastomer had conformed is visible, as are the menisci that extend approximately 25 µm from either side of the channel wall. This additional PDMS introduces a degree of uncertainty to channel-width measurements, and therefore also to the interaction length between electric fields propagating along the conductor and the analyte in the channel. In addition, the wicking action presents a risk of sealing smaller (~10's of microns) channels when the uncured adhesive is transferred. It has been demonstrated that the less-viscous PDMS curing agent can be used to create the adhesive layer [127], which significantly reduced the wicking effect as shown in Figure 4.4f, but was also found to produce a reduced PDMS–glass bond strength of 2.5 bar to 4 bar [127].

Plasma bonding is a commonly discussed technique that does not rely on the use of any adhesive between the bonded layers [79, 128, 129], and is therefore well-suited to micron-scale geometries where blockage is likely. With this method, the material

interfaces to be bonded are exposed to an O_2-plasma that creates surface hydroxyl groups (−OH) that condense to form Si−O−Si bonds between the materials when brought into contact [125]. However, the processing parameters reported to produce the greatest PDMS–PDMS and PDMS–glass bond-strengths vary between publications, illustrated by the fact that powers ranging from 20 W [128] to 75 W [130] and chamber pressures between 9×10^{-2} mbar [129] and 1.3 mbar [128] have been identified as optimal.

The plasma bonding process was tested by first curing PDMS in a Petri dish, and then dicing it into 10 mm × 10 mm squares, while a scriber was used to divide glass microscope slides, which had been cleaned in a piranha etch solution, into 25 mm × 25 mm pieces. PDMS and glass sample pairs were then exposed to an O_2-plasma where an array of powers and pressures in the published optimal ranges were applied. It was found that most PDMS–glass samples that had been exposed to a <20 W O_2-plasma successfully bonded in some regions, but a complete interfacial bond between the two materials was never achieved. Eddings et al. [79] note that of the methods tested, the most unreliable results were produced by this technique, as indicated by the large range of bond strengths presented in Table 4.1.

The adhesion methods discussed thus far have been restricted to the bonding of PDMS to Si-based materials, however as demonstrated in §4.2.2, some device designs necessitate the bonding of PDMS to non-Si-based polymers. An irreversible chemical adhesion technique pioneered by Lee et al. [131,132] required only that it was possible to generate hydroxyl (−OH) groups on the surfaces to be bonded, through exposure to an O_2-plasma for example. 3-aminopropyltriethoxysilane (APTES) was anchored to one surface, and 3-glycidoxypropyltriethoxysilane (GPTES) to the other, such that an irreversible amine–epoxy bond was formed when the two surfaces were brought into contact.

The methodology used to form the amine–epoxy bond is independent of substrate, and therefore the same process was used here to bond PDMS to any material. The moulded PDMS and target substrate were exposed to a 50 W O_2-plasma for one minute, which created −OH hydroxyl groups on the surfaces, as shown in Figure 4.5a. The PDMS channel was then placed in a GPTES:IPA solution (1:49 by

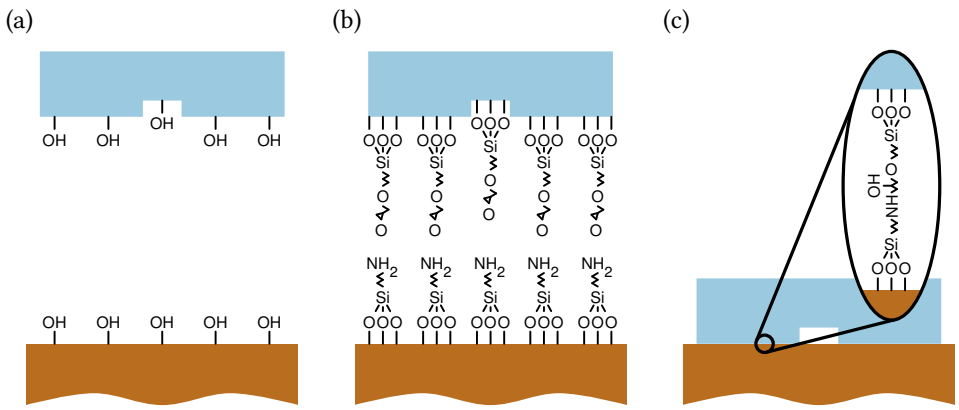

Figure 4.5: (a) Hydroxyl groups were generated on the PDMS and substrate surfaces by exposure to a 50 W O_2-plasma for one minute. (b) The PDMS and substrate were placed in GPTES:IPA and APTES:DI-H_2O solutions respectively, and left to react for twenty minutes, during which the silanes were anchored to the hydroxyl groups. (c) The functionalised surfaces were brought into contact and left to bond for one hour, after which an irreversible amine–epoxy bond was formed.

volume), and the substrate was placed in an APTES:DI-H_2O solution (1:49 by volume). The components were left in their respective solutions for twenty minutes, during which the silanes were anchored to the functionalised surfaces, as illustrated in Figure 4.5b. The PDMS and substrate were then thoroughly washed in DI-H_2O, and brought into contact. After one hour, a strong amine–epoxy bond was formed, as shown in Figure 4.5c, that has been shown to withstand pressures between 5 bar and 6 bar [132].

4.1.4 Isolation of electronics and overlaid liquids

As discussed in §4.1.1, some device designs required that the separation between the liquid analyte and photoconductive switches was minimised, and that the microfluidic channel overlaid the switching regions. To achieve this, the on-chip device had to be coated with a terahertz-transparent, electrically and chemically insulating film to which the microfluidic channel could be bonded, creating a physical barrier between the liquid and biased switches. The environment in the immediate proximity of a photoconductive switch severely limits the choice of materials that can be overlaid, for example the electric field in the switching region was between $2 \times 10^6\ \mathrm{V\,m^{-1}}$ and $6 \times 10^6\ \mathrm{V\,m^{-1}}$, and the power density of the focused 10 mW laser (as discussed in §3.2.2) was of order $10^7\ \mathrm{W\,m^{-2}}$, which contributed to localised heating of the ma-

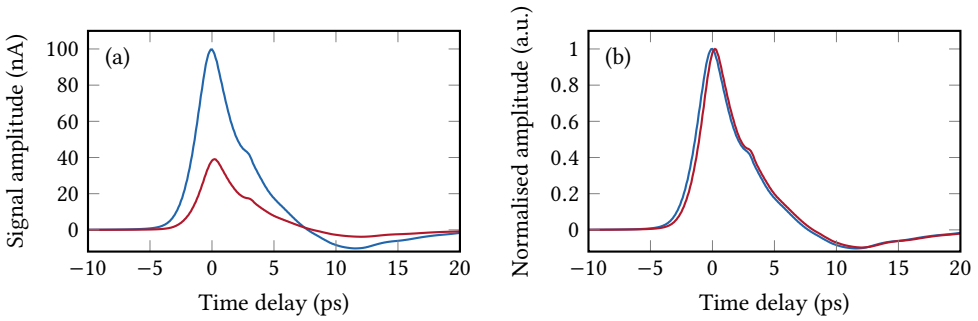

Figure 4.6: (a) Picosecond pulses recorded after propagation along an unloaded 1-mm-long planar Goubau line (blue) that was then coated in a 2.2-µm-thick layer of SU-8, and then remeasured (red). (b) The data in (a) was normalised to more clearly show the propagation delay introduced by the additional dielectric load.

terials.

SU-8 is well-suited to the creation of permanent electrically insulating films, as it has a reported dielectric breakdown strength of approximately $4.4 \times 10^8\,\mathrm{V\,m^{-1}}$ and resistivity of order $10^{15}\,\Omega\,\mathrm{cm}$ [133]. The absorption coefficient of SU-8 at 1 THz is $25\,\mathrm{cm^{-1}}$ [134], which is an order of magnitude greater than materials such as quartz that are considered to be terahertz-transparent [90], but is significantly less than many of the intended sample liquids with which the device would be loaded. To investigate the loss introduced by an overlaid SU-8 film, the time-domain response of picosecond pulses transmitted along a 1-mm-long planar Goubau line device was measured before and after the waveguide was spin-coated with a 2.2-µm-thick layer of SU-8 2002, as shown in Figure 4.6. The time-domain data in Figure 4.6a show that the pulse amplitude measured for the SU-8-coated device was approximately 40 % that of the unloaded waveguide. Owing to the realignment of the system that was required between measurements, which typically introduced a change in amplitude of ±5 nA, it is not possible to use this result to determine the absorption coefficient of the resist, but it nonetheless does show a substantial attenuation of the propagating signal. The normalised plots of the same data in Figure 4.6b more clearly show the group propagation delay increase of $0.25\,\mathrm{ps\,mm^{-1}}$ that was also introduced by the dielectric load of the resist.

The performance of SU-8 as a physical barrier between a liquid analyte and the biased photoconductive switches was tested by bonding a 100-µm-deep PDMS channel to the SU-8-coated device using the amine–epoxy bonding technique described

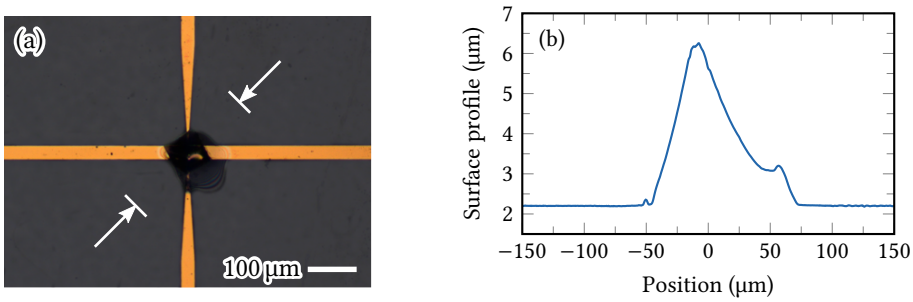

Figure 4.7: (a) A micrograph of a photoconductive switch that had been coated with a layer of SU-8. The heat of the laser caused expansion of the resist film that allowed the biased switch to be electrically shorted by the conductive liquid analyte. (b) The distortion of the damaged SU-8 film between the arrows in (a) as measured by a surface profiler.

in §4.1.3. When the channel was filled with DI-H_2O, the current supplied to the biased switch by the voltage source exceeded its protective output limit, preventing measurement. After this, the liquid was removed. The switch was found to be irreversibly damaged, as an uncharacteristically high dark current was measured, and picosecond pulses were no longer produced. These findings suggested that the biased switch had been electrically shorted by the introduction of the liquid, which was therefore not isolated by the SU-8 film. The micrograph in Figure 4.7a shows discolouration of the switching region, and the optical banding around the switch perimeter suggests that the integrity of the SU-8 film had been compromised. A surface profiler was used to measure the height of the SU-8 film across the region indicated in Figure 4.7a. As shown in Figure 4.7b, the film height increased to more than 6 µm; given the brittle nature of SU-8, it is likely that this expansion resulted in cracking of the film, which exposed the biased switch to the overlaid liquid. SU-8 is known to be sensitive to thermal fluctuations, exacerbated by the high tensile stress that is established during fabrication [135]. It is therefore possible that localised heating in the vicinity of the photoconductive switch resulted in the expansion, and subsequent failure, of the film.

An alternative low-loss material with a high dielectric breakdown strength that was more thermally-robust was therefore sought. Benzocyclobutene (BCB) has been used previously as a substrate material for microstrip waveguides operating in the terahertz-frequency-range [21,44], and has a breakdown voltage of 5.3×10^8 V m^{-1} [136] (comparable to that of SU-8) and a resistivity of order 10^{19} Ω cm [137], which is four

orders of magnitude greater than that of SU-8.

A BCB insulation layer was created by first cleaning the target device in acetone, IPA, and DI-H_2O for five minutes each, after which it was ashed in a 50 W O_2-plasma for one minute. To enable electrical connections to be made with the insulated chip, a piece of adhesive film was used to mask the bond pads to which Au-wire was to be affixed later in the fabrication process. Here, the BCB 4024-40 formulation was used, which is designed to produce a final film thickness between 3.5 µm and 7.5 µm. The resist was deposited by first spin-coating at 500 rpm for ten seconds to evenly distribute the resin, after which the spin-speed was increased to 2000 rpm for thirty seconds, reported to produce a 5.9-µm-thick final film. After spin-coating, the adhesive film was removed from the bond pads as the viscosity of the BCB film was sufficient to avoid unwanted flow. The device was then transferred to an 80 °C hot plate and baked for 90 seconds to drive out any residual solvent, after which it was moved to a vacuum oven to be cured. BCB films are degraded by oxidation when heated above 150 °C in an O_2-atmosphere (>150 ppm). Therefore, the resin film was cured by first purging the vacuum chamber with N_2, and then baking at 250 °C for two hours. After curing, the completed device was ready to be bonded to a microfluidic channel with the amine–epoxy bonding process described in §4.1.3, which was found to resolve the thermal issues encountered with SU-8.

4.2 The integration of on-chip microfluidics

In any spectroscopic measurement, an understanding of the interaction between the probing field and sample-under-test is required so that sample parameters can be determined. Previous measurements of planar Goubau lines integrated with microfluidic chips have been restricted to observation of the relative change in signal amplitude as a sample is introduced, and the limited knowledge of propagation characteristics has prevented the extraction of useful parameters, such as the complex permittivity of a sample. In this work, reflection-geometry waveguide structures were first used to investigate methods of channel integration as they allow simultaneous measurement of the input and output response of a given device, thereby

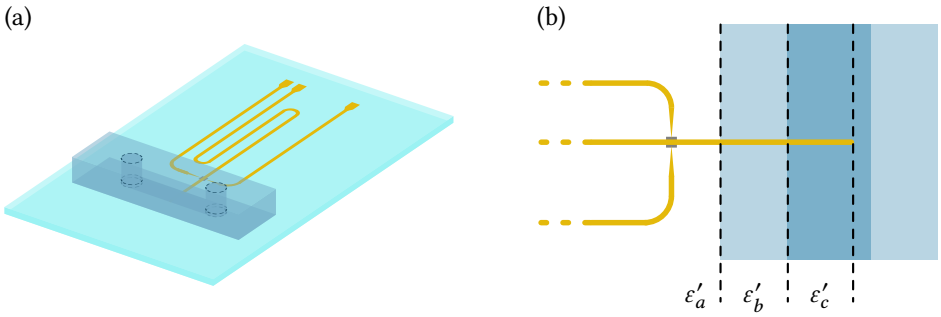

Figure 4.8: (a) A three-dimensional illustration of a 2-mm-long planar Goubau line that is terminated with an open-circuit stub. The overlaid microfluidic channel was positioned such that the transmission line was terminated within the cavity. (b) The overlaid channel created three regions of differing superstrate permittivity, ε'_a (air), ε'_b (PDMS), and ε'_c (analyte).

yielding important information that cannot be collected from transmission measurements. The findings were then used to inform the design and fabrication of the spectrometer discussed in §4.3.

4.2.1 Planar Goubau lines in reflection-geometry

As discussed, the majority of microfluidic on-chip devices reported prior to this work comprised a microfluidic channel overlaid perpendicular to the transmission line [55, 60, 71]. In principal, picosecond pulses generated at the photoconductive switch propagate along the PGL and are guided through the channel wall and the analyte contained within. Here, a reflection-geometry planar Goubau line, based upon a coplanar analogue [91], was used to illustrate the complicating factors introduced by such a configuration.

Figure 4.8a shows a planar Goubau line geometry that comprises a single photoconductive switch pair and a 2-mm-long transmission that is terminated with an open-circuit stub, over which a microfluidic channel has been bonded. The design was patterned on a 500-µm-thick quartz substrate, and a 400-µm-deep microfluidic channel (defined in PDMS) was bonded to the top surface so that the stub was terminated within the channel cavity, as shown in Figure 4.8b. Silicone tubing was inserted into the inlet and outlet ports that had been punched into the PDMS during fabrication, and a syringe pump was used to deliver or withdraw the liquid samples.

With this geometry, pulse generation and detection was performed using the single switch pair. A bias was applied to one of the switch arms, and picosecond

pulses were generated when illuminated with the femtosecond pump beam. The field coupled into the centre conductor propagated both along the parasitic delay line, and the open-circuit stub. Owing to the large impedance presented by the stub, the wave was reflected without a change in phase, as described by Equation 3.10. The perpendicular alignment of the microfluidic channel also created three regions of differing effective permittivity as a pulse propagating from the photoconductive switch towards the stub would transition from the the air-covered region, ε'_a, into the PDMS boundary, ε'_b, and then into the liquid-filled channel, ε'_c. A calibrated microscope was used to measure the lengths of each region after the channel was bonded; the distance from the switch to the PDMS boundary was 250 µm, the PDMS wall was 1150-µm-thick, and the distance from the channel boundary to the end of the stub was 650 µm. In addition to the reflection caused by the stub, a reflection coefficient can be determined for the interface between two regions of differing effective permittivity along the length of the transmission line, given that

$$Z = \sqrt{\frac{\mathrm{j}\omega\mu}{\sigma + \mathrm{j}\omega\varepsilon'}}, \tag{4.3}$$

where μ and σ are permeability and conductivity respectively. The materials considered here are non-magnetic ($\mu = 1$), and the conductivity is small relative to ε', and therefore

$$\Gamma = \frac{Z_2 - Z_1}{Z_2 + Z_1} \propto \frac{\varepsilon'_1 - \varepsilon'_2}{\varepsilon'_1 + \varepsilon'_2}. \tag{4.4}$$

Hence, if the effective permittivity ε'_2 is greater than ε'_1, the reflected wave will have a negative phase with respect to the incident pulse.

Figure 4.9a shows the time-domain traces measured for the geometry illustrated in Figure 4.8 before and after the microfluidic channel was bonded to the device. Both measurements comprised two main features, an input pulse (A) followed by the pulse reflected from the open-circuit stub (D). The temporal separation of these pulses in the unloaded device can be used to approximate the group propagation

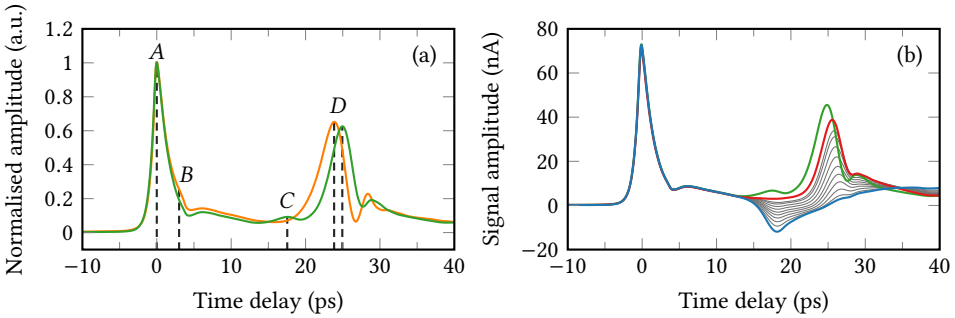

Figure 4.9: (a) Time-domain traces recorded before (orange) and after (green) a microfluidic channel was bonded to the surface of a reflection geometry device. After application of the channel, the generated pulse at time A was partially reflected by the PDMS boundaries, as demonstrated by the reflections at time B and C. The main reflection at time D was also delayed by the PDMS load. (b) Time-domain traces measured when the microfluidic channel was filled with air (green), propan-2-ol (red), and DI-H_2O (blue). Also shown are the responses as propan-2-ol was diluted with DI-H_2O in volume fraction intervals of 10 %.

velocity when the only superstrate material was air,

$$v_g = \frac{l}{\Delta t} = \frac{c}{\sqrt{\varepsilon'_{eff}}}, \tag{4.5}$$

where Δt is the difference in arrival time between the two pulses, l is the corresponding propagation distance, c is the speed of light in a vacuum, and ε'_{eff} is the effective permittivity over the distance l. For the unloaded device, Δt was found to be 23.84 ps, which equates to a group velocity of $1.68 \times 10^8\,\mathrm{m\,s^{-1}}$ over the total propagation length of 4 mm. After application of the PDMS channel, the round-trip distance from the photoconductive switch pair, to the PDMS boundary, and back to the switches, was 500 µm. According to Equation 4.4, the increase in effective permittivity introduced by this interface between ε'_1 and ε'_2 was expected to produce a negative-phase reflection. The decrease in amplitude at B occurred ~3 ps after the generated pulse, which corresponds both to a propagation distance of 500 µm when $v_g = 1.68 \times 10^8\,\mathrm{m\,s^{-1}}$, and the expected negative-phase of the partial reflection caused by the interface. Application of the same logic to the increase in amplitude at time C can be used to show that it is a positive-phase reflection owing to the decrease in permittivity at the interface between the PDMS wall, and the empty air-filled channel. After the channel was bonded to the device, the reflection from the stub at time D was delayed by approximately 1.1 ps, owing to the lower propagation

velocity in the PDMS-loaded region ε_2'.

The most significant issue with this channel alignment concept was demonstrated by filling the channel with propan-2-ol and DI-H_2O liquid samples, as shown in Figure 4.9b. The permittivity of propan-2-ol is comparable to that of PDMS; as such, no reflection was observed at the PDMS–propan-2-ol interface around 15 ps, and the most significant feature was the pulse reflected from the open-circuit stub. In contrast, the high permittivity of DI-H_2O resulted in a significant reflection from the channel boundary, which dominated the response with a negative-phase reflection. Measurements were also taken as propan-2-ol was diluted with DI-H_2O in 10 % volume fraction intervals. The incremental transition from the most significant reflection originating from the stub to the channel boundary is clearly displayed. The interaction between the terahertz field and the sample was therefore strongly dependent on the permittivity contrast between PDMS and the sample in the channel. To accurately extract the sample permittivity from such a structure would require a propagation model that incorporates both the Fresnel reflections from the various material interfaces, and the Fabry–Pérot cavity oscillations as pulses are reflected between two interfaces, similar to the models that are used in the permittivity extraction of samples contained within a flow-cell in free-space systems [32]. As discussed, appropriate models have not yet been derived for the planar Goubau line, thus performing spectroscopic measurements with such a design is not possible. Therefore, the device design was modified to remove the source of these problematic reflections.

4.2.2 Through-substrate measurement with thin films

To avoid the partial reflection of pulses by impedance-mismatched boundaries, it was necessary to remove the material interfaces in the direction of propagation. This was first achieved by moving the microfluidic channel to the underside of the substrate so that the biased photoconductive switches were electrically isolated from the liquid samples. However, this geometry required that the substrate thickness was reduced so that the extent of the terahertz electric field was sufficient for there to be a measurable interaction between the sample liquid and a propagating pulse. Gacemi et al. [138] mapped the extent of the electric field around a planar Goubau line with

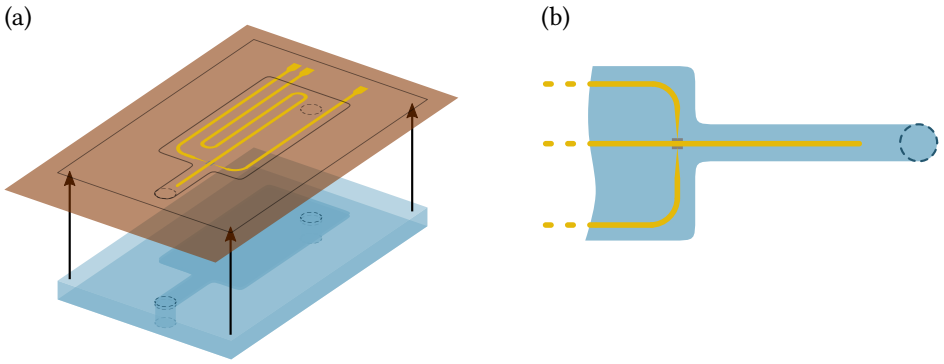

Figure 4.10: (a) Three-dimensional illustration of a reflection-geometry planar Goubau line patterned on a 50-µm-thick polyimide film. A 400-µm-deep microfluidic channel was bonded to the underside of the substrate. (b) A schematic of the channel alignment with respect to the transmission line, the lack of impedance boundaries along the length of the conductor prevents the unwanted generation of reflections.

an electro-optic sensing technique, and found that the field intensity halved when the crystal was moved to be approximately 60 µm from the conductor. Also, Russell et al. [94] showed that the effective permittivity of a planar Goubau line patterned on a quartz substrate diminished as the substrate thickness was reduced to less than 250 µm, and a more significant decrease was observed for substrates less than 100-µm-thick; the decrease in effective permittivity was ascribed to the extension of the electric field into the air beneath the substrate. These previous investigations suggested that a substrate thickness less than 100 µm was required, however quartz substrates of the necessary dimensions become impractically fragile when thinned to this extent. Therefore, a 2-mm-long reflection-geometry planar Goubau line was patterned on a 50-µm-thick polyimide film—another common substrate material used in the fabrication of on-chip transmission lines [109, 139].

As shown in Figure 4.10, a 1-mm-wide, 400-µm-deep microfluidic channel was cast in PDMS, and bonded to the underside of the device. The channel depth was selected such that there was almost no interaction between the propagating field and the PDMS material. In this configuration, the superstrate over the entirety of the device was air, and the substrate was a layered structure comprising the polyimide film, and the liquid sample in the channel. Samples were inserted at the inlet port shown in Figure 4.10b, and withdrawn from the outlet over the parasitic meandering region of the transmission line.

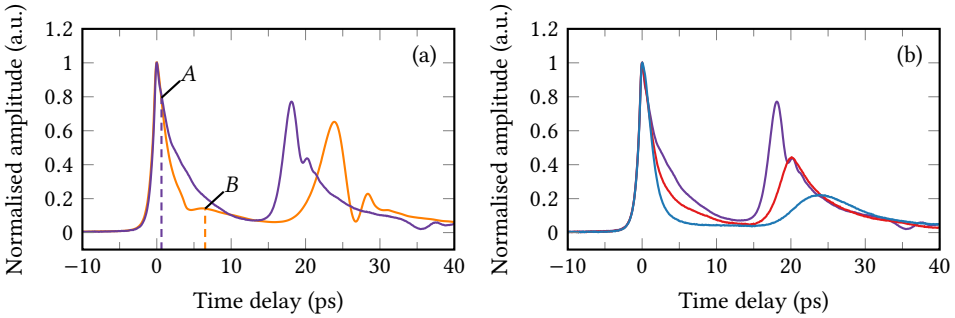

Figure 4.11: (a) Time-domain responses recorded from reflection-geometry planar Goubau lines patterned on a 50-µm-thick polyimide (purple) and 500-µm-thick quartz (orange) substrate. *A* and *B* indicate the arrival time of the terahertz field that was reflected from the underside of the polyimide and quartz substrates respectively. (b) Time-domain responses recorded when the polyimide device was loaded with air (purple), propan-2-ol (red), and DI-H_2O (blue) samples.

Reducing the thickness of the substrate material resulted in a significant change in the shape of the input pulse, as illustrated in Figure 4.11a, which shows the time-domain response of the polyimide and quartz devices before the channels were bonded. As discussed, the terahertz electric field produced by the photoconductive switch extends in all directions, and therefore a portion of the field that was not coupled into the overlaid Goubau line propagated through the substrate material, and was reflected back to the detection switch by the substrate–air interface on the device underside [140], in accordance with the Fresnel reflectance loss described in Equation 3.9. For example, polyimide has a permittivity of $\varepsilon' = 3.6$ [141] in the terahertz frequency range, and therefore a pulse with 9.5 % of the incident amplitude was reflected by the polyimide–air interface. Using Equation 4.5, a propagation time of 0.63 ps was calculated for the field reflected in the device patterned on polyimide, as indicated by *A* in Figure 4.11a, and a delay of 6.5 ps was identified for the quartz-based device ($l = 1$ mm, $\varepsilon' = 3.8$ [90]), as indicated by *B*. The propagation time through the polyimide substrate was sufficiently short that the measured input pulse was a superposition of multiple reflections, hence it was significantly broader than the input pulse of the quartz-based device. A systematic study of this effect was conducted by Russell [88], in which a quartz substrate was progressively thinned, and the arrival time of the reflection was mapped.

Figure 4.11b shows the time-domain traces that were recorded when the poly-

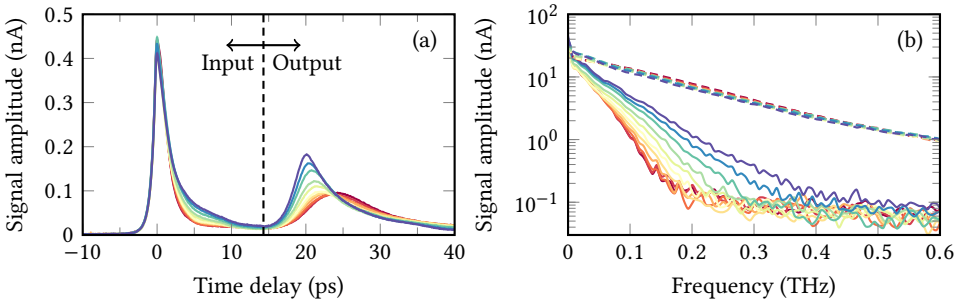

Figure 4.12: (a) The time-domain response of the polyimide-based reflection-geometry device when loaded with propan-2-ol:DI-H_2O mixtures with volume fractions from 0 % (purple) to 100 % DI-H_2O (red) in 10 % increments. (b) Fourier transforms of the 'input' (dashed) and 'output' (solid) pulses of each of the datasets in (a). Although the tail of the 'input' pulses differed as the volume fraction was varied, the spectral content was unaffected.

imide device was loaded with samples of propan-2-ol and DI-H_2O. As the channel was positioned on the underside of the substrate, the Fresnel reflectance of the substrate–sample interface was dependent on the analyte permittivity. For example, the permittivity of propan-2-ol is approximately $\varepsilon' = 2.5$ at terahertz frequencies [142], which equates to a Fresnel reflectance of less than 1 %, as such the broadening effect of the reflected pulses was less significant when the device was loaded with a propan-2-ol sample. Similarly, the high permittivity of DI-H_2O in this frequency range resulted in a narrower input pulse as the reflected field had a negative-phase.

Mixtures of propan-2-ol and DI-H_2O were prepared in which the volume ratio of DI-H_2O was increased from 0 % to 100 % in increments of 10 %. As shown in Figure 4.12a, the amplitude of the input pulse was unaffected by the introduction of the highly absorbing liquid samples, and the same broadening of the tail owing to the change in sample permittivity was observed. The reflection-geometry configuration is particularly useful when investigating new device designs as it allows simultaneous measurement of the picosecond pulse before and after propagation along the waveguide. The length of the 2 mm stub was sufficient for the effect of the input pulse to be negligible by 14.3 ps, after which the rise of the output pulse was observed. The recorded time-domain traces were therefore split into two separate responses. Input pulses were defined by windowing the time-domain data from −10 ps to 14.3 ps, and the output was defined as the data that occurred after 14.3 ps. Fourier transforms of the input and output pulses are presented in Figure 4.12b. Here, it is clear that

the broadening of the tail had little effect on the spectral content of the input pulses; this observation is of critical importance to spectroscopic measurements as the referencing methods used in time-domain spectroscopy require that the input field is not dependent on the sample material (see §1.2 and §4.3.4). The bandwidth of the input pulses extended to approximately 1.5 THz, although only the first 0.6 THz are shown here so that the output spectrum can be observed more clearly. The spectra of the output pulses show a clear frequency-dependent sensitivity to the increase in DI-H_2O concentration, however the significant attenuation owing to the sample loads restricted the sensitive bandwidth to between 100 GHz and 300 GHz, which is at the low-frequency end of what is defined as the terahertz frequency range.

The measurement bandwidth is primarily constrained by the interaction volume between the terahertz field and the attenuating sample, which can be reduced by either increasing the separation between the sample and the conductor, or by reducing the length of the transmission line. As discussed in §3.3.3, an increase in the substrate thickness can introduce additional propagation modes that further limit the measurement bandwidth, and is therefore an undesirable solution. As shown in Figure 4.12a, the output pulse arrived approximately 20 ps after the input signal, allowing isolation of the input and output pulses for further analysis. If the stub-length was reduced to decrease the interaction volume, the arrival time of the input and output pulses would overlap, creating a superposition of the two features that would be difficult to resolve analytically. Therefore, while the reflection configurations discussed here are useful for investigation of device performance, and developing an understanding of some complicating factors, they are not necessarily practical for use in the realisation of a terahertz-frequency spectrometer.

4.3 An on-chip microfluidic spectrometer

The investigation of reflection-geometry devices revealed that the design of a functional on-chip microfluidic spectrometer requires the liquid channel to be integrated such that the generation of reflections at impedance-mismatched interfaces is avoided, and that the interaction volume between the electric field and sample is sufficiently

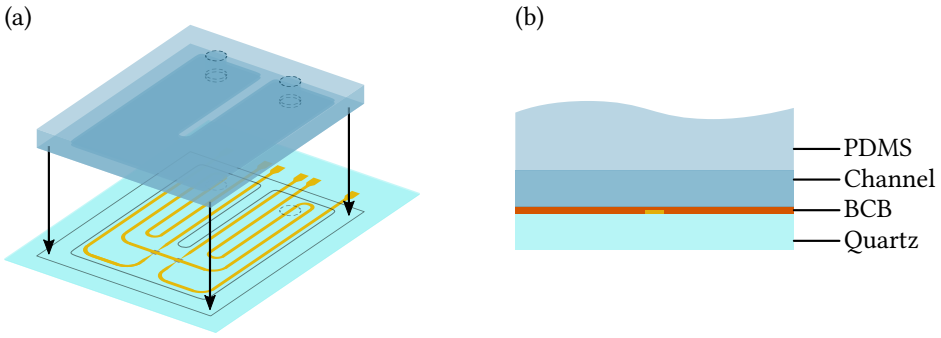

Figure 4.13: (a) Three-dimensional illustration of the transmission-geometry spectrometer. A 100-µm-deep channel defined in PDMS was bonded to the top surface of a 100-µm-thick quartz substrate which had been insulated with a 6-µm-thick layer of BCB. (b) The cross-section of the device was designed to be invariant along the length of the transmission line, thus removing any reflective interfaces.

small that the signal is not excessively attenuated. Considering these factors, a design was proposed in which the low-reflection transmission-geometry from §3.3.2 was patterned on a 100-µm-thick quartz substrate. The waveguide was isolated with a 6-µm-thick layer of BCB, and a 100-µm-deep microfluidic channel, cast in PDMS, was bonded to the top surface. The geometry, shown in Figure 4.13, was designed such that the cross-section of the layered structure did not change along the length of the transmission line, in order to both remove reflective boundaries, and to simplify further analysis.

Given that the planar Goubau line cannot be solved analytically, or at least the discovery of a solution is outwith the scope of this work, a numerical method was then developed in which an accurate model of the device structure was first simulated in HFSS, and used to calculate its propagation constants. It will be shown that the proposed stratified structure with an invariant cross-section enables the electromagnetic propagation mode to be simulated for an arbitrary length of transmission line, such that per-unit-length values can be determined; and that an accurate model of the device structure can be used to simulate the performance for a range of proxy samples, which then enables the complex permittivity of an unknown sample to be extracted from measured data.

4.3.1 Mechanical lapping of quartz-based devices

To produce an on-chip waveguide on a thin quartz substrate, the device was first fabricated on a 500-µm-thick quartz wafer using the methods described in Chapter 3, and was then spin-coated with a protective layer of S1813 at 1000 rpm, which was baked at 115 °C for four minutes. Quartz wax (Logitech) was melted onto a glass block that was heated to 110 °C, and the waveguide device was then placed face-down onto the wax, such that the surface to be lapped was exposed. The glass block was then placed in a bonding jig, which applied an evenly distributed force to the quartz surface, removed pockets of air trapped in the wax, and produced a plane-parallel bond between the glass block and quartz device as the wax cooled and set.

The quartz substrate was thinned on a lapping station at a rate of $10\,\mu m\,min^{-1}$ using an iron plate and an alumina (Al_2O_3) abrasive with a 9 µm grit size. To avoid damage to the quartz substrate, stress was relieved by melting the wax, and re-bonding the device to the glass block after 300 µm of quartz had been removed. After the quartz was lapped to a thickness of 100 µm, the abraded surface was polished, and the device was then released from the glass block by melting the wax. The wax residue was then dissolved in trichloroethylene, and the protective layer of S1813 was removed with acetone. Although fragile, the strength of the 100-µm-thick quartz device was sufficient to be spin-coated with BCB, and bonded to a PDMS channel using the methods described in §4.1.

4.3.2 Accurate HFSS models of waveguide structures

To construct a model that allowed the calculation of the Goubau propagation mode, the terahertz-frequency dielectric characteristics of the materials used to fabricate the microfluidic device were required. The properties of quartz [90], BCB [143], and PDMS [144] have been published in the terahertz frequency-range, and are often stated in the interchangeable terms of absorption coefficient, complex refractive index, or complex permittivity, as shown in Figure 4.14. The real and imaginary components of complex permittivity, $\tilde{\varepsilon} = \varepsilon' - j\varepsilon''$, and complex refractive index

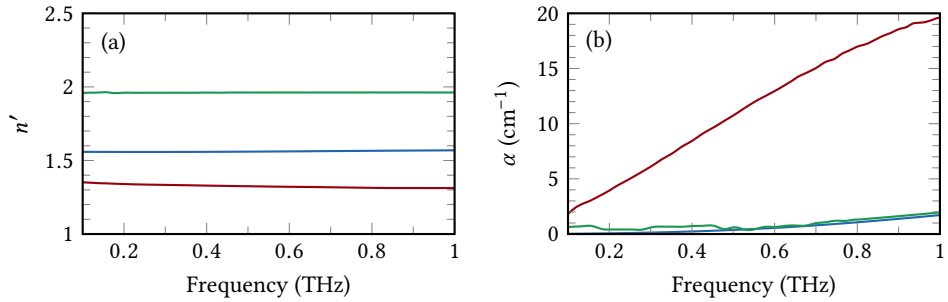

Figure 4.14: (a) The real component of the refractive index, and (b) the absorption coefficient of quartz [90] (green), BCB [143] (blue), PDMS [144] (red), as reported in literature.

$\tilde{n} = n' - jn'' = \sqrt{\tilde{\varepsilon}}$, describe the phase and attenuation losses in a sample respectively. The frequency-dependent absorption coefficient of a sample, α, can be calculated from its imaginary refractive index by

$$\alpha = \frac{2\omega n''}{c}. \tag{4.6}$$

HFSS requires that a sample's dielectric properties are given in terms of dielectric loss tangent, $\tan(\delta)$, and real permittivity, where the loss tangent is the ratio of the real and imaginary permittivity

$$\tan(\delta) = -\frac{\varepsilon''}{\varepsilon'}. \tag{4.7}$$

Therefore, values for ε' and $\tan(\delta)$ were calculated from those presented in literature, and input into HFSS as frequency-dependent material parameters.

In addition to accurate dielectric parameters, the model also required inclusion of the device geometry. While the nanofabrication processes used in the construction of these devices allow precise control of component dimensions, the compound uncertainty that results from many small design deviations necessitates accurate measurement of the device throughout fabrication. Therefore, the thickness of the substrate and PDMS channel were recorded using a non-contact gauge, and the depth of the BCB layer was measured with a surface profiler.

As discussed, simulation of the entire device structure, shown in Figure 4.15a, would be computationally expensive, and therefore a 3 mm × 1 mm × 3 mm (x, y, and z dimensions respectively) sub-section of the transmission line was instead modelled,

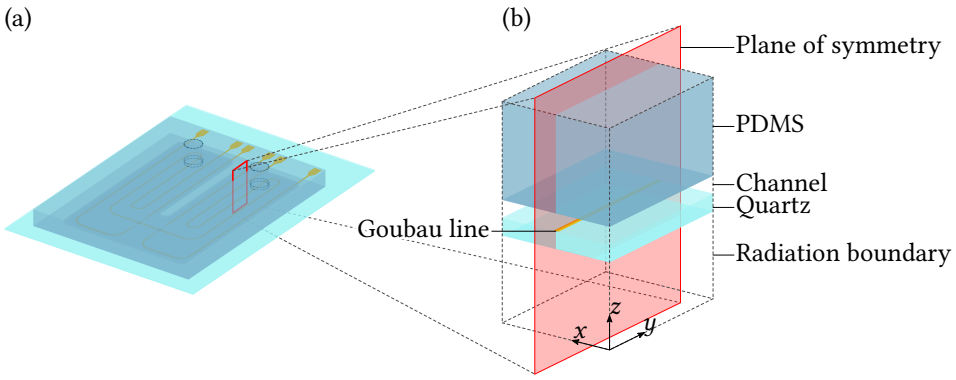

Figure 4.15: (a) The complete on-chip spectrometer device, upon which the model in (b) was based. The model comprised a 3 mm × 1 mm × 3 mm (x, y, and z dimensions respectively) vacuum region within a radiating boundary, in which the quartz substrate (coated with the BCB insulation layer), channel region, and PDMS channel wall were located according to measurements taken of a fabricated device. The plane of symmetry along the centre of the transmission line was exploited to reduce the required simulation time.

as shown in Figure 4.15b. The model dimensions were chosen such that the field at the edges of the model had decayed to a negligible magnitude. Owing to the uniform device cross-section, the propagation characteristics in the modelled cell were the same as those at an arbitrary point along the length of the transmission line. To further reduce the simulation resources required, symmetry along the length of the conductor was exploited, so that the electromagnetic field was only calculated for one half of the model, and mirrored across the plane.

Given accurate geometric and dielectric properties for each of the components in the device structure, the frequency-dependent propagation characteristics could be simulated. For example, Figure 4.16a and b show the complex permittivity of the Goubau propagation mode when the channel was loaded with air ($\tilde{\varepsilon} = 1 - \mathrm{j}0$), as simulated with HFSS. The frequency-dependence of these terms can be understood by considering properties of the materials surrounding the centre-conductor, and the extent of the evanescent electric field as a function of frequency. As shown in Figure 4.16c and d, the extent of the evanescent field decreases with frequency, such that the interaction between the field and the PDMS channel boundary is reduced. Of quartz and PDMS, PDMS has the greatest absorption coefficient, and the lowest real refractive index. Therefore, as the interaction between the PDMS and field is reduced, the real permittivity of the mode is increased, and the associated loss is decreased. In order to extract the dielectric properties of unknown liquid samples, the channel

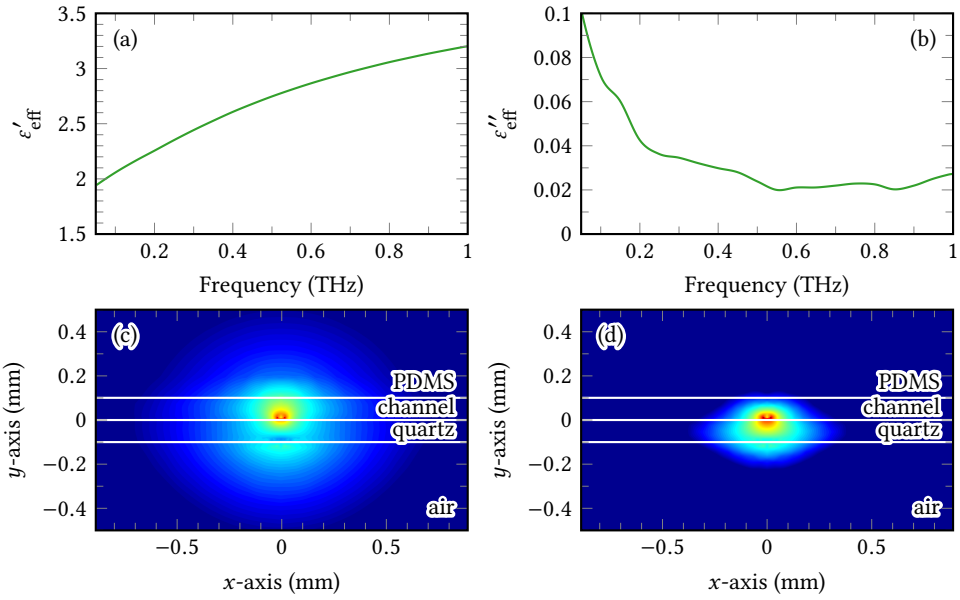

Figure 4.16: (a) The simulated real and (b) imaginary components of the complex permittivity of the Goubau mode when the channel was filled with air ($\varepsilon = 1 - \text{j}0$). (c) The simulated electric field distribution at 100 GHz and (d) 600 GHz.

region was modelled by defining a proxy material which had a programmatically variable complex permittivity, the selection of which is discussed in §4.3.3.

4.3.3 Parameter matrix reduction

The proposed method by which the dielectric properties of liquid samples are extracted relies on prior simulation of the device response to a range of proxy samples. Given that simulation of the waveguide structures discussed in §4.3.2 is time consuming, it is impractical to model all conceivable complex permittivities, and the problem domain must be somewhat constrained. For example, the complex permittivity of DI-H_2O, the greatest dielectric load considered in this work, ranges from approximately $\tilde{\varepsilon} = 8 - \text{j}14$ at 0.1 THz to $\tilde{\varepsilon} = 4 - \text{j}2$ at 1 THz [35]. In the most simple case, a proxy sample parameter matrix, $\tilde{\boldsymbol{\varepsilon}}_{\text{lut}}$, could be produced to define the problem domain such that the response of the device was simulated between the smallest (i.e.

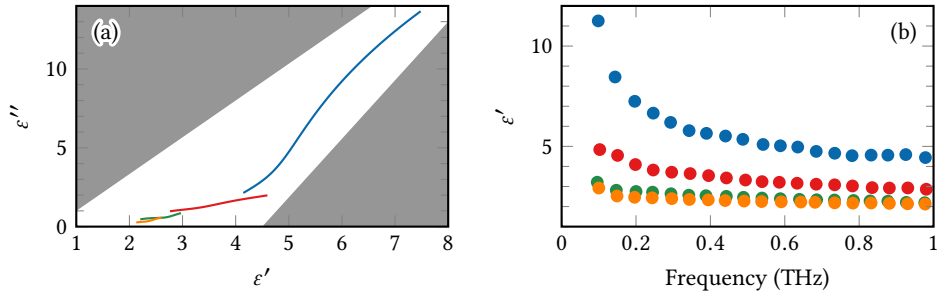

Figure 4.17: (a) Cole–Cole plots of DI-H_2O (blue), methanol (red), ethanol (green), and propan-1-ol (orange) between 0.1 THz and 1 THz, as measured by Kindt and Schmuttenmaer [35]. The shaded regions represent values in the parameter matrix that were omitted from simulation, owing to their relative distance from the complex permittivity of the target samples. (b) The real permittivity of the samples in (a) as measured by Kindt and Schmuttenmaer.

$\tilde{\varepsilon}_{\text{lut}} = 1 - \text{j}0$ in air) and largest loads,

$$\tilde{\boldsymbol{\varepsilon}}_{\text{lut}} = \begin{pmatrix} 1-\text{j}0 & 1-\text{j}0.5 & \cdots & 1-\text{j}14 \\ 1.5-\text{j}0 & 1.5-\text{j}0.5 & \cdots & 1.5-\text{j}14 \\ \vdots & \vdots & \ddots & \vdots \\ 8-\text{j}0 & 8-\text{j}0.5 & \cdots & 8-\text{j}14 \end{pmatrix}. \tag{4.8}$$

With a proxy sample step size of 0.5, the parameter matrix in Equation 4.8 comprises 435 elements, each of which requires simulation. However, through consideration of realistic target samples, it can be shown that many of these proxy samples can be discarded to reduce the size of the problem domain.

Kindt and Schmuttenmaer [35] measured the complex dielectric properties of several liquids that are of interest in biological systems, namely DI-H_2O, methanol, ethanol, and propan-1-ol. The corresponding Cole–Cole distributions of these samples are plotted in Figure 4.17a, in which it is clear that there is an approximately linear relationship between the real and imaginary components of complex permittivity in the terahertz frequency range. Therefore, the extrema in which either the real or imaginary component is dominant do not represent realistic samples, and need not be simulated. If the shaded regions in Figure 4.17a are removed from the parameter matrix, then the number of proxy samples to be simulated is decreased from 435 to 161. This equates to a 63 % reduction in the size of the problem domain, achieved by pre-emptively excluding simulations that would not be relevant

for analysis.

The real permittivity of the samples measured by Kindt and Schmuttenmaer are shown in Figure 4.17b, and it can be seen that the permittivity of each sample decreases as frequency is increased. Here, it is clear that it is unnecessary to simulate the highest permittivity proxy samples up to 1 THz. Therefore, the device propagation modes were simulated up to $\tilde{\varepsilon}_{\text{lut}} = 8 - \text{j}14$ below 0.4 THz, and only $\tilde{\varepsilon}_{\text{lut}} = 7 - \text{j}6$ between 0.4 THz and 1 THz, such that a total of 73 proxy samples were analysed. By restricting the simulated parameter matrix in this manner, the finite element simulations required for analysis of the results from a single device were completed in one eighth of the time that it would take to complete the original parameter matrix described in Equation 4.8.

4.3.4 Calculating the complex permittivity of measured samples

As discussed in §4.3.2 and §4.3.3, the planar Goubau line microfluidic spectrometer was modelled in HFSS, and the complex permittivity of the Goubau mode was simulated for a range of proxy samples. In lieu of an analytical propagation model for the planar Goubau line, the results of these finite element simulations can be used to determine the dielectric properties of an unknown liquid sample measured with the spectrometer. If the material properties and geometry used in the model accurately represent those of a fabricated device, then the simulated propagation coefficients when $\tilde{\varepsilon}_{\text{lut}} = 1 - \text{j}0$ can be assumed to be equal to those of the unloaded physical device, in which the channel is filled with air. Therefore, any measured change in the mode propagation resulting from the introduction of a liquid sample can be used to extract its dielectric properties.

The propagation constant, $\gamma = \zeta + \text{j}\beta$, is a mode property that can be calculated in HFSS, and describes the change in amplitude and phase of a travelling wave, where ζ and β are the per-unit-length attenuation and phase coefficients respectively. By convention, ζ and β are both negative in passive systems, indicating a loss in amplitude and phase through propagation. If the propagation constant of a mode is

known, its effective refractive index can be calculated from the relationship [145]

$$\tilde{n}_{\text{eff}} = \mathrm{j}\frac{\gamma}{k_0}, \tag{4.9}$$

where k_0, the free-space wavenumber, is given by

$$k_0 = \frac{\omega}{c}. \tag{4.10}$$

Although the propagation constant of the sample-loaded device, $\gamma_\mathrm{s} = \zeta_\mathrm{s} + \mathrm{j}\beta_\mathrm{s}$, cannot be measured directly, it is possible to measure the change in propagation coefficients, $\Delta\zeta$ and $\Delta\beta$, with respect to the propagation constant of an unloaded reference, $\gamma_\mathrm{r} = \zeta_\mathrm{r} + \mathrm{j}\beta_\mathrm{r}$, as simulated in HFSS. Therefore, the measurement of a sample required a measurement of picosecond pulse propagation when the microfluidic channel was filled with the liquid-under-test, and a measurement of an air-filled reference.

For example, Figure 4.18a shows the time-domain traces of picosecond pulses measured when the channel was filled with air, followed by propan-1-ol, which resulted in an attenuation and delay of the picosecond pulse. The Fourier transform of the measured field $E(t)$ has the complex form $\tilde{E}(\omega) = Ae^{\mathrm{j}\theta}$, where A and θ are the frequency-dependent amplitude and phase angle respectively, as plotted in Figure 4.18b and c. The phase-shift introduced by the sample is therefore $\varphi = \theta_\mathrm{r} - \theta_\mathrm{s}$ where the subscripts r and s indicate the reference- and sample-loaded measurements respectively. As previously stated, β is the per-unit-length phase coefficient, thus the change in β introduced by the addition of the sample, $\Delta\beta$, is

$$\Delta\beta = \frac{\varphi}{l}, \tag{4.11}$$

where l is the transmission line length. Hence, β_s was calculated by adding the measured sample-induced change in phase coefficient to the reference value simulated in HFSS,

$$\beta_\mathrm{s} = \Delta\beta + \beta_\mathrm{r}. \tag{4.12}$$

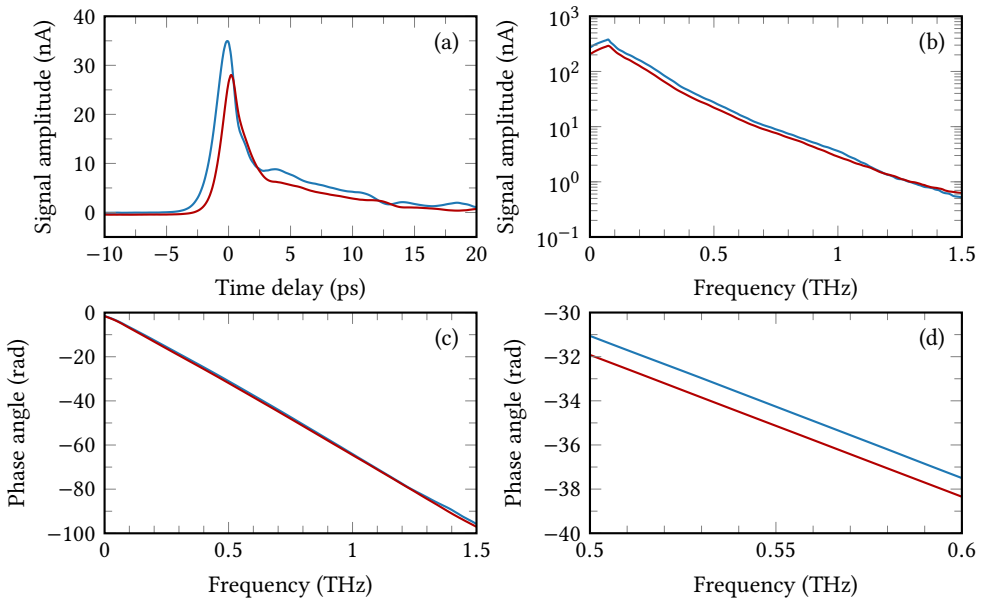

Figure 4.18: (a) Picosecond pulses measured after propagation along the 1-mm-long planar Goubau line device when unloaded (blue), and when the channel was filled with propan-1-ol. (b) The amplitude and (c) phase angle of the Fourier transformation of the data in (a). (d) The phase angle between 0.5 THz and 0.6 THz to demonstrate more clearly the difference between the reference and sample-loaded measurements.

The attenuation coefficient, ζ, is related to the signal amplitude by the Beer–Lambert law [29]

$$\frac{A_0}{A_{l,x}} = e^{\zeta_x l}, \tag{4.13}$$

where A_0 is the amplitude of the electromagnetic field generated at PC 1, and $A_{l,x}$ is the amplitude of the field after propagation over the distance l, which was measured at PC 2, and the subscript x indicates either a reference or sample measurement. The pump–probe experimental configuration does not enable simultaneous measurement of A_0 and A_l, but (as shown in Figure 4.12) the generated field can be assumed to be constant between the reference and sample measurements, such that

$$A_0 = A_{l,\mathrm{r}} e^{\zeta_\mathrm{r} l} = A_{l,\mathrm{s}} e^{\zeta_\mathrm{s} l}, \tag{4.14}$$

which can be rearranged to make ζ_s the subject,

$$\zeta_s = \frac{1}{l} \ln\left(\frac{A_{l,\mathrm{r}}}{A_{l,\mathrm{s}}}\right) + \zeta_\mathrm{r}. \tag{4.15}$$

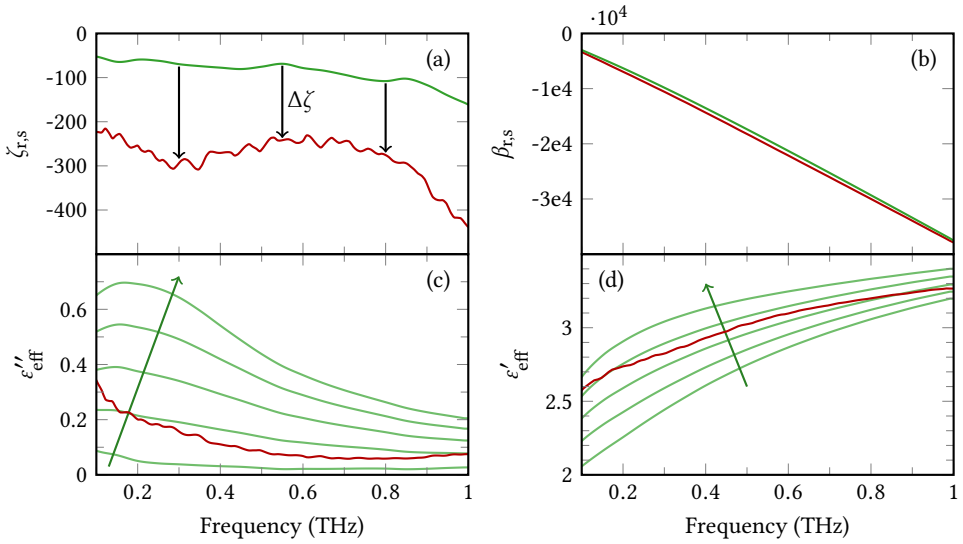

Figure 4.19: The measured change in the (a) real and (b) imaginary components of the propagation constant was added to the simulated reference values when $\tilde{\varepsilon}_{\mathrm{lut}} = 1 - \mathrm{j}0$ (green) in order to calculate the sample-loaded propagation constant (red). (c) The imaginary component of the measured effective permittivity (red) is shown with the imaginary component of the mode simulated for proxy samples (green) between $\tilde{\varepsilon}_{\mathrm{lut}} = 2 - \mathrm{j}0$ and $\tilde{\varepsilon}_{\mathrm{lut}} = 2 - \mathrm{j}2$ in increments of j0.5, ascending in the direction of the arrow. (d) The real component of the measured sample-loaded effective permittivity (red) and simulated (green) effective permittivity of the Goubau mode for proxy samples between $\tilde{\varepsilon}_{\mathrm{lut}} = 1 - \mathrm{j}0$ and $\tilde{\varepsilon}_{\mathrm{lut}} = 3 - \mathrm{j}0$ in increments of 0.5, ascending in the direction of the arrow.

The change in attenuation coefficient, $\Delta\zeta$, owing to the introduction of the sample is therefore the first term of Equation 4.15.

To calculate the complex permittivity of the propan-1-ol sample from the data presented in Figure 4.18, the simulated propagation constant of the device when loaded with an air reference ($\tilde{\varepsilon}_{\mathrm{lut}} = 1 - \mathrm{j}0$) was used, as demonstrated in Figure 4.19a and b. Equations 4.11 to 4.15 were then used to calculate the complex propagation coefficients of the device when loaded with the propan-1-ol sample, and the effective permittivity of the measured mode was calculated from Equation 4.9 (given that $n^2_{\mathrm{eff}} = \varepsilon_{\mathrm{eff}}$). In Figure 4.19c and d, the measured effective mode permittivity is plotted alongside those simulated for a selection of proxy samples with a complex permittivity comparable to that of the propan-1-ol sample. As the permittivity of propan-1-ol varies with frequency, the measured data does not align with any one proxy sample, and therefore the extraction of the sample permittivity is a two-dimensional interpolation problem.

At each frequency point, the problem domain can be visualised by plotting a

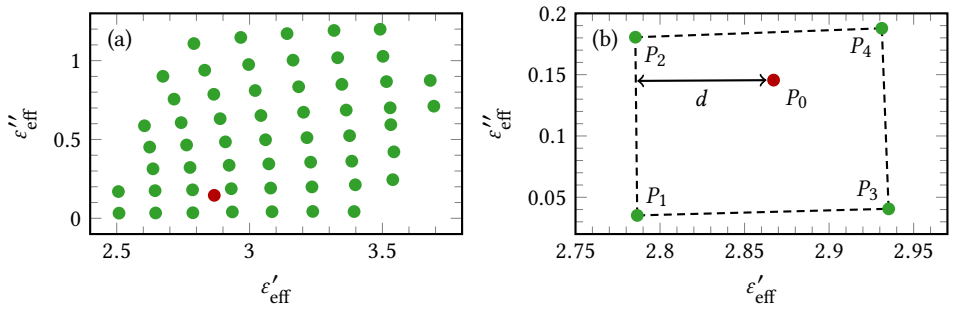

Figure 4.20: (a) The range of complex effective permittivities simulated in HFSS for each proxy sample (green) at 0.34 THz, also shown is the measured effective permittivity (red), the position of which is to be interpolated from the simulated dataset. (b) The simulated points P_{1-4} represent $\tilde{\varepsilon}_{\text{eff}}$ when $\tilde{\varepsilon}_{\text{lut}} = 2 - \text{j}0,\ 2 - \text{j}0.5,\ 2.5 - \text{j}0$, and $2.5 - \text{j}0.5$, respectively. The fractional distance from P_0 to the lines $\overline{P_1P_2}$ and $\overline{P_1P_3}$ was used to calculate the distance from the $\tilde{\varepsilon}_{\text{lut}}$ represented by P_1, and the $\tilde{\varepsilon}_{\text{lut}}$ represented by P_0.

Table 4.2: The proxy samples (with permittivity $\tilde{\varepsilon}_{\text{lut}}$) were identified as those that enclose P_0. The value of $\tilde{\varepsilon}_{\text{lut}}$ at P_0 was determined through two-dimensional interpolation with respect to the $\tilde{\varepsilon}_{\text{eff}}$ values at P_{1-4}. All data shown at 0.34 THz.

	P_0	P_1	P_2	P_3	P_4
$\tilde{\varepsilon}_{\text{eff}}$	$2.869 - \text{j}0.146$	$2.787 - \text{j}0.035$	$2.785 - \text{j}0.181$	$2.935 - \text{j}0.041$	$2.931 - \text{j}0.188$
$\tilde{\varepsilon}_{\text{lut}}$	$(2.278 - \text{j}0.367)$	$2 - \text{j}0$	$2 - \text{j}0.5$	$2.5 - \text{j}0$	$2.5 - \text{j}0.5$

Cartesian map of the simulated and measured effective permittivities, as shown in Figure 4.20a. Each point in Figure 4.20a represents the effective permittivity calculated for a given proxy sample permittivity at 0.34 THz, noting that a similar map could be produced for each frequency point in question. The interpolation method was carried out by first identifying the point in the array of proxy samples that was nearest to the measured point, P_0. Then, the adjacent three points that formed a quadrilateral with this point to enclose P_0 were identified, as shown in Figure 4.20b, where the surrounding points are labelled as P_{1-4}. The coordinates of each point in this specific example are given in Table 4.2. The sample permittivity, $\tilde{\varepsilon}_{\text{lut}}$, represented by P_0 was then obtained by first determining its location within the P_{1-4} quadrilateral, and interpolating the corresponding $\tilde{\varepsilon}_{\text{lut}}$ value with the following method. The perpendicular distance from the line $\overline{P_1P_2}$ to the point P_0 is

$$d\left(\overline{P_1P_2} \perp P_0\right) = \frac{\left|\det\begin{pmatrix} P_2 - P_1 \\ P_0 - P_1 \end{pmatrix}\right|}{|P_2 - P_1|}, \tag{4.16}$$

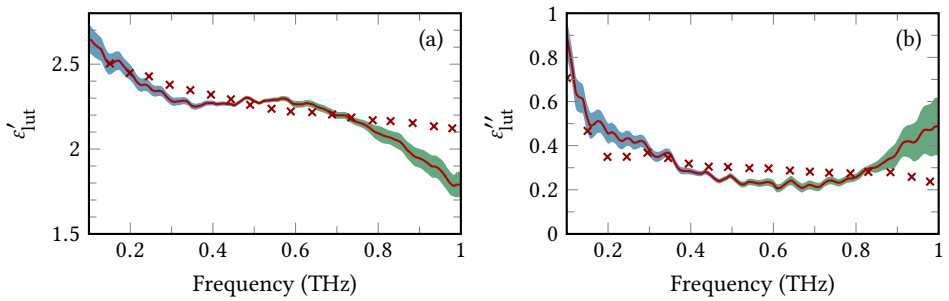

Figure 4.21: The (a) real and (b) imaginary components of the complex permittivity of propan-1-ol as extracted from the effective values given in Figure 4.19. The solid lines are the mean of five measurements of the same sample, and the shaded regions indicate the standard deviation (green), which becomes more significant above 0.8 THz, and the ±10 % channel height model error (blue). Also shown (×) is the complex permittivity of propan-1-ol as measured by Kindt and Schmuttenmaer [35].

as indicated by the line d in Figure 4.20b. It follows that the ratio of the distances from P_0 to $\overline{P_1P_2}$ and $\overline{P_3P_4}$ is

$$r' = \frac{d\left(\overline{P_1P_2} \perp P_0\right)}{d\left(\overline{P_1P_2} \perp P_0\right) + d\left(\overline{P_3P_4} \perp P_0\right)}. \tag{4.17}$$

For the example at 0.34 THz given in Table 4.2, r' was found to be 0.514. In terms of $\varepsilon'_{\text{lut}}$, there is a difference of 0.5 between the lines $\overline{P_1P_2}$ and $\overline{P_3P_4}$, and therefore the real component of the sample permittivity at P_0 was $\varepsilon'_{\text{lut}} = 2 + 0.5r' = 2.28$. This process was then repeated for the imaginary components to find the fractional distance, $r'' = 0.731$ from P_0 to $\overline{P_1P_3}$ and $\overline{P_2P_4}$, from which $\varepsilon''_{\text{lut}} = 0 + 0.5r'' = 0.37$ was identified.

The interpolation method was conducted at each of the measured frequency points, resulting in extraction of the frequency-dependent complex permittivity of the measured propan-1-ol sample, as shown in Figure 4.21. The same sample was measured five times, such that the mean and standard deviation could be calculated. As the data in Figure 4.21 shows, the standard deviation became significant above 0.8 THz, indicating that system noise dominated the analysis above these frequencies, preventing repeatable extraction of sample parameters.

The algorithm used to calculate the sample permittivity requires that the simulated model is an accurate representation of the device geometry, therefore structural changes in the device during measurement may introduce an additional error. It is

well-known that PDMS samples placed in contact with a solvent (such as propan-1-ol) will swell by up to 10 % [146]. Furthermore, since PDMS is an elastomer, a pressure excess in the channel volume may result in expansion of the channel dimensions. The latter problem can be controlled by limiting the sample flow rate; a low flow rate of $5\,\mu L\,s^{-1}$ was therefore chosen to minimise the induced pressure within the channel. To account for the possible changes in channel geometry from solvent-induced swelling of the PDMS, the device simulations were repeated to estimate the maximum error introduced at the channel height extrema, corresponding to ±10 % of the initial height of 100 µm. The corresponding difference in calculated permittivity is indicated by the shaded regions in Figure 4.21. The uncertainty owing to a change in the channel height reduced with frequency; as shown in Figure 4.16, the extent of evanescent field also decreases as a function of frequency, and therefore higher frequencies are less sensitive to changes in the channel height.

Previously, Kindt and Schmuttenmaer measured the complex permittivity of a selection of primary alcohols using a liquid flow-cell placed in a free-space terahertz time-domain spectroscopy system (see Chapter 5) [35]. As shown in Figure 4.21, the dielectric properties of propan-1-ol extracted using the technique developed here, and those presented by Kindt and Schmuttenmaer are in relatively strong agreement. Methods for quantifying the extent to which datasets agree are discussed in more detail in §4.3.5.

4.3.5 Verification of the extraction method

Given that a new technique for the extraction of the complex permittivity of an unknown liquid sample has been presented, it is necessary to verify the output of this analysis method. Hence, a comparative study was conducted against data available in literature. As mentioned, Kindt and Schmuttenmaer [35] measured the complex permittivity of the primary alcohols methanol, ethanol, and propan-1-ol using a free-space terahertz transmission system, incorporating a flow-cell fabricated from high-density polyethylene and high-resistivity silicon. Additionally, Barthel et al. [82] measured the same samples at frequencies accessible by rectangular waveguide bands [147], and Yomogida et al. [148] used a free-space spectrometer to mea-

Table 4.3: The triple-Debye model dielectric relaxation parameters calculated for propan-1-ol as reported by Kindt and Schmuttenmaer [35].

LUT	ε_{DC}	τ_1 (ps)	ε_2	τ_2 (ps)	ε_3	τ_3 (ps)	ε_∞
propan-1-ol	20.44	316	3.43	2.9	2.37	0.2	1.97

sure the liquids contained between polypropylene windows; Hirori et al. [149] and Møller et al. [83] both used reflection spectroscopy systems to measure the dielectric properties of methanol and ethanol, respectively. In some cases, these groups fit their respective datasets to a triple-Debye relaxation model, which aids quantitative comparison between the published results.

As discussed in §1.3.1, the Debye model decomposes the complex permittivity of a dielectric material into discrete relaxation and vibration terms that represent intramolecular rotation, reorientation, and hydrogen bonding processes that span several orders of magnitude in the frequency-domain [148, 150]. The dielectric response of protic solvents, such as methanol, ethanol, and propan-1-ol, is typically described with a triple-Debye relaxation model [82, 151], such that the frequency-dependent Debye permittivity $\tilde{\varepsilon}_D$, is described by the summation of the contributions made by each relaxation term [35],

$$\tilde{\varepsilon}_D = \varepsilon_\infty + \sum_{i=1}^{n} \frac{\varepsilon_i - \varepsilon_{i+1}}{1 + j\omega\tau_i}, \tag{4.18}$$

where ε_∞ is the high frequency permittivity limit of the sample, and ε_i are the n intermediate permittivity intervals, with the corresponding relaxation time constants τ_i.

Given the values of ε_i and τ_i, it is possible to replicate a reported triple-Debye relaxation model. For example, Kindt and Schmuttenmaer [35] reported the propan-1-ol parameters presented in Table 4.3, which describes three relaxation processes (ε_{DC}, ε_2, and ε_3) each with a corresponding relaxation time constant (τ_1, τ_2, and τ_3), and a high-frequency permittivity limit (ε_∞). Equation 4.18 was used to calculate $\tilde{\varepsilon}_D$ from the parameters in Table 4.3, and produce the triple-Debye model shown in Figure 4.22a and b. Here, in addition to the modelled permittivity, the frequency-dependent contributions of each of the summed components are also plotted, such

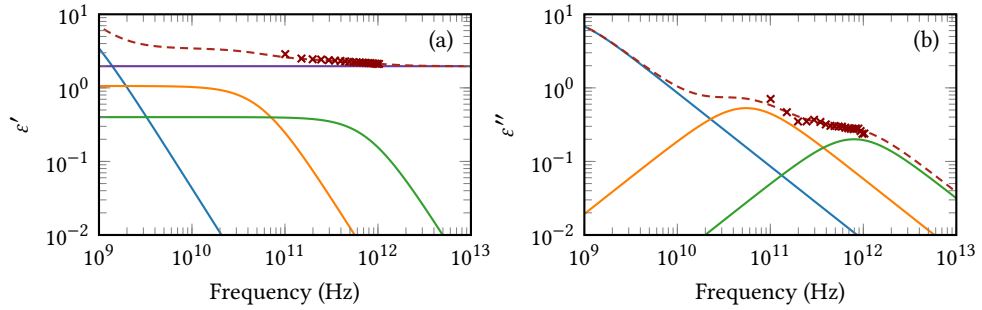

Figure 4.22: The (a) real and (b) imaginary components of the measured data (×), and triple-Debye model of propan-1-ol produced from the relaxation parameters reported by Kindt and Schmuttenmaer [35] (red, dashed), which is the sum of the contributions from $\varepsilon_{\mathrm{DC}}$ (blue), ε_2 (orange), ε_3 (green), and ε_∞ (purple).

that the effect of each relaxation term can be observed. The real component of the permittivity associated with a given term is effective up to the critical frequency of the corresponding time constant,

$$f_{\mathrm{c}} = \frac{1}{2\pi\tau_i}, \tag{4.19}$$

for example, the point of inflection of the second relaxation term in Table 4.3 is at 55 GHz, as shown in Figure 4.22a. The point of inflection in the real component of a particular relaxation term also corresponds to a maxima in the imaginary component. The critical frequency is significant when considering the relaxation terms that can be accurately resolved by a given dataset, as little spectral information can be accessed if f_{c} is outwith the sensitive bandwidth of the measurement [35, 82].

To verify data recorded with the on-chip spectrometer, samples of methanol, ethanol, and propan-1-ol were measured, and the complex permittivity of each liquid was extracted using the methods described in §4.3.4. The values obtained are plotted in Figure 4.23 alongside the data presented by previous authors. As shown by these plots, the established rectangular waveguide and free-space spectroscopy systems do not fully agree on the dielectric properties of the sample in question, however, the data recorded with the on-chip spectrometer developed in this work lie within the variance of the published datasets. The disagreement between datasets are likely to result from the compound errors of variation in sample quality (the purity of methanol used in this work was ≥99.8 %, yet ethanol was only 95 %, owing to the

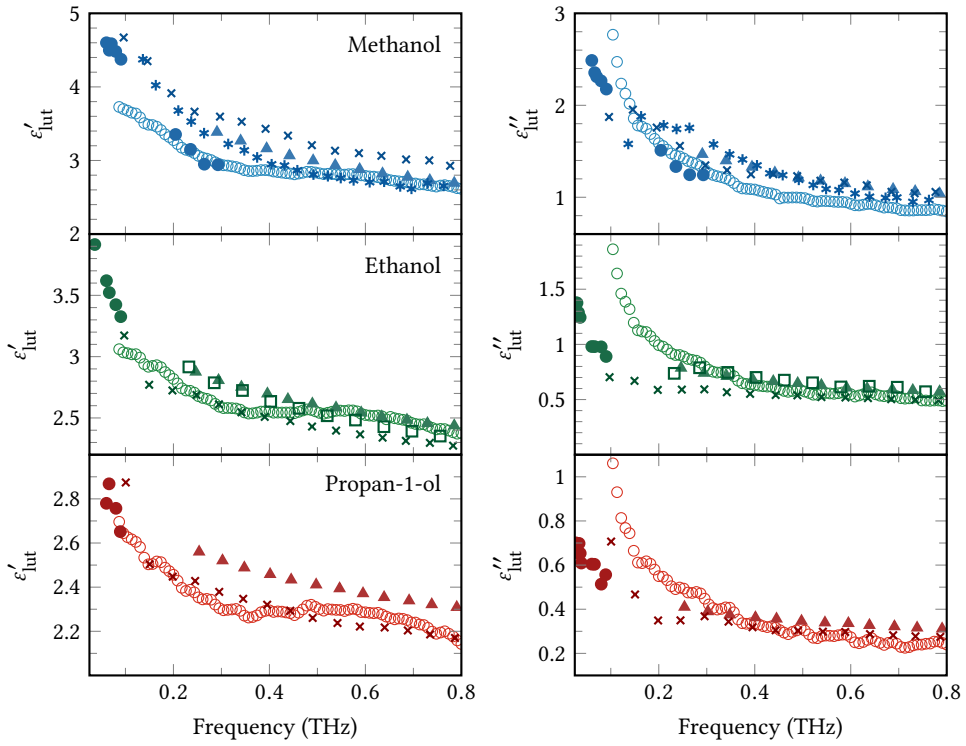

Figure 4.23: The real and imaginary components of the complex permittivity of methanol, ethanol, and propan-1-ol as measured using an on-chip spectrometer (○), compared to those from Barthel et al. [82] (●), Kindt and Schmuttenmaer [35] (×), Yomogida et al. [148] (▲), Hirori et al. [149] (∗), and Møller et al. [83] (□).

inherent cost of pure ethanol [152]), and errors in the system models employed. Each analysis method requires the use of a model to describe the interaction between a probing electromagnetic field and sample, and it has been shown that there is significant disagreement between research groups that have implemented similar models to measure identical samples [153]. Considering these factors, the agreement between the sample data measured using rectangular waveguide, free-space, and on-chip systems is within acceptable bounds.

Both Barthel et al. [82] and Kindt and Schmuttenmaer [35] published the triple-Debye relaxation parameters that were found to fit their data. The triple-Debye model in Equation 4.18 was fitted to the data in Figure 4.23 with a nonlinear least squares algorithm; a Levenberg–Marquadt [154] minimisation method was used to reduce the residual between the frequency-dependent values of $\tilde{\varepsilon}_{\text{D}}$ and the measured $\tilde{\varepsilon}_{\text{lut}}$ with each iteration, such that the real and imaginary components were concurrently fitted [83]. Given that the Debye model is used to describe dielectric relaxation

Table 4.4: The triple-Debye relaxation parameters for methanol, ethanol, and propan-1-ol fitted to data recorded with an on-chip spectrometer. Values in parentheses are those identified for the same samples in rectangular waveguide [82], and those in square brackets are for the same samples measured in a free-space system [35].

LUT	ε_{DC}	τ_1 (ps)	ε_2	τ_2 (ps)	ε_3	τ_3 (ps)	ε_∞
methanol	[32.63]	[51.5]	[5.91]	[7.09]	[4.9]	[1.12]	[2.79]
	(32.63)	(48)	(5.35)	(1.25)	(3.37)	(0.16)	(2.10)
	32.63	51.01	5.52	1.84	2.85	0.16	2.37
ethanol	[24.35]	[163]	[4.49]	[8.97]	[3.82]	[1.81]	[2.69]
	(24.35)	(161)	(4.15)	(3.3)	(2.72)	(0.22)	(1.93)
	24.35	161	4.45	4.16	3.34	0.69	2.24
propan-1-ol	[20.44]	[329]	[3.74]	[15.1]	[3.2]	[2.4]	[2.44]
	(20.44)	(316)	(3.43)	(2.9)	(2.37)	(0.2)	(1.97)
	20.44	328	3.79	14.2	3.05	1.01	2.16

over several orders of magnitude, it is essential that appropriate constraints are applied when fitting spectral data that is relatively narrow, such as that recorded in the terahertz frequency range. Therefore, as described in Reference 83, the triple-Debye model was constrained between 1 GHz and 200 GHz using the data presented by Barthel et al. [82], and ε_i and τ_i were initialised using the values from Kindt and Schmuttenmaer [35]. In each fitting operation, the static permittivity, ε_{DC}, was fixed at the initialised value [35].

The parameters reported in the previous works, and those found here, are presented in Table 4.4, and a good agreement is observed for the slower relaxation processes (τ_1). However, the critical frequency of the fastest relaxation processes (τ_2 and τ_3) identified by Kindt and Schmuttenmaer was beyond the spectral range of the rectangular waveguide data, and also at the high frequency limit of the on-chip system in some cases (e.g. 0.2 ps ≡ 795 GHz). It is therefore difficult to accurately resolve these processes with all systems, resulting in some disagreement between the parameters fitted to these terms. However, the parameters that were found to fit the on-chip spectrometer data in Table 4.4 were typically between thos values reported for the lower-frequency rectangular waveguide system [82], and the higher-frequency free-space spectrometer [35].

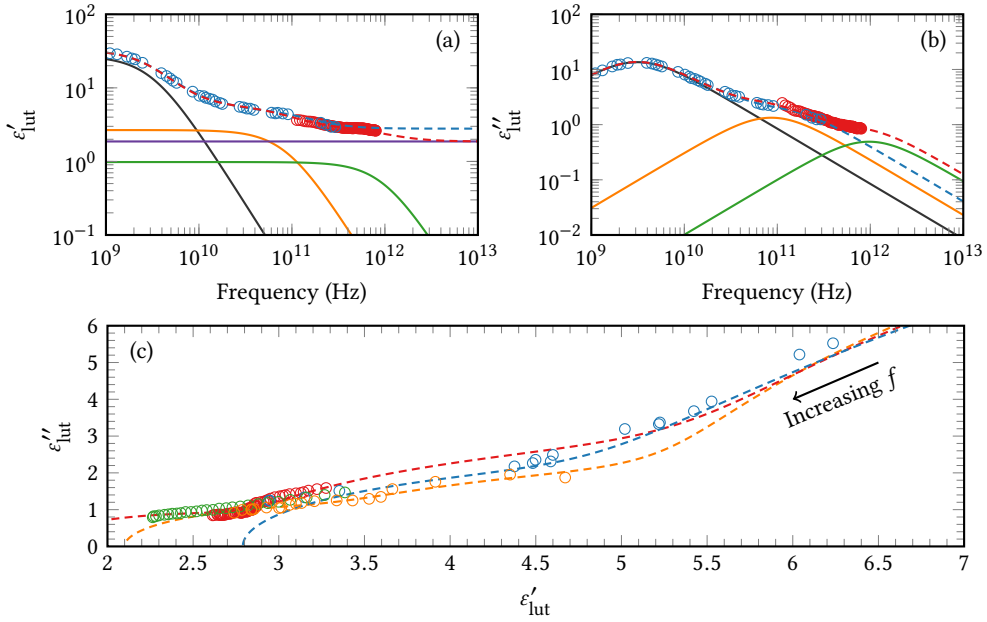

Figure 4.24: (a) The real component of the complex permittivity of methanol as measured by Barthel et al. [82] (○, blue), and as measured with the on-chip spectrometer (○, red). The triple-Debye model fitted to the on-chip data (red, dashed), and its components ε_{DC} (grey), ε_2 (orange), ε_3 (green), and ε_∞ (purple) are also shown. The triple-Debye model from the parameters given in Reference 82 is also shown (blue, dashed). (b) The imaginary components corresponding to the data in (a). (c) A Cole–Cole representation of the complex permittivity of methanol as measured in this work (○, red), by Barthel et al. (○, blue), by Kindt and Schmuttenmaer (○, orange), and by Yomogida et al. (○, green). The dashed lines represent the corresponding triple-Debye relaxation models, and the arrow indicates the direction of increasing frequency.

Figure 4.24a and b show the triple-Debye model that was fitted to the measured complex permittivity of methanol by Barthel et al., and to the on-chip data recorded in this work. Given that the on-chip fit was constrained by this low-frequency data, the two models are in agreement below 100 GHz. However, beyond this frequency, the additional data introduced by the on-chip measurements resulted in a revision of the faster relaxation terms (τ_2 and τ_3), and a corresponding change in the model permittivity. Figure 4.24c shows the Cole–Cole representation of the data recorded with each system, and the methanol Debye relaxation models described in Table 4.4. Given that each of the models were constrained by the same low-frequency (high-permittivity) data, there is a good agreement between $\varepsilon'_{lut} = 6$ and $\varepsilon'_{lut} = 7$, however the models diverge at the introduction of the high-frequency data. Yomogida et al. did not publish the relaxation parameters found to fit their free-space data, but the model fitted to the on-chip data recorded here showed the best agreement.

4.4 Concluding remarks

A development process has been discussed which resulted in the fabrication of a terahertz-frequency on-chip microfluidic spectrometer that was used to measure the complex permittivity of liquid samples. It was demonstrated that a microfluidic channel overlaid perpendicular to a transmission line results in problematic reflections that disrupt the measurement of analytes within. Thus, methods for the fabrication of devices on thin polyimide films, and mechanically lapped quartz substrates have been discussed, and the integration of a microfluidic chip and terahertz-frequency waveguide was optimised for spectroscopic applications.

Finite element simulations of the final device design were executed, and it was shown that the modelled propagation modes could be used to successfully extract the complex permittivity of a sample measured with the spectrometer. The performance of the technique was then verified by comparison with available data in the microwave and terahertz-frequency range, and quantified by fitting the extracted data to a Debye relaxation model. This device and associated analysis method constitute the first terahertz-frequency on-chip spectrometer that can be used to obtain the frequency-dependent complex permittivity of unknown liquid samples.

Chapter 5

Free-space and On-chip Measurement of Alcohols

In Chapter 4, an on-chip microfluidic terahertz-frequency spectrometer was introduced; the complex permittivity of methanol, ethanol, and propan-1-ol was measured, and found to compare well with published data. However, such verification efforts are restricted by the availability of data in the terahertz-frequency-range. As discussed in Chapter 1, free-space terahertz time-domain spectroscopy is a well-established technique that is often used to measure the dielectric properties of samples in the solid, liquid, and gas phase. Therefore, the measurement of liquid samples with a free-space spectrometer was investigated to allow independent verification of data collected with the on-chip microfluidic device.

The strong attenuation of terahertz-frequency signals in polar liquids necessitates the use of sample containment methods that either allow for reflection of a terahertz beam off the liquid surface, or enable thin films to be probed by transmission of a terahertz field through the sample. Attenuated total reflection [149] and reflection spectroscopy systems [155, 156] can be used to extract the dielectric properties of samples by reflecting terahertz-frequencies from a window–sample interface and modelling the interaction between the evanescent field at the interface and the analyte. Liquid flow-cells are commonly used in transmission experiments, where the sample is sandwiched between two low-loss windows (such as Si [32] or

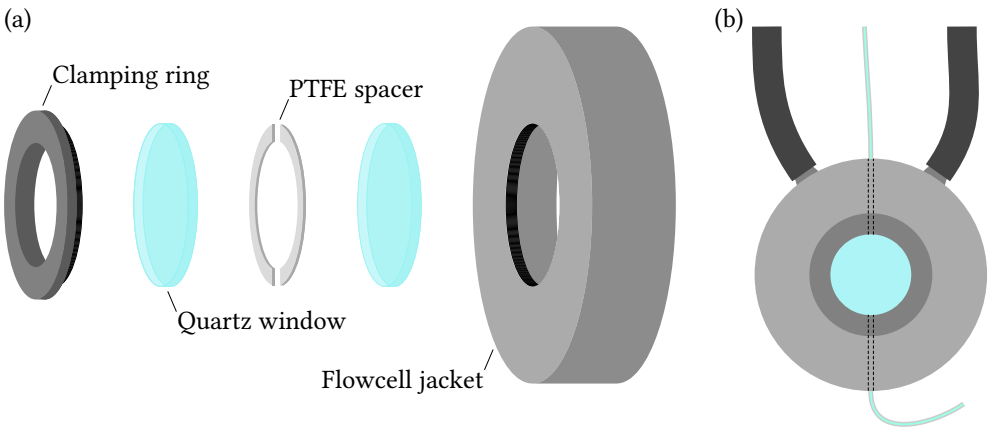

Figure 5.1: (a) An exploded view of the liquid flow-cell that comprised a temperature-controlled jacket within which two 2.18-mm-thick quartz windows, separated by a PTFE spacer, were positioned, and held in place by a threaded ring. (b) Liquid samples were inserted through inlet and outlet holes (dashed) machined in the jacket and aligned with the cavity formed between the windows. The heating jacket was supplied via two hoses on the top of the cell, through which temperature-controlled fluid could be passed to heat or cool samples.

terahertz-transparent plastics [35]) with a separation of a few hundred micrometers, thereby limiting the attenuation introduced by the sample.

In this work, a variable-temperature liquid flow-cell (TFC-M25, Harrick) was used for all free-space liquid measurements. As shown in Figure 5.1a, the cell comprised two 2.18-mm-thick quartz windows separated by a PTFE spacer that were fixed in the flow-cell jacket by a threaded clamping ring. Two inlet and outlet holes, shown in Figure 5.1b, were machined into the flow-cell jacket and aligned with the cavity between the windows, so that liquid samples could be replaced without requiring the cell to be dismantled. Once constructed, the window through the centre of the cell was approximately 25 mm in diameter, which was significantly greater than the focus of the free-space terahertz beam used to probe the sample, thereby reducing the risk of the cell walls interfering with the beam. The temperature of the cell jacket was maintained by flowing water from a temperature-controller (F12-ED, Julabo) through the integrated hoses; a temperature of 20 °C was sustained throughout this work.

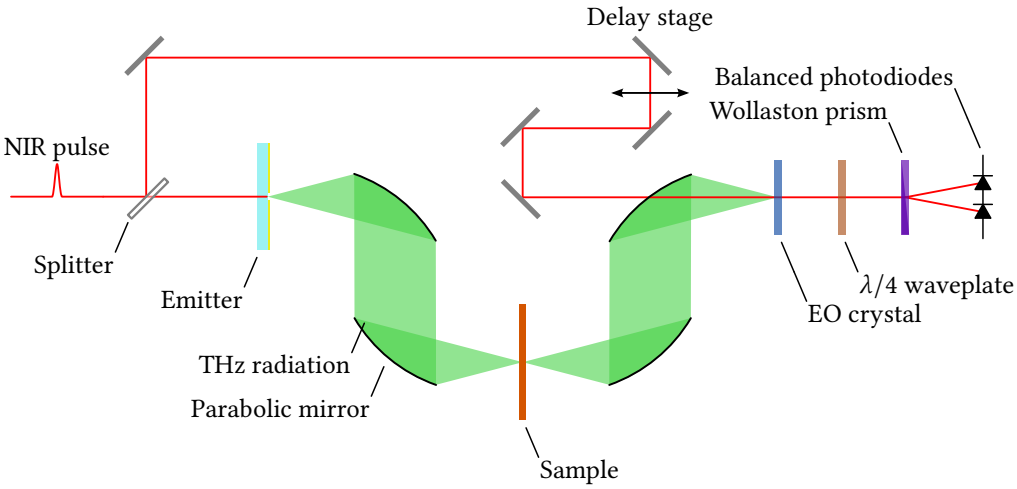

Figure 5.2: A schematic of the free-space terahertz time-domain spectroscopy system. The near-infrared (NIR) input pulse was divided into a pump beam that excites terahertz radiation from the photoconductive antenna, and a probe beam that was used to measure the terahertz-frequency electric field incident on the electro-optic (EO) crystal. Parabolic mirrors were used to first collimate and focus the terahertz field onto the sample, and then collect and focus the radiation onto the EO detection system. The arrival of the probe beam was mechanically delayed with respect to the terahertz pulses; the polarisation of the probing beam was modulated by the terahertz-induced birefringence of the EO crystal, and elliptically polarised by the quarter waveplate. Finally, a Wollaston prism was used to separate the horizontally- and vertically-polarised components of the probe beam, which were measured by a pair of balanced photodiodes.

5.1 The free-space terahertz time-domain spectrometer

The free-space spectroscopy system was constructed adjacent to the microfluidic spectrometer, such that both systems were excited by the same ~100 fs near-infrared source. Owing to the significant attenuation of terahertz-frequency signals by the water vapour content of untreated air, the free-space spectrometer was situated in a sealed box that could be purged with N_2 or dry air. As shown in Figure 5.2, a 10 % beam splitter was used to divide the input near-infrared beam (with an average power of 700 mW) into a 630 mW pump beam, and a 70 mW probe. Terahertz pulses were generated from a photoconductive switch patterned on a 350-µm-thick quartz substrate [157] by focusing the pump beam onto the LT GaAs in the 100-µm-wide gap formed between two Ti:Au electrodes, across which a 350 V bias was applied. The photoconductive antenna bias was electrically chopped at 7 kHz to allow synchronisation with a lock-in amplifier. The generated terahertz field was focused onto the sample space with a pair of parabolic mirrors, and similarly collected with

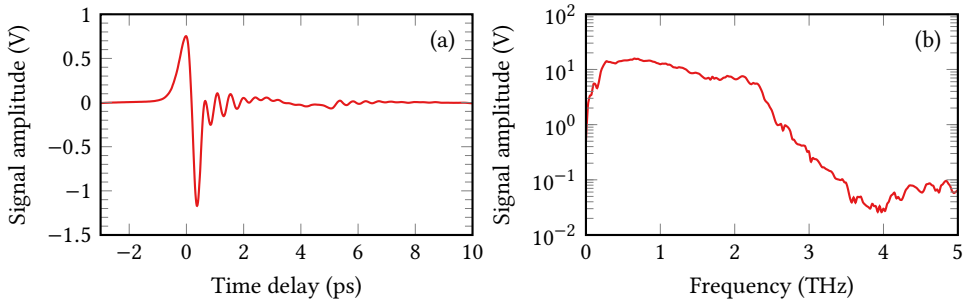

Figure 5.3: (a) The time-domain response recorded at the balanced photodiodes as the arrival of the probe pulse was delayed with respect to the terahertz pulses incident on the electro-optic crystal. (b) The Fourier transform of the data in (a).

a second pair of mirrors, and then focused onto the 2-mm-thick ZnTe electro-optic crystal.

A linear stage was used to mechanically delay the arrival of the probe beam with respect to the pulsed terahertz electric field, after which the detection beam was focused through a hole in the final parabolic mirror such that it was coincident with the focused terahertz pulses on the surface of the electro-optic crystal. The birefringence of the crystal was modulated by the focused terahertz field, such that the polarisation angle of the probe beam varied in proportion with the local field amplitude. A quarter waveplate was used to elliptically polarise the probe beam, which was then divided into horizontally- and vertically-polarised components by a Wollaston prism. The relative amplitude of the perpendicular components was measured using a pair of balanced photodiodes (Nirvana, Newport), and their difference was recorded with a lock-in amplifier (Signal Recovery 7265). Figure 5.3a shows the output of the balanced photodiodes when the purge box was filled with dry air without a sample in the beam path, and the relative delay introduced by the linear stage was increased from −2 ps to +10 ps. In practice, the stage position was varied from −15 ps to +45 ps, but a cropped window is shown here for clarity. As shown in Figure 5.3b, there was little variation in the amplitude of the frequency response of the free-space spectrometer between 0.3 THz and 2 THz, and a significant decrease in amplitude above 2 THz. This is in contrast with the on-chip devices considered in Chapters 3 and 4, where the signal amplitude decreased with frequency across the measured spectrum.

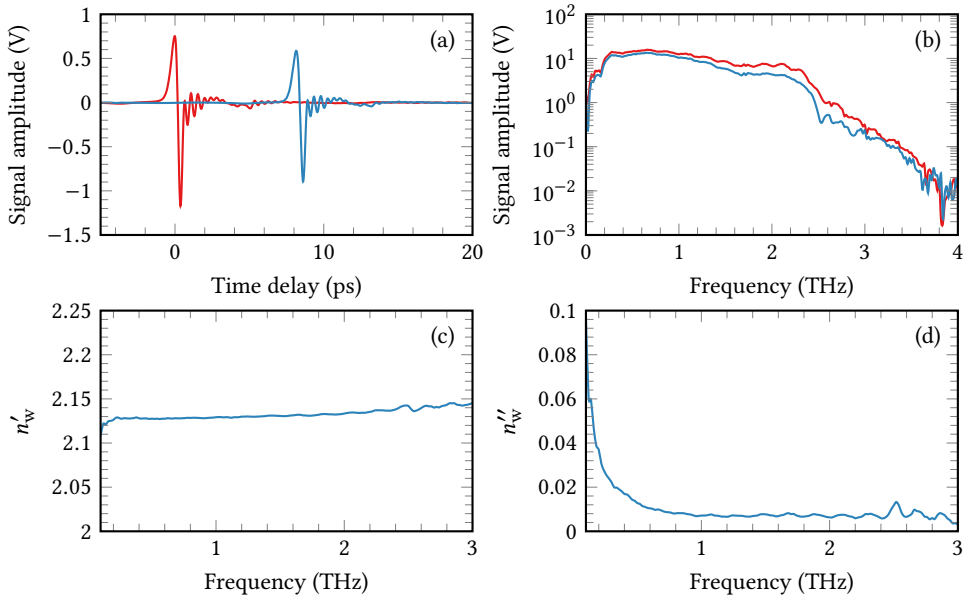

Figure 5.4: (a) Picosecond pulses recorded using the free-space spectrometer when an empty (windowless) flow-cell was placed in the beam path (red), and when a 2.18-mm-thick z-cut quartz window was fitted in the cell (blue). (b) The amplitude of the Fourier transforms of the data shown in (a). (c) The real and (d) imaginary components of the refractive index of the quartz window.

5.1.1 Refractive index calculation of single-layer samples

The propagation model used to calculate the complex permittivity of samples held within a liquid flow-cell positioned in the focus of the terahertz beam is discussed in §5.2. In order to implement this model, the complex refractive index of the window material, $\tilde{n}_w$, must be known. The index of a 2.18-mm-thick, d, z-cut quartz window was measured by first recording a reference, $E_r(t)$, of the empty flow-cell with the windows removed (such that the terahertz beam path was unobstructed), and then fitting a single window into the cell (such that the quartz window was in the focus of the terahertz beam), and measuring the response, $E_w(t)$. The time-domain responses, as shown in Figure 5.4a, were transformed into the frequency domain, as shown in Figure 5.4b, and the amplitude, $A(\omega)$, and phase, $\varphi(\omega)$, ratios were calculated. The real component of the refractive index of the quartz window was calculated as described by Jepsen [158],

$$n'_w = 1 + \frac{c}{\omega d}\varphi, \tag{5.1}$$

and the absorption coefficient was also determined [158],

$$\alpha = -\frac{2}{d}\ln\left(A\frac{n'_{\mathrm{w}}+1}{4n'_{\mathrm{w}}}\right), \tag{5.2}$$

from which the imaginary component of the refractive index was calculated using Equation 4.6, as shown in Figure 5.4c and d. The refractive index of both windows was measured in this manner, and their indices were found to be indistinguishable. Therefore, the data in Figure 5.4 was used to represent both windows in further calculations.

5.2 Calculation of sample parameters

In the previous section, a relatively simple method was used to determine the dielectric properties of samples placed in the path of a terahertz beam. However, this approach is only valid when a single, homogeneous sample is measured. The measurement of multi-layered structures, such as the liquid flow-cell, introduces a number of abrupt changes in the propagation medium permittivity, so that terahertz pulses are partially reflected at each interface. The source of some of these reflections are identified in Figure 5.5, which shows the time-domain response of both an unobstructed terahertz beam, and the response when the cell was fitted with two windows separated by a 270-µm-thick spacer, and positioned in the beam focus; the initial terahertz pulse of each measurement has been aligned at 0 ps to ease comparison of the responses. The most significant difference between the two responses is observed around 30 ps, owing to the reflection of the terahertz pulse within a single 2.18-mm-thick quartz window (a total propagation distance of 4.36 mm through a medium with index $n' = 2.12$ equates to a delay of 30.8 ps). The reflection observed after 42 ps was present in both measurements, and is a result of the initial pulse reflected from the back surface of the 2-mm-thick ZnTe crystal, which is then sampled for a second time (a total distance of 4 mm through a medium with index $n' = 3.16$ [159] is equivalent to a delay of 42.2 ps). The final feature present in the cell-loaded response occurred after approximately 61.6 ps and is the result of two reflections within the quartz windows. Ordinarily, system reflections such as these

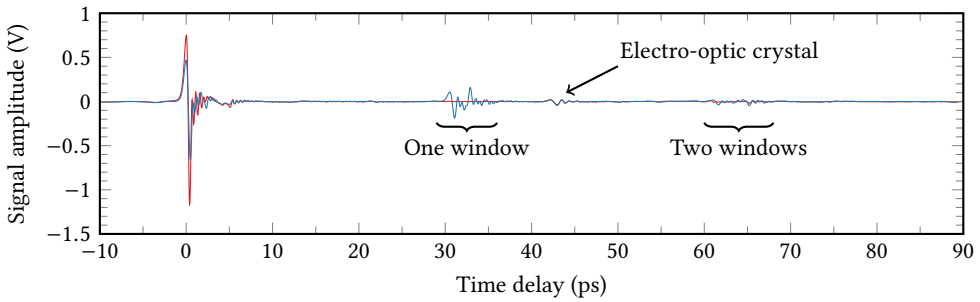

Figure 5.5: The time-domain response of the free-space spectrometer measured with an unobstructed beam path (red), and when a flow-cell fitted with two 2.18-mm-thick quartz windows, separated by a 270-µm-thick spacer was positioned in the beam focus (blue). The initial pulses of each trace have been aligned at 0 ps to ease comparison, and reflections owing to the quartz windows and electro-optic crystal are indicated.

would be cropped from a measured response to simplify further analysis. However, owing to the close proximity of the quartz windows, a Fabry–Pérot cavity is formed between the two windows, which results in a reflection that is incorporated within the initial terahertz pulse, and is difficult to distinguish by eye from the responses shown in Figure 5.5; the 540 µm propagation distance per cavity oscillation results in an additional reflection every 1.8 ps that cannot be easily windowed out of the time-domain response. Therefore, extraction of the the complex permittivity of a sample inserted into the flow-cell required that either the source of these system reflections was physically removed, or an analytical model was used to account for them.

When designing the on-chip spectrometer, it was possible to define the device structure such that mismatched interfaces were removed from the sensitive regions of the transmission line. While the fabrication techniques developed in Chapter 4 could be used to integrate photoconductive switches directly into the windows of a liquid flow-cell (with the aim of removing any sample–window interfaces in the beam path) such a development is outside the scope of this work. Here, a propagation model will be implemented in order to analytically isolate the complex permittivity of a liquid sample from the measured response of the flow-cell in which it is contained.

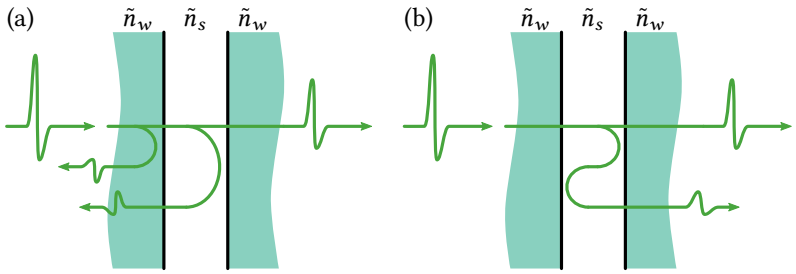

Figure 5.6: (a) An incoming pulse is reflected at the interface between regions of differing $\tilde{n}$, first at the transition from window to sample, then at the transition from sample to window. The total reflective loss is described by the Fresnel transmission coefficient. (b) A Fabry–Pérot etalon is formed by two planar parallel surfaces. A pulse is reflected multiple times within the cavity, such that the x^{th} reflection in the time-domain has completed $2x+1$ passes through the sample.

5.2.1 The flow-cell propagation model

In the most simple case, a terahertz-frequency signal, $E_0(\omega)$, is attenuated by the propagation coefficient of the medium in which the wave is travelling, $P(\omega)$, such that after a distance d, the signal amplitude is [160]

$$E(\omega) = E_0(\omega) \cdot P(\omega, d), \tag{5.3}$$

where

$$P_x(\omega, d) = e^{-\mathrm{j}\tilde{n}_x k_0 d}, \tag{5.4}$$

in which $\tilde{n}_x$ is the complex index of the propagation medium, and k_0 is the free-space wavenumber. If a measurement of free-space ($\tilde{n} = 1 - \mathrm{j}0$) is used as a reference, and all reflection effects are ignored, the ratio of the sample-loaded ($x = s$) and reference ($x = r$) fields, E_s and E_r respectively, is

$$\frac{E_\mathrm{s}(\omega)}{E_\mathrm{r}(\omega)} = e^{-\mathrm{j}k_0 d(\tilde{n}_\mathrm{s}-1)}. \tag{5.5}$$

In practice, the terahertz field is typically generated at a photoconductive switch that is some distance from the sample. Therefore, the propagating pulse is not only attenuated and dispersed by the complex refractive index of the sample, but is also partially reflected by the index discontinuities at each material interface, as illustrated in Figure 5.6a. The Fresnel transmission coefficient, t_{pq}, describes the attenuation of

a signal as it is reflected at the interface between materials p and q as follows,

$$t_{pq} = \frac{2\tilde{n}_p}{\tilde{n}_p + \tilde{n}_q}. \tag{5.6}$$

Reflections are produced at each interface between the air, windows, and sample in the flow-cell structure. Therefore, the reference measurement of an empty (air-filled) cell includes transmission across four material interfaces, which give a total Fresnel transmission coefficient of

$$T_\mathrm{r} = t_\mathrm{aw} t_\mathrm{wa} t_\mathrm{aw} t_\mathrm{wa}, \tag{5.7}$$

where the subscripts a and w denote the air and windows respectively, such that t_aw represents a pulse propagating from the air into a window. Similarly, when a sample is loaded into the cavity, the total Fresnel transmission coefficient is

$$T_\mathrm{s} = t_\mathrm{aw} t_\mathrm{ws} t_\mathrm{sw} t_\mathrm{wa}, \tag{5.8}$$

where the subscript s denotes the sample. The ratio of the sample and reference Fresnel transmission coefficients gives the frequency-dependent reflection losses [2],

$$\frac{T_\mathrm{s}}{T_\mathrm{r}} = \frac{t_\mathrm{ws} t_\mathrm{sw}}{t_\mathrm{wa} t_\mathrm{aw}} = \frac{\tilde{n}_\mathrm{s} \left(\tilde{n}_\mathrm{w} + 1\right)^2}{\left(\tilde{n}_\mathrm{s} + \tilde{n}_\mathrm{w}\right)^2}. \tag{5.9}$$

As illustrated in Figure 5.6b, the Fabry–Pérot etalons formed by the plane–parallel windows and sample produce time-domain reflections that have completed multiple-passes through each component. Typically, the cell windows were an order of magnitude thicker than the spacer material, and therefore the majority of the oscillations originate in the cavity between them. A pulse oscillating in the cavity is reflected by each window, and attenuated by the sample. The Fabry–Pérot term is therefore the infinite sum of these oscillations [31],

$$FP_\mathrm{s}(\omega) = \sum_{m=0}^{\infty} \left(r_\mathrm{sw} \cdot P_\mathrm{s}^2(\omega, d) \cdot r_\mathrm{sw}\right)^m = \frac{1}{1 - r_\mathrm{sw}^2 P_\mathrm{s}^2(\omega, d)}, \tag{5.10}$$

where r_{sw} is the Fresnel reflection coefficient of the sample–window interface,

$$r_{\mathrm{sw}} = \frac{\tilde{n}_{\mathrm{s}} - \tilde{n}_{\mathrm{w}}}{\tilde{n}_{\mathrm{s}} + \tilde{n}_{\mathrm{w}}}. \tag{5.11}$$

It follows that the full expression for transmission through the flow-cell structure is the ratio of the fields when the propagation coefficient, Fresnel transmission coefficient, and Fabry-Pérot etalons are considered [32],

$$\frac{E_{\mathrm{s}}(\omega)}{E_{\mathrm{r}}(\omega)} = \frac{E_0(\omega) \cdot P_{\mathrm{s}}(\omega, d) \cdot T_{\mathrm{s}}(\omega) \cdot FP_{\mathrm{s}}(\omega)}{E_0(\omega) \cdot P_{\mathrm{r}}(\omega, d) \cdot T_{\mathrm{r}}(\omega) \cdot FP_{\mathrm{r}}(\omega)}. \tag{5.12}$$

When substituted, it is clear that the function in Equation 5.12 is dependent on $\tilde{n}_{\mathrm{w}}$, $\tilde{n}_{\mathrm{s}}$, and d,

$$\frac{E_{\mathrm{s}}(\omega)}{E_{\mathrm{r}}(\omega)} = e^{-\mathrm{j}k_0 d(\tilde{n}_{\mathrm{s}}-1)} \cdot \frac{\tilde{n}_{\mathrm{s}} \left(\tilde{n}_{\mathrm{w}} + 1\right)^2}{\left(\tilde{n}_{\mathrm{s}} + \tilde{n}_{\mathrm{w}}\right)^2} \cdot \frac{1 - \left(\frac{1-\tilde{n}_{\mathrm{w}}}{1+\tilde{n}_{\mathrm{w}}}\right)^2 e^{-2\mathrm{j}k_0 d}}{1 - \left(\frac{\tilde{n}_{\mathrm{s}}-\tilde{n}_{\mathrm{w}}}{\tilde{n}_{\mathrm{s}}+\tilde{n}_{\mathrm{w}}}\right)^2 e^{-2\mathrm{j}\tilde{n}_{\mathrm{s}} k_0 d}}. \tag{5.13}$$

The complex refractive index of the z-cut quartz windows was measured in §5.1, and was assumed to be invariant between measurements. The sample thickness, d, was determined by the thickness of the spacer material used in the flow-cell, and therefore $\tilde{n}_{\mathrm{s}}$ is the only unknown in Equation 5.13, which was solved by first approximating $\tilde{n}_{\mathrm{s}}$ with Equations 5.1 and 5.2, and then using a Levenberg–Marquardt [154] nonlinear least-squares minimisation algorithm to reduce the residual between the measured ratio $E_{\mathrm{s}}(\omega)/E_{\mathrm{r}}(\omega)$ and the model output.

The spacer thickness could only be directly measured prior to construction of the flow-cell. Therefore, a degree of error was introduced by the force applied when the clamping ring was tightened by hand, leading to variation in the cavity length, d, owing to compression of the spacer material. For example, Figure 5.7a and b shows the complex refractive index of propan-2-ol calculated using the propagation model method as the estimated sample thickness was varied between ±20 % of the 210 µm value that was measured. It is clear that a thickness error of a few percent corresponds to a relatively large change in the value of $\tilde{n}_s$ that is extracted, and introduces an oscillatory component (a result of an incorrect thickness applied to

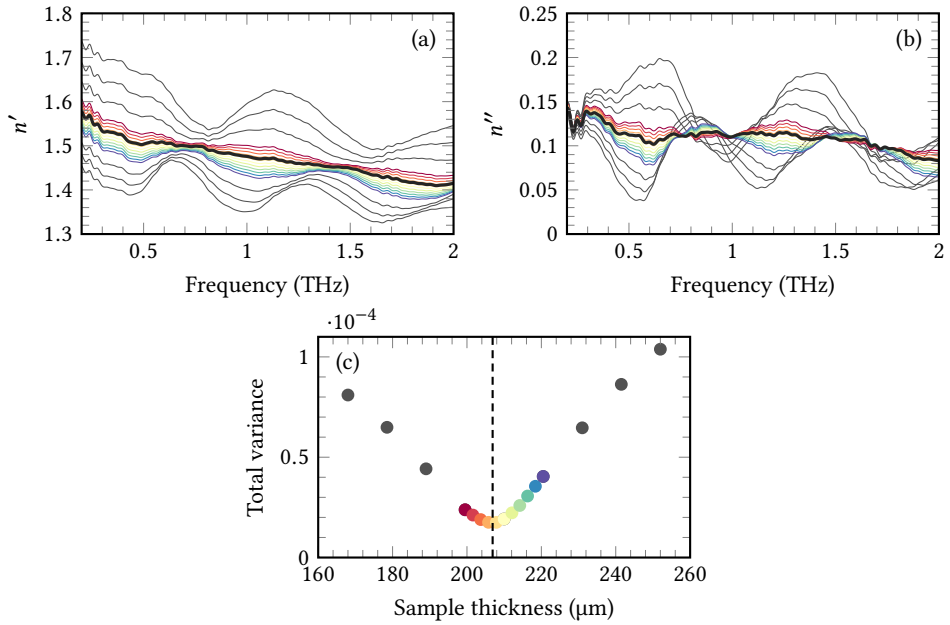

Figure 5.7: The (a) real and (b) imaginary components of the refractive index of propan-2-ol measured using the flow-cell propagation model as the estimated spacer thickness was varied from −20 % to +20 % of the measured value, in 5 % increments (grey). The total variance (c) was calculated for each coarse step, and a higher resolution sweep of thickness was conducted between −5 % (red) and +5 % (violet) of the coarse total variance minimum. The sample thickness, and corresponding refractive index, was determined by identification of the minimum total variance (black).

the Fabry-Pérot term). The real and imaginary components of liquid samples are not expected to exhibit sharp spectral features, hence little change is expected between adjacent frequency points [30]. This property can be exploited to allow the sample thickness to be determined *in situ*, through calculation of the total variance as a function of modelled thickness.

The total variance of a measurement, TV, is the sum of the difference between the real and imaginary components of the refractive index calculated at each frequency point [30],

$$TV = \sum_{i=1}^{m-1} \left(\left| n'_i - n'_{i-1} \right| + \left| n''_i - n''_{i-1} \right| \right), \tag{5.14}$$

where m is the number of data points over which the total variance is calculated. As shown in Figure 5.7c, the total variance was calculated as the sample thickness estimate, d, was varied from −20 % to +20 % of the spacer thickness measured prior to construction of the flow-cell. As the minimisation process by which Equation 5.13 is solved can be time-consuming, the spacer thickness was first incremented by 5 %

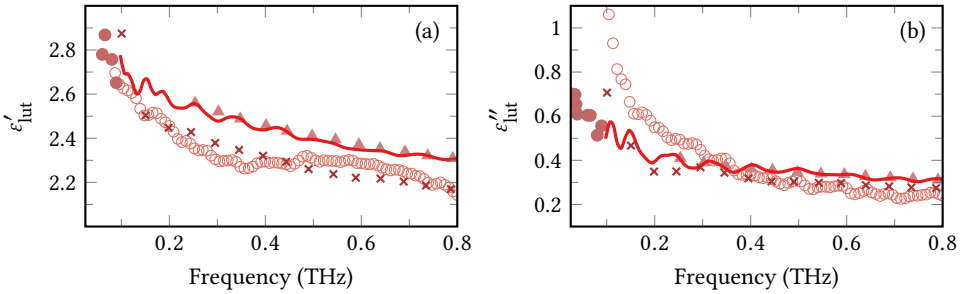

Figure 5.8: The (a) real and (b) imaginary components of the permittivity of propan-1-ol as measured using the flow-cell in the free-space spectrometer (solid), and the on-chip microfluidic spectrometer (○). Also shown are data published by Barthel et al. [82] (●), Kindt and Schmuttenmaer [35] (×), and Yomogida et al. [148] (▲).

in a coarse pass, and the thickness that produced the smallest total variance was identified. A second fine pass was then executed in which the sample thickness was incremented by 1 % between −5 % and +5 % of the thickness identified in the coarse pass. A peak finding algorithm was then used to identify the sample thickness that produced the smallest total variance, and the sample complex refractive index was calculated for this value. In this example, the spacer was measured to be 210-µm-thick prior to construction of the cell, and a thickness of 206.9 µm was extracted using the method described, which is a difference of 1.5 %.

5.3 Comparison with on-chip data

The flow-cell was constructed with a 270-µm-thick spacer between the windows, and an automated syringe pump was connected to the liquid inlet to allow control over sample flow. Samples were loaded into the cell by first inserting 3 mL of the analyte at a rate of 15 µL s^{-1} to fill the system with the liquid-under-test, without inducing an overpressure that could cause displacement of the cell windows. After a measurement was complete, the system was purged of the sample with 3 mL of propan-2-ol, and approximately 10 mL of dry air, which served to flush out the propan-2-ol, and evaporate any residual solvent.

A sample of propan-1-ol was first loaded into the cell, and the complex permittivity calculated using the method described in §5.2.1, as shown in Figure 5.8. Also plotted are the published data discussed in Chapter 4, with which a good agreement

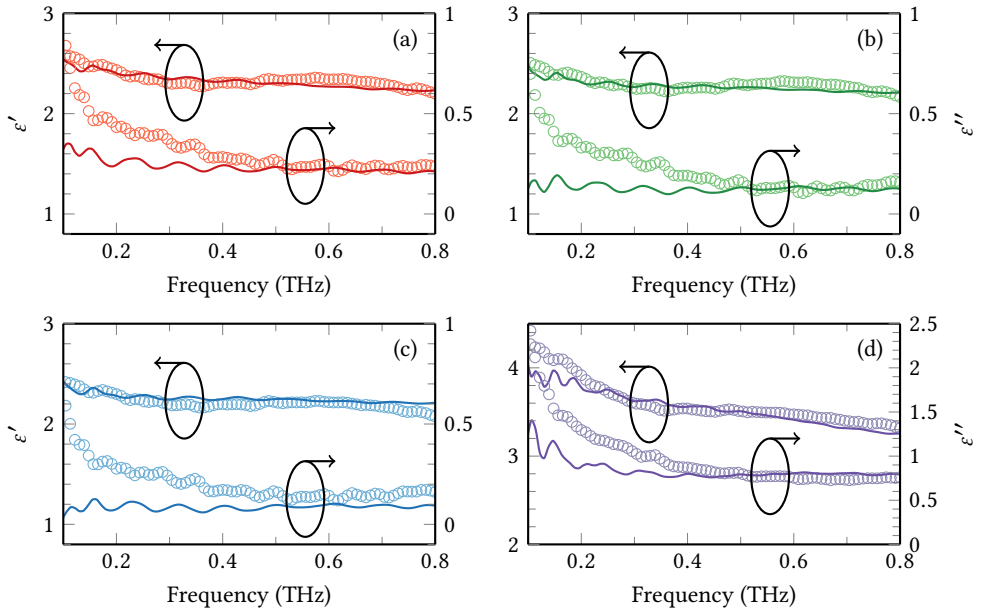

Figure 5.9: The complex permittivity of (a) butan-1-ol, (b) hexan-1-ol, (c) octan-1-ol, and (d) ethan-1,2-diol as measured using the on-chip microfluidic spectrometer (○), and the free-space time-domain spectroscopy system (solid). In all plots, the left and right y-axes represent the real and imaginary components respectively.

is observed; the complex permittivity of methanol and ethanol was also measured, and a similar agreement was found. Methanol, ethanol, and propan-1-ol form part of the monohydric alcohol series, where the prefix indicates the number of carbon atoms in the molecule (meth = 1, eth = 2, prop = 3). The dielectric properties of these samples have been well-studied in the literature, however measurements of higher order alcohols such as butan-1-ol, hexan-1-ol, and octan-1-ol are not readily available. As shown in Figure 5.9, both the on-chip and free-space spectrometer were used to measure the complex permittivity of the higher order monohydric alcohols, and a sample of ethan-1,2-diol. An excellent agreement was observed between the datasets above 0.3 THz, however the extracted imaginary components diverged at lower frequencies. Both the free-space and on-chip spectrometers are restricted by measurement uncertainty at these frequencies. As shown in Figure 5.4b, the dynamic range of the free-space spectrometer is greatest between 0.3 THz and 2 THz, and decreases sharply below 0.3 THz, therefore any measurement below this frequency will be more susceptible to system noise. Additionally, the sensitivity of the interaction between the field and sample is further reduced, as the 270-µm-thick sample is considerably thinner than the wavelength of the <200 GHz probing field, which is

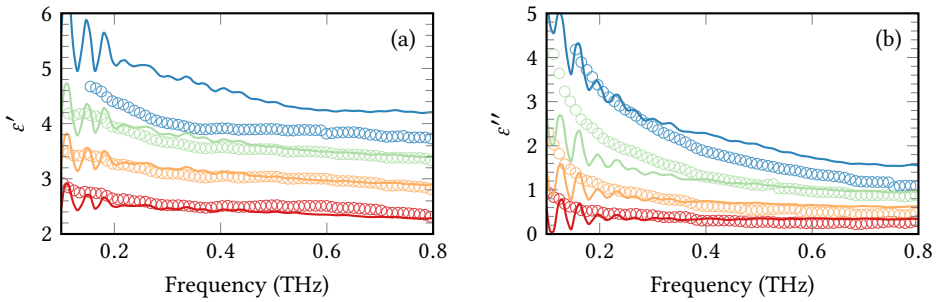

Figure 5.10: The (a) real and (b) imaginary permittivity components of DI-H_2O:propan-2-ol solutions with volume mixing ratios from 0 % (red) to 75 % (blue) in 25 % increments.

of order 1 mm in a sample such as ethan-1,2-diol. Although techniques have been developed to improve accuracy when measuring sub-wavelength samples, their efficacy is yet to be demonstrated below 500 GHz, or with multi-layered structures [161]. Similarly, the sensitivity of the on-chip microfluidic spectrometer is limited by the extent of the evanescent field at the low-frequency end of its sensitive bandwidth. The interaction between the propagating field and structural components such as the quartz substrate or PDMS channel boundary increases with the extent of field. Therefore, any error owing to inaccuracies in the modelled complex permittivity of these components increases as a function of wavelength.

5.3.1 High-permittivity limit of on-chip measurements

As discussed in §3.3.3, additional dielectric slab propagation modes are supported when a planar Goubau line is patterned on a thick, or high permittivity substrate. Similarly, the introduction of a high permittivity superstrate can result in the generation of additional modes that cause a failure of the technique used to extract the sample permittivity from on-chip spectrometer measurements. To illustrate this limitation, mixtures of DI-H_2O and propan-2-ol were prepared in volume ratios from 0 % to 100 % in increments of 25 %, and measured on both systems. Given that the permittivity of DI-H_2O is considerably greater than that of propan-2-ol, the permittivity of the solutions increased as a function of the DI-H_2O ratio, as shown in Figure 5.10. A good agreement was observed between the two systems when the DI-H_2O ratio was less than 50 %; very different values were extracted at 75 %, and the on-chip device extraction algorithm failed to find a solution when a 100 % DI-H_2O sample was mea-

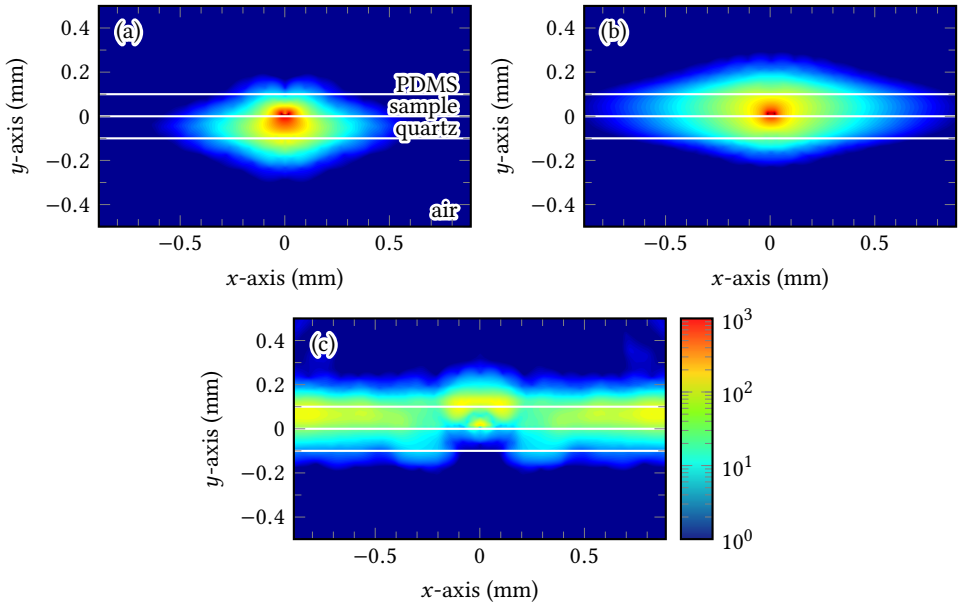

Figure 5.11: The simulated cross-sectional distribution of an 800 GHz field about the 30-µm-wide planar Goubau line of the on-chip spectrometer when the permittivity of the overlaid sample material was (a) $\varepsilon' = 1$, (b) $\varepsilon' = 4$, and (c) $\varepsilon' = 5.5$. As the permittivity of the sample was increased from 1 to 4, the field distribution within the sample increased also. Increasing the permittivity to 5.5 allowed a more complex superstrate slab mode to be supported, preventing accurate extraction of the sample permittivity. The absolute values of electric field are arbitrary, but the same logarithmic colour scale has been applied to each figure.

sured. The source of this limitation is revealed by considering the field distribution about the planar Goubau line as the sample permittivity is increased. Figure 5.11a shows the cross-sectional distribution of an 800 GHz field supported by the planar Goubau line for a sample with permittivity $\tilde{\varepsilon} = 1 - \mathrm{j}0$, which follows the expected radial pattern. A similar distribution is demonstrated in Figure 5.11b, where the sample permittivity was increased to $\tilde{\varepsilon} = 4 - \mathrm{j}0$, and the field tends increasingly into the sample. As the sample permittivity is increased further, a slab-like mode is preferred. Figure 5.11c shows the slab-like mode that was preferred when the sample permittivity was increased to $\tilde{\varepsilon} = 5.5 - \mathrm{j}0$. In this more complex propagation mode, the field is no longer guided by the transmission line, and cannot therefore be accurately measured by detection at the integrated photoconductive switches. The cut-off frequency of this slab mode could be increased by reducing the depth of the microfluidic channel, however doing so would reduce the sensitivity of the device to lower permittivity samples, owing to the reduction in interaction volume between the field and analyte.

5.4 Concluding remarks

The measurement of liquid samples using a free-space terahertz time-domain spectroscopy system has been investigated. As the analytes were contained within a liquid flow-cell, a multi-layer propagation model was implemented that included the Fresnel and Fabry–Pérot reflections, thereby enabling extraction of the sample permittivity from a measurement of the entire cell. The output of the free-space spectrometer was first verified by measuring the complex permittivity of the well-studied monohydric alcohols studied in Chapter 4, and then comparing the results to several published datasets, and those recorded with the on-chip spectrometer. Samples of butan-1-ol, hexan-1-ol, octan-1-ol, and ethan-1,2-diol were then measured using both the free-space and on-chip systems, and a good agreement was found between the output of the two systems. Finally, the high-permittivity limit of the on-chip device was investigated by systematically diluting propan-1-ol with DI-H_2O such that the permittivity of the sample solution was increased. For the 100-µm-deep channel measured here, a maximum sample permittivity of 4 was identified. The permittivity measurable with an on-chip microfluidic device could be increased further by reducing the height of the channel, but this would in turn reduce the sensitivity. Therefore, the device geometry should be selected to be appropriate for the expected sample permittivity range.

Chapter 6

Conclusions and Future Work

The work presented in this thesis has demonstrated the integration of a planar Goubau transmission line and microfluidic circuit in order to create the first on-chip microfluidic terahertz-frequency spectrometer that can be used to measure the complex dielectric properties of liquids. This critical development paves the way for the miniaturisation of terahertz-sensors, and their integration with larger systems. In the course of this work, a range of device geometries were investigated, and several important observations made that allowed simplification of the device geometry, so that it could be accurately modelled. The numerical method introduced allows extraction of sample parameters such as permittivity, refractive index, and absorption, and is by no means limited to the analysis of liquids, as it can be easily adapted for the measurement of samples in the solid or gas phase.

The processes involved in the fabrication of these devices have been detailed, and several modifications were made to pre-existing techniques to improve device yield and quality. Given that spectroscopic applications rely on a high signal-to-noise ratio, the efficient generation and detection of terahertz radiation using these devices was investigated, and it was argued that switch bias, beam polarisation, and switch geometry play an important role. It was also shown that careful design of the waveguide geometry is required to avoid the generation of unwanted reflections and propagation modes that may complicate further analysis of the device, and potentially prevent accurate measurement of sample properties. Specifically, the use of waveguide meanders to allow changes in transmission line direction without

generating reflections was discussed, and the support of substrate modes in thick and high-permittivity substrates was explored through device simulation.

The integration of microfluidic channels and on-chip waveguides presented some interesting challenges as fabrication techniques were developed that allowed intimate interaction between the liquid analyte and propagating electric field, without compromising the electronics required to generate and detect terahertz pulses. It was shown that microfluidic channels must be bonded in a manner that avoids the generation of unwanted reflections, so that the device can be more easily modelled, and a device was designed that allowed tens of millimetres of signal propagation before the first significant reflections were detected, thereby allowing a relatively high frequency resolution to be achieved. A numerical method was introduced that relied on the prior simulation of a range of proxy samples placed within an accurate model of the device geometry and interpolation of these results to determine the dielectric properties of an unknown measured sample. The data recorded using this device and analysis technique were compared to those available in literature from a wide range of terahertz-frequency spectrometers, and a satisfactory agreement was found between the methods.

Finally, a wider range of samples were investigated with the on-chip spectrometer developed in this work, and the results were verified with data recorded using a free-space terahertz time-domain spectroscopy system that was equipped with a liquid flow-cell. Again, a satisfactory agreement was found between the datasets, and some limitations of the on-chip device were identified. It was shown that for a given device geometry, there is an upper limit to the permittivity that can be measured without the generation of additional propagation modes that result in a break-down of the numerical analysis technique.

Overall, the work presented in this thesis marks significant progress in the development of compact terahertz-frequency analytical tools, and it is hoped that the work discussed here will lay the foundation for future developments. Arguably, the most significant area of interest is the study of active biological systems that are particularly difficult to examine in traditional free-space systems. Recent developments in organ-on-a-chip technologies make it increasingly possible to establish a sus-

tained artificial *in vivo* environment that could be readily integrated with terahertz-frequency sensors, which have been shown to be of value in the investigation of hydration, molecular dynamics, and protein function. It has been shown that temperature control is critical when investigating biological function, and it may therefore be necessary to develop methods by which a heating element and thermocouple can be integrated with the on-chip device in order to monitor and control the environment within the microfluidic system. To achieve such a goal, several improvements may need to be made to the technology described here, in order to attract the wider attention of biochemists. As discussed, temperature is a key environmental variable in biological experiments, however the temperature local to the photoconductive switch is unknown, and is difficult to measure. Given that a 10 mW infrared beam is focused into a micrometre-scale area, a high temperature is expected, and therefore it may be necessary to develop a geometry in which the sample is separated from the switching regions, perhaps by increasing the switch separation, however this would increase signal attenuation. The bio-compatibility of the device may also require improvement, as it is known that some biological species can be absorbed by PDMS. While this phenomenon can be of use in the definition of semi-permeable membranes, filters, and on-chip pumping systems, it may be necessary to explore surface treatments, or alternative materials. The method of analysis developed in this work could be transferred to a wide range of device geometries and materials, and may therefore be a valuable tool in the next generation of on-chip microfluidic technologies.

Bibliography

[1] A. G. Davies, A. D. Burnett, W. Fan, E. H. Linfield, and J. E. Cunningham, "Terahertz spectroscopy of explosives and drugs," *Materials Today*, vol. 11, no. 3, pp. 18–26, 2008.

[2] A. G. Markelz, "Terahertz dielectric sensitivity to biomolecular structure and function," *IEEE Journal of Selected Topics in Quantum Electronics*, vol. 14, no. 1, pp. 180–190, 2008.

[3] P. F. Taday, "Applications of terahertz spectroscopy to pharmaceutical sciences," *Philosophical Transactions of the Royal Society of London A: Mathematical, Physical and Engineering Sciences*, vol. 362, no. 1815, pp. 351–364, 2004.

[4] W. H. Fan, A. Burnett, P. C. Upadhya, J. Cunningham, E. H. Linfield, and A. G. Davies, "Far-infrared spectroscopic characterization of explosives for security applications using broadband terahertz time-domain spectroscopy," *Applied Spectroscopy*, vol. 61, no. 6, pp. 638–643, 2007.

[5] P. Taday, I. Bradley, D. Arnone, and M. Pepper, "Using terahertz pulse spectroscopy to study the crystalline structure of a drug: a case study of the polymorphs of ranitidine hydrochloride," *Journal of Pharmaceutical Sciences*, vol. 92, no. 4, pp. 831–838, 2003.

[6] M. Walther, B. M. Fischer, and P. U. Jepsen, "Noncovalent intermolecular forces in polycrystalline and amorphous saccharides in the far infrared," *Chemical Physics*, vol. 288, no. 2, pp. 261–268, 2003.

[7] T. Ohkubo, M. Onuma, J. Kitagawa, and Y. Kadoya, "Micro-strip-line-based sensing chips for characterization of polar liquids in terahertz regime," *Applied Physics Letters*, vol. 88, no. 21, p. 212511, 2006.

[8] Thomson Reuters, *Web of Science*, https://apps.webofknowledge.com/, Online; accessed 2017-04-22.

[9] M. van Exter, C. H. Fattinger, and D. Grischkowsky, "Terahertz time-domain spectroscopy of water vapor," *Optics Letters*, vol. 14, no. 20, pp. 1128–1130, 1989.

[10] R. Köhler, A. Tredicucci, F. Beltram, H. E. Beere, E. H. Linfield, A. G. Davies, D. A. Ritchie, R. C. Iotti, and F. Rossi, "Terahertz semiconductor-heterostructure laser," *Nature*, vol. 417, no. 6885, pp. 156–159, 2002.

[11] R. A. Lewis, "A review of terahertz sources," *Journal of Physics D: Applied Physics*, vol. 47, no. 37, 374001, 2014.

[12] Z. Piao, M. Tani, and K. Sakai, "Carrier dynamics and terahertz radiation in photoconductive antennas," *Japanese Journal of Applied Physics*, vol. 39, no. 1, pp. 96–100, 2000.

[13] D. Auston, K. Cheung, and P. Smith, "Picosecond photoconducting hertzian dipoles," *Applied Physics Letters*, vol. 45, no. 3, pp. 284–286, 1984.

[14] S. Gupta, J. F. Whitaker, and G. A. Mourou, "Ultrafast carrier dynamics in III-V semiconductors grown by molecular-beam epitaxy at very low substrate temperatures," *IEEE Journal of Quantum Electronics*, vol. 28, no. 10, pp. 2464–2472, 1992.

[15] F. Doany, D. Grischkowsky, and C.-C. Chi, "Carrier lifetime versus ion-implantation dose in silicon on sapphire," *Applied Physics Letters*, vol. 50, no. 8, pp. 460–462, 1987.

[16] P. U. Jepsen, R. H. Jacobsen, and S. Keiding, "Generation and detection of terahertz pulses from biased semiconductor antennas," *Journal of the Optical Society of America B*, vol. 13, no. 11, pp. 2424–2436, 1996.

[17] J. Neave, B. Joyce, P. Dobson, and N. Norton, "Dynamics of film growth of GaAs by MBE from RHEED observations," *Applied Physics A*, vol. 31, no. 1, pp. 1–8, 1983.

[18] M. Kaminska, Z. Liliental-Weber, E. Weber, T. George, J. Kortright, F. Smith, B.-Y. Tsaur, and A. Calawa, "Structural properties of As-rich GaAs grown by molecular beam epitaxy at low temperatures," *Applied Physics Letters*, vol. 54, no. 19, pp. 1881–1883, 1989.

[19] I. S. Gregory, C. Baker, W. Tribe, M. Evans, H. E. Beere, E. H. Linfield, A. Davies, and M. Missous, "High resistivity annealed low-temperature GaAs with 100 fs lifetimes," *Applied Physics Letters*, vol. 83, no. 20, pp. 4199–4201, 2003.

[20] E. Yablonovitch, T. Gmitter, J. Harbison, and R. Bhat, "Extreme selectivity in the lift-off of epitaxial GaAs films," *Applied Physics Letters*, vol. 51, no. 26, pp. 2222–2224, 1987.

[21] J. Cunningham, C. Wood, A. G. Davies, I. Hunter, E. H. Linfield, and H. E. Beere, "Terahertz frequency range band-stop filters," *Applied Physics Letters*, vol. 86, no. 21, 213503, 2005.

[22] E. Yablonovitch, D. Hwang, T. Gmitter, L. Florez, and J. Harbison, "Van der Waals bonding of GaAs epitaxial liftoff films onto arbitrary substrates," *Applied Physics Letters*, vol. 56, no. 24, pp. 2419–2421, 1990.

[23] D. Grischkowsky, S. Keiding, M. van Exter, and C. Fattinger, "Far-infrared time-domain spectroscopy with terahertz beams of dielectrics and semiconductors," *Journal of the Optical Society of America B*, vol. 7, no. 10, pp. 2006–2015, 1990.

[24] Q. Wu and X.-C. Zhang, "Free-space electro-optics sampling of mid-infrared pulses," *Applied Physics Letters*, vol. 71, no. 10, pp. 1285–1286, 1997.

[25] S. O. Kasap, *Optoelectronics and Photonics*. Prentice Hall, New Jersey, 1st ed., 2001.

[26] S. Dankowski, D. Streb, M. Ruff, P. Kiesel, M. Kneissl, B. Knüpfer, G. Döhler, U. Keil, C. Sørenson, and A. Verma, "Above band gap absorption spectra of the arsenic antisite defect in low temperature grown GaAs and AlGaAs," *Applied Physics Letters*, vol. 68, no. 1, pp. 37–39, 1996.

[27] K.-E. Peiponen, A. Zeitler, and M. Kuwata-Gonokami, *Terahertz Spectroscopy and Imaging*. Springer, Berlin, 1st ed., 2013.

[28] D. E. Spence, P. N. Kean, and W. Sibbett, "60-fsec pulse generation from a self-mode-locked Ti:sapphire laser," *Optics Letters*, vol. 16, no. 1, pp. 42–44, 1991.

[29] S. O. Kasap, *Principles of Electronic Materials and Devices*. McGraw-Hill Education, New York, 3rd ed., 2006.

[30] T. D. Dorney, R. G. Baraniuk, and D. M. Mittleman, "Material parameter estimation with terahertz time-domain spectroscopy," *Journal of the Optical Society of America A*, vol. 18, no. 7, pp. 1562–1571, 2001.

[31] L. Duvillaret, F. Garet, and J.-L. Coutaz, "A reliable method for extraction of material parameters in terahertz time-domain spectroscopy," *IEEE Journal of Selected Topics in Quantum Electronics*, vol. 2, no. 3, pp. 739–746, 1996.

[32] A. Baragwanath, G. Swift, D. Dai, A. Gallant, and J. Chamberlain, "Silicon based microfluidic cell for terahertz frequencies," *Journal of Applied Physics*, vol. 108, no. 1, 013102, 2010.

[33] Y. Ikeda, Y. Ishihara, T. Moriwaki, E. Kato, and K. Terada, "A novel analytical method for pharmaceutical polymorphs by terahertz spectroscopy and the optimization of crystal form at the discovery stage," *Chemical and Pharmaceutical Bulletin*, vol. 58, no. 1, pp. 76–81, 2010.

[34] A. D. Burnett, W. Fan, P. C. Upadhya, J. E. Cunningham, M. D. Hargreaves, T. Munshi, H. G. Edwards, E. H. Linfield, and A. G. Davies, "Broadband terahertz time-domain spectroscopy of drugs-of-abuse and the use of principal component analysis," *Analyst*, vol. 134, no. 8, pp. 1658–1668, 2009.

[35] J. Kindt and C. Schmuttenmaer, "Far-infrared dielectric properties of polar liquids probed by femtosecond terahertz pulse spectroscopy," *Journal of Physical Chemistry*, vol. 100, no. 24, pp. 10373–10379, 1996.

[36] M. J. Tauber, R. A. Mathies, X. Chen, and S. E. Bradforth, "Flowing liquid sample jet for resonance Raman and ultrafast optical spectroscopy," *Review of Scientific Instruments*, vol. 74, no. 11, pp. 4958–4960, 2003.

[37] T. Wang, P. Klarskov, and P. U. Jepsen, "Ultrabroadband THz time-domain spectroscopy of a free-flowing water film," *IEEE Transactions on Terahertz Science and Technology*, vol. 4, no. 4, pp. 425–431, 2014.

[38] A. Treizebre, S. Laurette, Y. Xu, R. G. Bosisio, and B. Bocquet, "THz power divider circuits on planar Goubau lines (PGLs)," *Progress In Electromagnetics Research C*, vol. 26, pp. 219–228, 2012.

[39] V. S. Mottonen and A. V. Raisanen, "Novel wide-band coplanar waveguide-to-rectangular waveguide transition," *IEEE Transactions on Microwave Theory and Techniques*, vol. 52, no. 8, pp. 1836–1842, 2004.

[40] A. Maestrini, B. Thomas, H. Wang, C. Jung, J. Treuttel, Y. Jin, G. Chattopadhyay, I. Mehdi, and G. Beaudin, "Schottky diode-based terahertz frequency multipliers and mixers," *Comptes Rendus Physique*, vol. 11, pp. 480–495, 2010.

[41] G. Gallot, S. Jamison, R. McGowan, and D. Grischkowsky, "Terahertz waveguides," *Journal of the Optical Society of America B*, vol. 17, no. 5, pp. 851–863, 2000.

[42] D. Dube and R. Natarajan, "Determination of dielectric parameters for films at microwave frequencies," *Journal of Applied Physics*, vol. 44, no. 11, pp. 4927–4929, 1973.

[43] V. Matvejev, C. De Tandt, W. Ranson, J. Stiens, R. Vounckx, and D. Mangelings, "Integrated waveguide structure for highly sensitive THz spectroscopy of nanoliter liquids in capillary tubes," *Progress In Electromagnetics Research*, vol. 121, pp. 89–101, 2011.

[44] M. Byrne, J. Cunningham, K. Tych, A. D. Burnett, M. R. Stringer, C. D. Wood, L. Dazhang, M. Lachab, E. H. Linfield, and A. G. Davies, "Terahertz vibrational absorption spectroscopy using microstrip-line waveguides," *Applied Physics Letters*, vol. 93, no. 18, 182904, 2008.

[45] J. Cunningham, C. Wood, A. Davies, C. Tiang, P. Tosch, D. Evans, E. Linfield, I. Hunter, and M. Missous, "Multiple-frequency terahertz pulsed sensing of dielectric films," *Applied Physics Letters*, vol. 88, no. 7, 071112, 2006.

[46] M. Y. Frankel, S. Gupta, J. A. Valdmanis, and G. A. Mourou, "Terahertz attenuation and dispersion characteristics of coplanar transmission lines," *IEEE Transactions on Microwave Theory and Techniques*, vol. 39, no. 6, pp. 910–916, 1991.

[47] H.-J. Cheng, J. F. Whitaker, T. M. Weller, and L. P. Katehi, "Terahertz-bandwidth characteristics of coplanar transmission lines on low permittivity substrates," *IEEE Transactions on Microwave Theory and Techniques*, vol. 42, no. 12, pp. 2399–2406, 1994.

[48] A. Sommerfeld, "Ueber die Fortpflanzung elektrodynamischer Wellen längs eines Drahtes," *Annalen der Physik*, vol. 303, no. 2, pp. 233–290, 1899.

[49] G. Goubau, "Surface waves and their application to transmission lines," *Journal of Applied Physics*, vol. 21, no. 11, pp. 1119–1128, 1950.

[50] Y.-S. Xu and R. Bosisio, "Application of Goubau lines for millimetre and submillimetre wave gas sensors," *IEE Proceedings – Microwaves, Antennas and Propagation*, vol. 152, no. 5, pp. 400–405, 2005.

[51] K. Alonso and M. J. Hagmann, "Simulations of tapered Goubau line for coupling microwave signals generated by resonant laser-assisted field emission," *Journal of Vacuum Science & Technology B: Microelectronics and Nanometer Structures Processing, Measurement, and Phenomena*, vol. 18, no. 2, pp. 1009–1013, 2000.

[52] K. Alonso and M. J. Hagmann, "Comparison of three different methods for coupling of microwave and terahertz signals generated by resonant laser-assisted field emission," *Journal of Vacuum Science & Technology B: Microelectronics and Nanometer Structures Processing, Measurement, and Phenomena*, vol. 19, no. 1, pp. 68–71, 2001.

[53] A. Treizebré, T. Akalin, and B. Bocquet, "Planar excitation of Goubau transmission lines for THz bioMEMS," *IEEE Microwave and Wireless Components Letters*, vol. 15, no. 12, pp. 886–888, 2005.

[54] C. Russell, C. D. Wood, A. D. Burnett, L. Li, E. H. Linfield, A. G. Davies, and J. E. Cunningham, "Spectroscopy of polycrystalline materials using thinned-substrate planar Goubau line at cryogenic temperatures," *Lab on a Chip*, vol. 13, no. 20, pp. 4065–4070, 2013.

[55] S. Laurette, A. Treizebre, and B. Bocquet, "Co-integrated microfluidic and THz functions for biochip devices," *Journal of Micromechanics and Microengineering*, vol. 21, no. 6, 065029, 2011.

[56] N. Marcuvitz, *Waveguide Handbook*. McGraw-Hill Book Company, New York, 1st ed., 1951.

[57] D. M. Pozar, *Microwave Engineering*. John Wiley & Sons, New Jersey, 4th ed., 2011.

[58] A. Treizebré, B. Bocquet, Y. Xu, and R. G. Bosisio, "New THz excitation of planar Goubau line," *Microwave and Optical Technology Letters*, vol. 50, no. 11, pp. 2998–3001, 2008.

[59] J. Cunningham, M. Byrne, P. Upadhya, M. Lachab, E. Linfield, and A. Davies, "Terahertz evanescent field microscopy of dielectric materials using on-chip waveguides," *Applied Physics Letters*, vol. 92, no. 3, 032903, 2008.

[60] S. Laurette, A. Treizebre, A. Elagli, B. Hatirnaz, R. Froidevaux, F. Affouard, L. Duponchel, and B. Bocquet, "Highly sensitive terahertz spectroscopy in microsystem," *RSC Advances*, vol. 2, no. 26, pp. 10064–10071, 2012.

[61] G. M. Whitesides, "The origins and the future of microfluidics," *Nature*, vol. 442, no. 7101, pp. 368–373, 2006.

[62] A. E. Kamholz and P. Yager, "Theoretical analysis of molecular diffusion in pressure-driven laminar flow in microfluidic channels," *Biophysical Journal*, vol. 80, no. 1, pp. 155–160, 2001.

[63] A. Markelz and E. Heilweil, "Temperature-dependent terahertz output from semi-insulating GaAs photoconductive switches," *Applied Physics Letters*, vol. 72, no. 18, pp. 2229–2231, 1998.

[64] M. Tsai, A. Kita, J. Leach, R. Rounsevell, J. N. Huang, J. Moake, R. E. Ware, D. A. Fletcher, and W. A. Lam, "In vitro modeling of the microvascular occlusion and thrombosis that occur in hematologic diseases using microfluidic technology," *The Journal of Clinical Investigation*, vol. 122, no. 1, pp. 408–418, 2012.

[65] D. Huh, B. D. Matthews, A. Mammoto, M. Montoya-Zavala, H. Y. Hsin, and D. E. Ingber, "Reconstituting organ-level lung functions on a chip," *Science*, vol. 328, no. 5986, pp. 1662–1668, 2010.

[66] H. Kimura, T. Yamamoto, H. Sakai, Y. Sakai, and T. Fujii, "An integrated microfluidic system for long-term perfusion culture and on-line monitoring of intestinal tissue models," *Lab on a Chip*, vol. 8, no. 5, pp. 741–746, 2008.

[67] K.-J. Jang and K.-Y. Suh, "A multi-layer microfluidic device for efficient culture and analysis of renal tubular cells," *Lab on a Chip*, vol. 10, no. 1, pp. 36–42, 2010.

[68] S.-A. Leung, R. F. Winkle, R. C. Wootton, and A. deMello, "A method for rapid reaction optimisation in continuous-flow microfluidic reactors using online Raman spectroscopic detection," *Analyst*, vol. 130, no. 1, pp. 46–51, 2005.

[69] L. Zhang, L. Wang, Y.-T. Kao, W. Qiu, Y. Yang, O. Okobiah, and D. Zhong, "Mapping hydration dynamics around a protein surface," *Proceedings of the National Academy of Sciences*, vol. 104, no. 47, pp. 18461–18466, 2007.

[70] S. Hay and N. S. Scrutton, "Good vibrations in enzyme-catalysed reactions," *Nature Chemistry*, vol. 4, no. 3, pp. 161–168, 2012.

[71] S. Laurette, A. Treizebre, F. Affouard, and B. Bocquet, "Subterahertz characterization of ethanol hydration layers by microfluidic system," *Applied Physics Letters*, vol. 97, no. 11, p. 111904, 2010.

[72] M. Walther, P. Plochocka, B. Fischer, H. Helm, and P. Uhd Jepsen, "Collective vibrational modes in biological molecules investigated by terahertz time-domain spectroscopy," *Biopolymers*, vol. 67, no. 4-5, pp. 310–313, 2002.

[73] C. S. Effenhauser, A. Manz, and H. M. Widmer, "Glass chips for high-speed capillary electrophoresis separations with submicrometer plate heights," *Analytical Chemistry*, vol. 65, no. 19, pp. 2637–2642, 1993.

[74] L. Brown, T. Koerner, J. H. Horton, and R. D. Oleschuk, "Fabrication and characterization of poly(methylmethacrylate) microfluidic devices bonded using surface modifications and solvents," *Lab on a Chip*, vol. 6, no. 1, pp. 66–73, 2006.

[75] K. S. Lee and R. J. Ram, "Plastic–PDMS bonding for high pressure hydrolytically stable active microfluidics," *Lab on a Chip*, vol. 9, no. 11, pp. 1618–1624, 2009.

[76] H. Wu, B. Huang, and R. N. Zare, "Construction of microfluidic chips using polydimethylsiloxane for adhesive bonding," *Lab on a Chip*, vol. 5, no. 12, pp. 1393–1398, 2005.

[77] M. Zhang, J. Wu, L. Wang, K. Xiao, and W. Wen, "A simple method for fabricating multi-layer PDMS structures for 3D microfluidic chips," *Lab on a Chip*, vol. 10, no. 9, pp. 1199–1203, 2010.

[78] Y. Xia, E. Kim, X.-M. Zhao, J. A. Rogers, M. Prentiss, and G. Whitesides, "Complex optical surfaces formed by replica molding against elastomeric masters," *Science*, vol. 273, no. 5273, pp. 347–349, 1996.

[79] M. A. Eddings, M. A. Johnson, and B. K. Gale, "Determining the optimal PDMS–PDMS bonding technique for microfluidic devices," *Journal of Micromechanics and Microengineering*, vol. 18, no. 6, 067001, 2008.

[80] E. K. Sackmann, A. L. Fulton, and D. J. Beebe, "The present and future role of microfluidics in biomedical research," *Nature*, vol. 507, no. 7491, pp. 181–189, 2014.

[81] P. Debye, "Zur theorie der spezifischen wärmen," *Annalen der Physik*, vol. 344, no. 14, pp. 789–839, 1912.

[82] J. Barthel, K. Bachhuber, R. Buchner, and H. Hetzenauer, "Dielectric spectra of some common solvents in the microwave region. Water and lower alcohols," *Chemical Physics Letters*, vol. 165, no. 4, pp. 369–373, 1990.

[83] U. Møller, D. G. Cooke, K. Tanaka, and P. U. Jepsen, "Terahertz reflection spectroscopy of Debye relaxation in polar liquids," *Journal of the Optical Society of America B*, vol. 26, no. 9, pp. A113–A125, 2009.

[84] G. Goubau, "Single-conductor surface-wave transmission lines," *Proceedings of the IRE*, vol. 39, no. 6, pp. 619–624, 1951.

[85] G. Goubau, "Open wire lines," *IRE Transactions on Microwave Theory and Techniques*, vol. 4, no. 4, pp. 197–200, 1956.

[86] D. Gacemi, J. Mangeney, R. Colombelli, and A. Degiron, "Subwavelength metallic waveguides as a tool for extreme confinement of THz surface waves," *Scientific Reports*, vol. 3, no. 1369, 2013.

[87] L. Dazhang, J. Cunningham, M. B. Byrne, S. Khanna, C. D. Wood, A. D. Burnett, S. M. Ershad, E. H. Linfield, and A. G. Davies, "On-chip terahertz Goubau-line waveguides with integrated photoconductive emitters and mode-discriminating detectors," *Applied Physics Letters*, vol. 95, no. 9, 092903, 2009.

[88] C. Russell, *Broadband On-chip Terahertz Spectroscopy*. PhD thesis, University of Leeds, 2013.

[89] A. Abbas, A. Treizebre, P. Supiot, N.-E. Bourzgui, D. Guillochon, D. Vercaigne-Marko, and B. Bocquet, "Cold plasma functionalized terahertz BioMEMS for enzyme reaction analysis," *Biosensors and Bioelectronics*, vol. 25, no. 1, pp. 154–160, 2009.

[90] M. Naftaly and R. E. Miles, "Terahertz time-domain spectroscopy for material characterization," *Proceedings of the IEEE*, vol. 95, no. 8, pp. 1658–1665, 2007.

[91] S. Yanagi, M. Onuma, J. Kitagawa, and Y. Kadoya, "Propagation of terahertz pulses on coplanar strip-lines on low permittivity substrates and a spectroscopy application," *Applied Physics Express*, vol. 1, no. 1, 012009, 2008.

[92] T. Akalin, A. Treizebré, and B. Bocquet, "Single-wire transmission lines at terahertz frequencies," *IEEE Transactions on Microwave Theory and Techniques*, vol. 54, no. 6, pp. 2762–2767, 2006.

[93] C. Wood, *On-chip THz Systems*. PhD thesis, University of Leeds, 2006.

[94] C. Russell, C. D. Wood, L. Dazhang, A. D. Burnett, L. H. Li, E. H. Linfield, A. G. Davies, and J. E. Cunningham, "Increasing the bandwidth of planar on-chip THz devices for spectroscopic applications," *The 36th International Conference on Infrared, Millimeter, and Terahertz Waves*, pp. 1–3, 2011.

[95] T. Tisone and J. Drobek, "Diffusion in thin film Ti–Au, Ti–Pd, and Ti–Pt couples," *Journal of Vacuum Science & Technology*, vol. 9, no. 1, pp. 271–275, 1972.

[96] M. Tani, S. Matsuura, K. Sakai, and S.-i. Nakashima, "Emission characteristics of photoconductive antennas based on low-temperature-grown GaAs and semi-insulating GaAs," *Applied Optics*, vol. 36, no. 30, pp. 7853–7859, 1997.

[97] B. Hu, X.-C. Zhang, and D. Auston, "Terahertz radiation induced by subband-gap femtosecond optical excitation of GaAs," *Physical Review Letters*, vol. 67, no. 19, pp. 2709–2712, 1991.

[98] J. Luo, H. Thomas, D. Morgan, and D. Westwood, "Thermal annealing effect on low temperature molecular beam epitaxy grown GaAs: Arsenic precipitation and the change of resistivity," *Applied Physics Letters*, vol. 64, no. 26, pp. 3614–3616, 1994.

[99] E. Hourdakis, B. J. Simonds, and N. M. Zimmerman, "Submicron gap capacitor for measurement of breakdown voltage in air," *Review of Scientific Instruments*, vol. 77, no. 3, 034702, 2006.

[100] R. S. Dhariwal, J.-M. Torres, and M. P. Y. Desmulliez, "Electric field breakdown at micrometre separations in air and nitrogen at atmospheric pressure," *IEE Proceedings – Science, Measurement and Technology*, vol. 147, no. 5, pp. 261–265, 2000.

[101] J. Luo, H. Thomas, D. Morgan, D. Westwood, and R. Williams, "The electrical breakdown properties of GaAs layers grown by molecular beam epitaxy at low temperature," *Semiconductor Science and Technology*, vol. 9, no. 12, pp. 2199–2204, 1994.

[102] E. Kreysig, *Advanced Engineering Mathematics*. John Wiley & Sons, Inc., New York, 8th ed., 1999.

[103] T. Radhakrishnan, "Further studies on the temperature variation of the refractive index of crystals," *Proceedings of the Indian Academy of Sciences-Section A*, vol. 33, no. 1, pp. 22–34, 1951.

[104] J. Kuta, H. van Driel, D. Landheer, and J. Adams, "Polarization and wavelength dependence of metal-semiconductor-metal photodetector response," *Applied Physics Letters*, vol. 64, no. 2, pp. 140–142, 1994.

[105] J. C. G. Lesurf, *Millimetre-wave Optics, Devices & Systems*. IOP Publishing Ltd., Bristol, 1st ed., 1990.

[106] E. R. Brown, J. E. Bjarnason, A. M. Fedor, and T. M. Korter, "On the strong and narrow absorption signature in lactose at 0.53 THz," *Applied Physics Letters*, vol. 90, no. 6, 061908, 2007.

[107] A. Weisshaar and V. K. Tripathi, "Perturbation analysis and modeling of curved microstrip bends," *IEEE Transactions on Microwave Theory and Techniques*, vol. 38, no. 10, pp. 1449–1454, 1990.

[108] J. Chiba, "Experimental studies of the losses and radiations due to bends in the Goubau line," *IEEE Transactions on Microwave Theory and Techniques*, vol. 25, no. 2, pp. 94–100, 1977.

[109] D. Gacemi, A. Degiron, M. Baillergeau, and J. Mangeney, "Identification of several propagation regimes for terahertz surface waves guided by planar Goubau lines," *Applied Physics Letters*, vol. 103, no. 19, 191117, 2013.

[110] O. Reynolds, "An experimental investigation of the circumstances which determine whether the motion of water shall be direct or sinuous, and of the law of resistance in parallel channels," *Proceedings of the Royal Society of London*, vol. 35, pp. 84–99, 1883.

[111] P. Watts and C. Wiles, "Recent advances in synthetic micro reaction technology," *Chemical Communications*, no. 5, pp. 443–467, 2007.

[112] O. Jones, "An improvement in the calculation of turbulent friction in rectangular ducts," *Journal of Fluids Engineering*, vol. 98, no. 2, pp. 173–180, 1976.

[113] K. Avila, D. Moxey, A. de Lozar, M. Avila, D. Barkley, and B. Hof, "The onset of turbulence in pipe flow," *Science*, vol. 333, no. 6039, pp. 192–196, 2011.

[114] B. Eckhardt, "Turbulence transition in pipe flow: 125th anniversary of the publication of Reynolds' paper," *Philosophical Transactions of the Royal Society A*, vol. 367, pp. 449–455, 2009.

[115] A. G. Darbyshire and T. Mullin, "Transition to turbulence in constant-mass-flux pipe flow," *Journal of Fluid Mechanics*, vol. 289, pp. 83–114, 1995.

[116] H. Faisst and B. Eckhardt, "Sensitive dependence on initial conditions in transition to turbulence in pipe flow," *Journal of Fluid Mechanics*, vol. 504, pp. 343–352, 2004.

[117] P. Shankar and M. Kumar, "Experimental determination of the kinematic viscosity of glycerol–water mixtures," *Proceedings of the Royal Society of London A*, vol. 444, no. 1922, pp. 573–581, 1994.

[118] H. Lorenz, M. Despont, N. Fahrni, J. Brugger, P. Vettiger, and P. Renaud, "High-aspect-ratio, ultrathick, negative-tone near-UV photoresist and its applications for MEMS," *Sensors and Actuators A: Physical*, vol. 64, no. 1, pp. 33–39, 1998.

[119] A. del Campo and C. Greiner, "SU-8: a photoresist for high-aspect-ratio and 3D submicron lithography," *Journal of Micromechanics and Microengineering*, vol. 17, no. 6, pp. R81–R95, 2007.

[120] MicroChem, *Processing Guidelines for SU-8 2000 Permanent Epoxy Negative Photoresist.* Rev. 4.

[121] N. Bowden, S. Brittain, A. G. Evans, J. W. Hutchinson, and G. M. Whitesides, "Spontaneous formation of ordered structures in thin films of metals supported on an elastomeric polymer," *Nature*, vol. 393, no. 6681, pp. 146–149, 1998.

[122] S. Satyanarayana, R. N. Karnik, and A. Majumdar, "Stamp-and-stick room-temperature bonding technique for microdevices," *Journal of Microelectromechanical Systems*, vol. 14, no. 2, pp. 392–399, 2005.

[123] J. S. Go and S. Shoji, "A disposable, dead volume-free and leak-free in-plane PDMS microvalve," *Sensors and Actuators A: Physical*, vol. 114, no. 2, pp. 438–444, 2004.

[124] M. A. Unger, H.-P. Chou, T. Thorsen, A. Scherer, and S. R. Quake, "Monolithic microfabricated valves and pumps by multilayer soft lithography," *Science*, vol. 288, no. 5463, pp. 113–116, 2000.

[125] D. C. Duffy, J. C. McDonald, O. J. A. Schueller, and G. M. Whitesides, "Rapid prototyping of microfluidic systems in poly(dimethylsiloxane)," *Analytical Chemistry*, vol. 70, no. 23, pp. 4974–4984, 1998.

[126] K. Haubert, T. Drier, and D. Beebe, "PDMS bonding by means of a portable, low-cost corona system," *Lab on a Chip*, vol. 6, no. 12, pp. 1548–1549, 2006.

[127] B. Samel, M. K. Chowdhury, and G. Stemme, "The fabrication of microfluidic structures by means of full-wafer adhesive bonding using a poly(dimethylsiloxane) catalyst," *Journal of Micromechanics and Microengineering*, vol. 17, no. 8, pp. 1710–1714, 2007.

[128] S. Bhattacharya, A. Datta, J. M. Berg, and S. Gangopadhyay, "Studies on surface wettability of poly(dimethyl)siloxane (PDMS) and glass under oxygen-plasma treatment and correlation with bond strength," *Journal of Microelectromechanical Systems*, vol. 14, no. 3, pp. 590–597, 2005.

[129] B.-H. Jo, L. M. van Lerberghe, K. M. Motsegood, and D. J. Beebe, "Three-dimensional micro-channel fabrication in polydimethylsiloxane (PDMS) elastomer," *Journal of Microelectromechanical Systems*, vol. 9, no. 1, pp. 76–81, 2000.

[130] Y. Berdichevsky, J. Khandurina, A. Guttman, and Y.-H. Lo, "UV/ozone modification of poly(dimethylsiloxane) microfluidic channels," *Sensors and Actuators B: Chemical*, vol. 97, no. 2, pp. 402–408, 2004.

[131] N. Y. Lee and B. H. Chung, "Novel poly(dimethylsiloxane) bonding strategy via room temperature 'chemical gluing'," *Langmuir*, vol. 25, no. 6, pp. 3861–3866, 2009.

[132] L. Tang and N. Y. Lee, "A facile route for irreversible bonding of plastic–PDMS hybrid microdevices at room temperature," *Lab on a Chip*, vol. 10, no. 10, pp. 1274–1280, 2010.

[133] J. Melai, C. Salm, S. Smits, J. Visschers, and J. Schmitz, "The electrical conduction and dielectric strength of SU-8," *Journal of Micromechanics and Microengineering*, vol. 19, no. 6, 065012, 2009.

[134] S. Arscott, F. Garet, P. Mounaix, L. Duvillaret, J.-L. Coutaz, and D. Lippens, "Terahertz time-domain spectroscopy of films fabricated from SU-8," *Electronics Letters*, vol. 35, no. 3, pp. 243–244, 1999.

[135] T. A. Anhoj, A. M. Jorgensen, D. A. Zauner, and J. Hübner, "The effect of soft bake temperature on the polymerization of SU-8 photoresist," *Journal of Micromechanics and Microengineering*, vol. 16, no. 9, pp. 1819–1824, 2006.

[136] L. Théolier, H. Mahfoz-Kotb, K. Isoird, F. Morancho, S. Assié-Souleille, and N. Mauran, "A new junction termination using a deep trench filled with benzocyclobutene," *IEEE Electron Device Letters*, vol. 30, no. 6, pp. 687–689, 2009.

[137] Dow Chemical Company, *Processing Procedures for CYCLOTENE 4000 Series Photo-BCB Resins (Puddle Develop Process)*, 2009.

[138] D. Gacemi, J. Mangeney, K. Blary, J.-F. Lampin, T. Laurent, T. Akalin, P. Crozat, and F. Meng, "Confinement of THz surface waves on the subwavelength size metal waveguide," *Applied Physics A*, vol. 109, no. 4, pp. 993–995, 2012.

[139] C. Russell, M. Swithenbank, C. D. Wood, A. D. Burnett, L. Li, E. H. Linfield, A. G. Davies, and J. E. Cunningham, "Integrated on-chip THz sensors for fluidic systems fabricated using flexible polyimide films," *IEEE Transactions on Terahertz Science and Technology*, vol. 6, no. 4, pp. 619–624, 2016.

[140] N. G. Paulter, D. N. Sinha, A. J. Gibbs, and W. R. Eisenstadt, "Optoelectronic measurements of picosecond electrical pulse propagation in coplanar waveguide transmission lines," *IEEE Transactions on Microwave Theory and Techniques*, vol. 37, no. 10, pp. 1612–1619, 1989.

[141] P. D. Cunningham, N. N. Valdes, F. A. Vallejo, L. M. Hayden, B. Polishak, X.-H. Zhou, J. Luo, A. K.-Y. Jen, J. C. Williams, and R. J. Twieg, "Broadband terahertz characterization of the refractive index and absorption of some important polymeric and organic electro-optic materials," *Journal of Applied Physics*, vol. 109, no. 4, 043505, 2011.

[142] Y. Yomogida, Y. Sato, R. Nozaki, T. Mishina, and J. Nakahara, "Comparative study of boson peak in normal and secondary alcohols with terahertz time-domain spectroscopy," *Physica B: Condensed Matter*, vol. 405, no. 9, pp. 2208–2212, 2010.

[143] E. Perret, N. Zerounian, S. David, and F. Aniel, "Complex permittivity characterization of benzocyclobutene for terahertz applications," *Microelectronic Engineering*, vol. 85, no. 11, pp. 2276–2281, 2008.

[144] A. Podzorov and G. Gallot, "Low-loss polymers for terahertz applications," *Applied Optics*, vol. 47, no. 18, pp. 3254–3257, 2008.

[145] K.-H. Schlereth and M. Tacke, "The complex propagation constant of multilayer waveguides: an algorithm for a personal computer," *IEEE Journal of Quantum Electronics*, vol. 26, no. 4, pp. 627–630, 1990.

[146] J. N. Lee, C. Park, and G. M. Whitesides, "Solvent compatibility of poly(dimethylsiloxane)-based microfluidic devices," *Analytical Chemistry*, vol. 75, no. 23, pp. 6544–6554, 2003.

[147] J. Barthel, K. Bachhuber, R. Buchner, H. Hetzenauer, and M. Kleebauer, "A computer-controlled system of transmission lines for the determination of the complex permittivity of lossy liquids between 8.5 and 90 GHz," *Berichte der Bunsengesellschaft für Physikalische Chemie*, vol. 95, no. 8, pp. 853–859, 1991.

[148] Y. Yomogida, Y. Sato, R. Nozaki, T. Mishina, and J. Nakahara, "Dielectric study of normal alcohols with THz time-domain spectroscopy," *Journal of Molecular Liquids*, vol. 154, no. 1, pp. 31–35, 2010.

[149] H. Hirori, T. Arikawa, M. Nagai, H. Ohtake, M. Yoshida, and K. Tanaka, "Accurate determination of complex dielectric constants by terahertz time domain attenuated total reflection spectroscopy," *Conference Digest of the Joint 29th International Conference on Infrared and Millimeter Waves, and 12th International Conference on Terahertz Electronics*, pp. 251–252, 2004.

[150] T. Fukasawa, T. Sato, J. Watanabe, Y. Hama, W. Kunz, and R. Buchner, "Relation between dielectric and low-frequency Raman spectra of hydrogen-bond liquids," *Physical Review Letters*, vol. 95, no. 19, 197802, 2005.

[151] J. Barthel and R. Buchner, "High frequency permittivity and its use in the investigation of solution properties," *Pure and Applied Chemistry*, vol. 63, no. 10, pp. 1473–1482, 1991.

[152] P. Pruksathorn and T. Vitidsant, "Production of pure ethanol from azeotropic solution by pressure swing adsorption," *Korean Journal of Chemical Engineering*, vol. 26, no. 4, pp. 1106–1111, 2009.

[153] M. Naftaly, "An international intercomparison of THz time-domain spectrometers," 41st *International Conference on Infrared, Millimeter, and Terahertz waves*, pp. 1–2, 2016.

[154] D. W. Marquardt, "An algorithm for least-squares estimation of nonlinear parameters," *Journal of the Society for Industrial and Applied Mathematics*, vol. 11, no. 2, pp. 431–441, 1963.

[155] L. Thrane, R. H. Jacobsen, P. U. Jepsen, and S. Keiding, "THz reflection spectroscopy of liquid water," *Chemical Physics Letters*, vol. 240, no. 4, pp. 330–333, 1995.

[156] P. U. Jepsen, J. K. Jensen, and U. Møller, "Characterization of aqueous alcohol solutions in bottles with THz reflection spectroscopy," *Optics Express*, vol. 16, no. 13, pp. 9318–9331, 2008.

[157] D. R. Bacon, A. D. Burnett, M. Swithenbank, C. Russell, L. Li, C. D. Wood, J. Cunningham, E. H. Linfield, A. G. Davies, P. Dean, and J. Freeman, "Free-space terahertz radiation from a LT-GaAs-on-quartz large-area photoconductive emitter," *Optics Express*, vol. 24, no. 23, pp. 26986–26997, 2016.

[158] P. U. Jepsen and B. M. Fischer, "Dynamic range in terahertz time-domain transmission and reflection spectroscopy," *Optics Letters*, vol. 30, no. 1, pp. 29–31, 2005.

[159] G. Gallot, J. Zhang, R. McGowan, T.-I. Jeon, and D. Grischkowsky, "Measurements of the THz absorption and dispersion of ZnTe and their relevance to the electro-optic detection of THz radiation," *Applied Physics Letters*, vol. 74, no. 23, pp. 3450–3452, 1999.

[160] W. Withayachumnankul and M. Naftaly, "Fundamentals of measurement in terahertz time-domain spectroscopy," *Journal of Infrared, Millimeter, and Terahertz Waves*, vol. 35, no. 8, pp. 610–637, 2014.

[161] M. Scheller, C. Jansen, and M. Koch, "Analyzing sub-100-μm samples with transmission terahertz time domain spectroscopy," *Optics Communications*, vol. 282, no. 7, pp. 1304–1306, 2009.